



저작자표시-비영리-변경금지 2.0 대한민국

이용자는 아래의 조건을 따르는 경우에 한하여 자유롭게

- 이 저작물을 복제, 배포, 전송, 전시, 공연 및 방송할 수 있습니다.

다음과 같은 조건을 따라야 합니다:



저작자표시. 귀하는 원저작자를 표시하여야 합니다.



비영리. 귀하는 이 저작물을 영리 목적으로 이용할 수 없습니다.



변경금지. 귀하는 이 저작물을 개작, 변형 또는 가공할 수 없습니다.

- 귀하는, 이 저작물의 재이용이나 배포의 경우, 이 저작물에 적용된 이용허락조건을 명확하게 나타내어야 합니다.
- 저작권자로부터 별도의 허가를 받으면 이러한 조건들은 적용되지 않습니다.

저작권법에 따른 이용자의 권리는 위의 내용에 의하여 영향을 받지 않습니다.

이것은 [이용허락규약\(Legal Code\)](#)을 이해하기 쉽게 요약한 것입니다.

[Disclaimer](#)

理學博士 學位論文

화학 및 생 분석 검출을 위한
새로운 신호증폭 전략

New Signal Amplification Strategies for
Chemical and Biological Detection

2014 年 8 月

서울대학교 大學院

化學部 電氣化學專攻

韓 東 勳

화학 및 생 분석 검출을 위한 새로운 신호증폭 전략

指導 教授 鄭 澤 東

이 論文을 理學博士 學位論文으로 提出함
2014 年 8 月

서울大學校 大學院
化學部 電氣化學專攻
韓 東 勳

韓東勳의 理學博士 學位論文을 認准함
2014 年 6 月

委 員 長 _____ (인)

副委員長 _____ (인)

委 員 _____ (인)

委 員 _____ (인)

委 員 _____ (인)

A Dissertation entitled

New Signal Amplification Strategies for
Chemical and Biological Detection

By Donghoon Han

Major: Electrochemistry

Submitted as partial fulfillment of the requirements for the
Doctor of Philosophy degree in Chemistry

Advisor: Prof. Taek Dong Chung

Seoul National University

August, 2014

Abstract

In modern analytical research, the development of sensitive, reliable, and inexpensive high-throughput assays for the detection of biomolecules has shown great potential in clinical diagnostics, food safety, and environmental monitoring. One of the most important issues in bioanalysis is to generate ultrasensitive signals, which will allow the analytes of interest to be identified with minimal treatment and consumption of samples and reagents. This dissertation describes the development and application of analytical methodologies for chemical/biological detection to improve their analytical performance.

First, we developed a gold microshell-based surface enhanced Raman scattering (SERS) sensor for the detection of mercury(II) ions. This sensor is based on a molecular beacon, which involves a Raman-active, tetramethylrhodamine-tagged DNA hairpin structure and provides strategically selective binding of a thymine-thymine mismatch to Hg^{2+} ions. The sensor achieved good sensitivity and a detection limit of 50 nM by monitoring the change in the SERS signal of Raman reporters confined on the gold microshell surface. The

selectivity of the sensor was demonstrated by the specific discrimination of mercury(II) ion from various other competing divalent metal ions. In addition, a DNA-modified single gold microshell could be individually manipulated using a micropipette. The DNA-modified single gold microshell demonstrated that the detection of mercury(II) ions could be successfully performed in small-volume sample solutions.

Second, we devised a new method to enhance the sensitivity of a competitive immunoassay using electrokinetic concentration near a pair of highly charge-selective polymer [poly-2-acrylamido-2-methyl-1-propanesulfonic acid (pAMPSA)] plugs on a microfluidic chip. The polyelectrolytic gel, which was photopolymerized in a microfluidic channel network, served as the effective charge-selective extractor to sophisticatedly control the ion distribution. In this system, fluorescent indicators on the magnetic microbeads dispersed in the sample were spontaneously displaced by the unlabeled target molecules and then electrokinetically preconcentrated in a single spot on the microfluidic chip. The locally preconcentrated fluorescent indicators were detected using laser-induced fluorescence. As a proof-of-concept, the

competitive displacement assay of unlabeled 1 nM biotin was conducted to observe *ca.* 2000-fold enrichment within 3 min. In addition to the sensitive assessment of unlabeled small target molecules, the proposed immunoassay system also showed good selectivity for biotin analogs such as biocytin, 2-iminobiotin, and desthiobiotin.

Third, we suggest an electrochemical redox cycling based on the three-dimensional interdigitated array (3D IDA) electrodes for signal amplification to enhance the sensitivity of chip-based immunosensors. The 3D IDA consists of two closely spaced parallel indium tin oxide (ITO) electrodes, which were not only positioned at the bottom but also the on ceiling, facing each other along a microfluidic channel. The geometric configurations affecting the signal intensity were investigated for the parallel electrode, Open-2D IDA, Closed-2D IDA, and 3D IDA through electrochemical experiments and finite-element simulations. The 3D IDA, amongst the four different systems, exhibited the greatest signal amplification resulting from the efficient redox cycling of electroactive species confined in the microchannels, such that the faradaic current was augmented by a factor of ~ 100 . We exploited the

enhanced sensitivity of the 3D IDA to build a chronocoulometric immunosensing platform based on the sandwich enzyme-linked immunosorbent assay (ELISA) protocol. The mouse IgGs on the 3D IDA showed much lower detection limits compared to those on the Closed-2D IDA. Moreover, the proposed immunosensor system based on the 3D IDA could be successfully used in clinical analysis, as shown by the sensitive detection of up to 100 fg/mL cardiac troponin I in human serum.

Fourth, we report that the amine-terminated polyamidoamine (PAMAM) dendrimers can be immobilized onto the ITO surfaces via the electrooxidative coupling of the terminal amine groups of dendrimers to the ITO surfaces. The electrochemical measurements confirmed the electrochemical immobilization of the amine-terminated dendrimers onto the ITO surfaces. The immobilization approach was applied to assemble the partially tethered ferrocenyl dendrimer (Fc-D) and Pt dendrimer-encapsulated nanoparticles (Pt DENs) onto the ITO surfaces, and the resulting dendrimers-grafted films showed electrocatalytic activity for the *p*-aminophenol redox reaction.

Finally, a new strategy involving three-electrode system fabrication in microchip systems has been described herein. A

standard photolithography method was used for the fabrication of an on-chip integrated three-electrode system, with a solid-state reference electrode, an ITO working electrode, and an electrodeposited Pt counter electrode. Electroplating conditions of potential and time were investigated with respect to the stability and uniformity of the electrodeposited films used as reference and counter electrodes. The solid-state reference electrode was fabricated using an electropolymerized poly-1,3-phenylenediamine (poly-*m*-PD) layer on a nanoporous platinum (np Pt) surface. The electrochemical performance of the three-electrode system was evaluated using cyclic voltammetry. The experimental results in this study demonstrate that the proposed system successfully works as a solid-state reference electrode, which can be integrated into microchips for microanalysis systems.

Keywords: Surface enhanced Raman scattering, Electrokinetic concentration, Three-dimensional interdigitated array, Redox cycling, Electrografting, Integrated electrochemical sensing platform

Student number: 2009-30852

Contents

Abstract	1
Contents	6
List of Figures	11
1. Introduction	23
1.1. Background and Overview	23
1.2. References	29
2. Mercury(II) Detection by SERS based on a Single Gold Microshell	31
2.1. Introduction	31
2.2. Experimental	35
2.2.1. Materials and reagents	35
2.2.2. Preparation of gold microshells	36
2.2.3. Functionalization of gold microshells with ss-DNA	37
2.2.4. Trapping a DNA-modified single gold microshell at the tip of the micropipette and manipulation	38
2.2.5. Instruments	39
2.3. Results and Discussion	40
2.3.1. Principle of sensor operation	40
2.3.2. Sensitivity of Hg ²⁺ sensor.....	45
2.3.3. Selectivity of Hg ²⁺ sensor.....	47
2.3.4. Application for small volume analysis.....	49
2.4. Conclusion	51
2.5. References	52

3. Electrokinetic Concentration on a Microfluidic Chip using Polyelectrolytic Gel Plugs for Small Molecule Immunoassay	55
3.1. Introduction	55
3.2. Experimental	61
3.2.1. Reagents	61
3.2.2. Preparation of antibody–conjugated magnetic microbeads	62
3.2.3. Competitive immunoassay	63
3.2.4. Fabrication of microfluidic chips	63
3.2.5. Polyelectrolytic gel plugs (pAMPSA) fabrication process	65
3.2.6. Instrumentation	67
3.3. Results and Discussion	68
3.3.1. The mechanism of electrokinetic concentration polarization	68
3.3.2. Electrokinetic preccentration of fluorescent indicators	71
3.3.3. Displacement and subsequent preconcentration	74
3.3.4. Sensitivity	75
3.3.5. Specificity	81
3.4. Conclusion	84
3.5. References	86
4. Electrochemical Signal Amplification for Immunosensor based on 3D Interdigitated Array Electrodes	91
4.1. Introduction	91
4.2. Experimental	97
4.2.1. Chemicals and materials	97
4.2.2. Device fabrication	98
4.2.3. Modeling and calculations	103
4.2.4. Electrode modification and	

procedures for measurements	104
4.2.5. Electrochemical measurements	106
4.3. Theory	108
4.3.1. Electrochemical processes	108
4.3.2. Finite element simulations	109
4.4. Results and Discussion	111
4.4.1. Current amplification by 3D IDA electrode.....	111
4.4.2. Signal amplification of various types of devices.....	115
4.4.3. Electrografting of ferrocene moieties on ITO electrodes	126
4.4.4. Immunosensing performance by dependence on geometry	134
4.4.5. Sensitive detection of cTnI using 3D IDA electrode	140
4.4. Conclusion	143
4.6. References	145
5. Electrografting of an ITO Surface with Amine- Terminated Dendrimers and its Application to Electrocatalytic Reaction	152
5.1. Introduction	152
5.2. Experimental	158
5.2.1. Chemicals and materials	158
5.2.2. Synthesis of Pt DENs	159
5.2.3. Preparation of the Fc-D-modified ITO electrode	159
5.2.4. Modification of ITO surfaces with Pt DENs	162
5.2.5. Fabrication of IDA microelectrode	162
5.2.6. Electrochemical measurements	164
5.3. Results and Discussion	165
5.3.1. Preparation and characterization of Fc-D- modified electrodes	165

5.3.2. Immobilization of Pt DENs on ITO electrodes	171
5.3.3. Application of Fc–D and Pt DEN–grafted ITO electrodes to electrocatalysis	174
5.4. Conclusion	187
5.5. References	188
6. A Novel Three–Electrode System Microfabricated onto ITO for On–Chip Electrochemical Detection	192
6.1. Introduction	192
6.2. Experimental	197
6.2.1. Chemicals and materials	197
6.2.2. Micropatterning of ITO–coated glass substrates	197
6.2.3. Fabrication of integrated three–electrode system	199
6.2.4. Electrochemical measurements	202
6.3. Results and Discussion	203
6.3.1. Fabrication of a Pt counter electrode on an ITO surface for a microchip	203
6.3.2. Fabrication of the solid–state reference electrode for the microchip using L_2 –ePt	210
6.3.3. Application for microchip with integrated three–electrode system	217
6.4. Conclusion	222
6.5. References	224
7. Summary	226
Appendix	231
A. Mask Layout	231
B. Cyclic Voltammetry Simulation at 3D IDA with COMSOL	

Multiphysics233

Abstract (in Korean)258

Acknowledgments (in Korean)262

List of Figures

[Fig. 2–1] Scanning electron microscopy (SEM) image of gold microshells composed of (PS–NH ₂ /AuNPs) with the diameter of 2 μm.	41
[Fig. 2–2] Schematic description of the SERS sensor for Hg ²⁺ ion detection.	42
[Fig. 2–3] SERS spectra obtained from DNA–modified gold microshells at a variety of Hg ²⁺ ion concentrations. The most prominent peak of TAMRA is observed at 1650 cm ⁻¹ . Inset: An optical microscopic image of DNA–modified gold microshells placed on a slide glass. The laser probe is indicated by an arrow. Scale bar in an inset is 10 μm.	44
[Fig. 2–4] A calibration curve for Hg ²⁺ ions. The error bars denote the standard deviations taken from at least four independent measurements.	46
[Fig. 2–5] Selectivity of our SERS probe over various divalent metal ions (10 μM for Hg ²⁺ and 50 μM for other metal ions) and a mixture of metal ions (10 μM each of Mg ²⁺ , Ca ²⁺ , Ba ²⁺ , Mn ²⁺ , Fe ²⁺ , Co ²⁺ , Ni ²⁺ , Cu ²⁺ , Zn ²⁺ , Cd ²⁺ , Pb ²⁺ plus Hg ²⁺). The error bars represent the standard deviations taken from at least four independent measurements.	48
[Fig. 2–6] Scheme of transferring and placing a single DNA–modified gold microshell on the point of interest. DNA–modified gold microshells sprinkled on a glass slide, trapped at the tip end of a micropipette (gray), and then released into the Hg ²⁺ solution (blue) of small volume. An optical microscope image shows a DNA–modified single gold microshell at the end of a	

micropipette tip. The SERS spectrum was obtained from the DNA-modified single gold microshell after reaction with 5 μL of the 10 μM Hg^{2+} ion solution.50

[Fig. 3-1] Schematic illustration of small molecule detection by combining the effective sample preconcentration on a microfluidic chip with bead-based competitive immunoassay. The enlarged view is an optical micrograph showing a microchannel section incorporating the polyelectrolytic gel plugs.69

[Fig. 3-2] Sample preconcentration process based on electrokinetic trapping. (A) Voltages at V_H , V_L , and GND of 8 V, 3 V, and float, respectively. The solution of displaced indicators flows along the sample and analysis channel. (B) GND is 0 V. Only cations are extracted through the negatively charged polyelectrolytic gel plugs, pAMPSA, while anions are expelled from the interface between the pair of pAMPSA plugs and solution. (C and D) Then, the ion depletion region expands along the main microchannel. Negatively charged indicators are stacked to the left of the ion depletion boundary due to the concentration polarization. Red and green arrows indicate cation and anion movement near the pAMPSA, respectively.72

[Fig. 3-3] Examples of sample preconcentration. The microchannel was filled with 5 μM biotin-4-fluorescein in Tris buffer (10 mM Tris-HCl, pH 8.3). When V_H , V_L , and GND were 8 V, 5 V, and 0 V, respectively, biotin-4-fluorescein was rapidly preconcentrated in the microchannel (0~70 s). The preconcentrated biotin-4-fluoresceins were redispersed into

the sample solution by setting the GND electrode float (70~90 s).	73
[Fig. 3-4] Optical (left) and fluorescence (right) micrographs of magnetic microbeads bearing the fluorescent indicators (biotin-4-fluorescein).	76
[Fig. 3-5] Optical (left) and fluorescence (right) micrographs obtained from the magnetic microbeads after competitive immunoreaction with unlabeled biotin targets and subsequent washing. The fluorescent indicators (biotin-4-fluoresceins) previously conjugated with the antibodies were washed out. ..	77
[Fig. 3-6] Optical (left) and fluorescence (right) micrographs obtained from the magnetic microbeads conjugated with the unlabeled biotin target after be exposed to the fluorescent indicators in the solution.	78
[Fig. 3-7] A series of fluorescence micrographs obtained during the electrokinetic preconcentration of the fluorescent indicators displaced by 100 nM biotin. $V_H = 8$ V, $V_L = 3$ V, and GND = 0 V.	79
[Fig. 3-8] Fluorescence intensity profiles of the concentrated indicators displaced by 1 μ M, 100 nM, 10 nM, and 1 nM biotin during electrokinetic preconcentration. The horizontal dotted lines are the fluorescence intensities of 1, 2, and 5 μ M standard indicator solutions for comparison.	80
[Fig. 3-9] Specificity of the proposed immunoassay over a few target analogs (1 μ M for all) which were biocytin, 2-aminobiotin, and desthiobiotin. The profile obtained from 1 μ M native biotin was plotted again for comparison.	82

[Fig. 4–1] Fabrication process of the 3D IDA device. (A) PR is coated on ITO substrate. Then, the PR film is exposed to UV light through a photomask. (B) The PR film is developed in a PR developer. (C) The exposed area of ITO is removed by etchant solution and the PR is removed. (D) An adhesion layer is deposited that ultimately determines the height of the channel. (E) The adhesion layer is removed to create fluidic channel. (F) Another IDA electrode is attached to construct the 3D IDA. ...99

[Fig. 4–2] An optical microscope image of part of ITO band pattern of IDA electrode. The 5 μm width, 10 μm gap, 2 mm long IDA electrode contains 25 bands on each side.100

[Fig. 4–3] Schematic illustration of redox cycling of the 3D IDA electrode.113

[Fig. 4–4] Cyclic voltammograms of 1 mM $\text{Fc}(\text{MeOH})_2$ in 2 M KCl (scan rate 5 $\text{mV} \cdot \text{s}^{-1}$) at the 3D IDA electrode. The IDA electrodes on the bottom were swept while the top IDA electrodes on the ceiling were disconnected (dashed line, magnification shown in inset). The potential of generator electrodes of the top and bottom IDA was swept and the potential of collector IDA electrodes on the bottom and ceiling was held at -0.2 V (red line).114

[Fig. 4–5] Left side: Schematic diagram of parallel electrode. Middle: Electrode geometry dependence of voltammetric response of 1 mM $\text{Fc}(\text{MeOH})_2$ solution on the parallel electrode. Right side: Concentration profiles of $\text{Fc}(\text{MeOH})_2$ for the parallel electrode under steady-state conditions with applying oxidizing ($E1$) and reducing ($E2$) at the electrodes. The color scale shows the concentration distribution of oxidized molecules for

the various types of devices (*red*: fully reduced, *blue*: fully oxidized). The microchannel height was set to be 30 μm117

[Fig. 4–6] Left side: Schematic diagram of Open–2D IDA. Middle: Electrode geometry dependence of voltammetric response of 1 mM $\text{Fc}(\text{MeOH})_2$ solution on the Open–2D IDA. Right side: Concentration profiles of $\text{Fc}(\text{MeOH})_2$ for the Open–2D IDA under steady–state conditions with applying oxidizing ($E1$) and reducing ($E2$) at the electrodes. The color scale shows the concentration distribution of oxidized molecules for the various types of devices (*red*: fully reduced, *blue*: fully oxidized).118

[Fig. 4–7] Left side: Schematic diagram of Closed–2D IDA. Middle: Electrode geometry dependence of voltammetric response of 1 mM $\text{Fc}(\text{MeOH})_2$ solution on the Closed–2D IDA. Right side: Concentration profiles of $\text{Fc}(\text{MeOH})_2$ for the Closed–2D IDA under steady–state conditions with applying oxidizing ($E1$) and reducing ($E2$) at the electrodes. The color scale shows the concentration distribution of oxidized molecules for the various types of devices (*red*: fully reduced, *blue*: fully oxidized). The microchannel height was set to be 30 μm119

[Fig. 4–8] Left side: Schematic diagram of 3D IDA. Middle: Electrode geometry dependence of voltammetric response of 1 mM $\text{Fc}(\text{MeOH})_2$ solution on the 3D IDA. Right side: Concentration profiles of $\text{Fc}(\text{MeOH})_2$ for the 3D IDA under steady–state conditions with applying oxidizing ($E1$) and reducing ($E2$) at the electrodes. The color scale shows the concentration distribution of oxidized molecules for the various

types of devices (*red*: fully reduced, *blue*: fully oxidized). The microchannel height was set to be 30 μm120

[**Fig. 4–9**] Left side: Schematic diagram of different channel height of the 3D IDA. Middle: Channel height dependence of voltammetric response of 1 mM $\text{Fc}(\text{MeOH})_2$ solution on the device. Right side: Concentration profiles of $\text{Fc}(\text{MeOH})_2$ for the various channel height of the 3D IDA after a minimal time interval of 10 ms with applying oxidizing (*E1*) and reducing (*E2*) potentials at the electrodes. The color scale shows the concentration of oxidized molecules between top and bottom IDA electrodes (*red*: reduced, *blue*: oxidized). The scan rate was $5 \text{ mV} \cdot \text{s}^{-1}$122

[**Fig. 4–10**] Left side: Schematic diagram of different channel height of the 3D IDA. Middle: Channel height dependence of voltammetric response of 1 mM $\text{Fc}(\text{MeOH})_2$ solution on the device. Right side: Concentration profiles of $\text{Fc}(\text{MeOH})_2$ for the various channel height of the 3D IDA after a minimal time interval of 10 ms with applying oxidizing (*E1*) and reducing (*E2*) potentials at the electrodes. The color scale shows the concentration of oxidized molecules between top and bottom IDA electrodes (*red*: reduced, *blue*: oxidized). The scan rate was $5 \text{ mV} \cdot \text{s}^{-1}$123

[**Fig. 4–11**] Left side: Schematic diagram of different channel height of the 3D IDA. Middle: Channel height dependence of voltammetric response of 1 mM $\text{Fc}(\text{MeOH})_2$ solution on the device. Right side: Concentration profiles of $\text{Fc}(\text{MeOH})_2$ for the various channel height of the 3D IDA after a minimal time interval of 10 ms with applying oxidizing (*E1*) and reducing (*E2*)

potentials at the electrodes. The color scale shows the concentration of oxidized molecules between top and bottom IDA electrodes (*red*: reduced, *blue*: oxidized). The scan rate was $5 \text{ mV} \cdot \text{s}^{-1}$124

[Fig. 4–12] Left side: Schematic diagram of different channel height of the 3D IDA. Middle: Channel height dependence of voltammetric response of 1 mM $\text{Fc}(\text{MeOH})_2$ solution on the device. Right side: Concentration profiles of $\text{Fc}(\text{MeOH})_2$ for the various channel height of the 3D IDA after a minimal time interval of 10 ms with applying oxidizing ($E1$) and reducing ($E2$) potentials at the electrodes. The color scale shows the concentration of oxidized molecules between top and bottom IDA electrodes (*red*: reduced, *blue*: oxidized). The scan rate was $5 \text{ mV} \cdot \text{s}^{-1}$125

[Fig. 4–13] Cyclic voltammograms obtained on ITO in an aqueous 2 mM (hydrazinocarbonyl)ferrocene solution containing 0.1 M LiClO_4 . Scan rate was $10 \text{ mV} \cdot \text{s}^{-1}$129

[Fig. 4–14] Cyclic voltammograms of a Fc-grafted (solid line) and a bare ITO (dashed line) electrode in 1 M NaClO_4 . Scan rate was $20 \text{ mV} \cdot \text{s}^{-1}$130

[Fig. 4–15] Cyclic voltammograms of Fc-grafted ITO electrode in 1 M NaClO_4 at scan rates from 5 to $100 \text{ mV} \cdot \text{s}^{-1}$131

[Fig. 4–16] Dependence of the oxidation peak current on the scan rates.132

[Fig. 4–17] XPS spectra for (A) Fc-modified and (B) a bare ITO electrode.133

[Fig. 4–18] (A) Schematic illustration of the preparation of an

immunosensing layer. (B) Schematic view for electrochemical detection of target antigen.	136
[Fig. 4-19] Immunosensing scheme (left) and chronocoulograms (right) of the electrochemical immunosensor for the Closed-2D IDA.	137
[Fig. 4-20] Immunosensing scheme (left) and chronocoulograms (right) of the electrochemical immunosensor for the 3D IDA.	138
[Fig. 4-21] Calibration curves obtained with Closed-2D IDA (red circles, magnification shown in inset) and 3D IDA (black squares) electrodes for the detection of mouse IgG. The dashed line corresponds to three times the standard deviation of the charge at the concentration of zero. The error bars represent the standard deviations taken from at least three independent measurements.	139
[Fig. 4-22] Chronocoulograms obtained with the 3D IDA for various concentration of cTnI in human serum.	141
[Fig. 4-23] Calibration curve for the detection of cTnI. The dashed line corresponds to three times the standard deviation of the charge at the concentration of zero. The error bars denote the standard deviations taken from at least three independent measurements.	142
[Fig. 5-1] Structure of alkylthiols self-assembled monolayers.	155
[Fig. 5-2] Schematic illustration of the preparation of Fc-D-modified ITO electrode.	161
[Fig. 5-3] Cyclic voltammograms obtained on ITO electrode in	

an aqueous 10 μM G6-NH ₂ PAMAM dendrimer solution containing 0.1 M LiClO ₄ . Scan rate was 10 mV · s ⁻¹	167
[Fig. 5-4] Cyclic voltammograms of a Fc-D-modified (solid line) and a bare ITO (dashed line) electrode in 1 M NaClO ₄ . Scan rate was 20 mV · s ⁻¹	168
[Fig. 5-5] Cyclic voltammograms of Fc-D-modified ITO electrode in 1 M NaClO ₄ at scan rates from 5 to 100 mV · s ⁻¹	169
[Fig. 5-6] Dependence of the oxidation peak current on the scan rates.	170
[Fig. 5-7] Cyclic voltammograms obtained on ITO electrode in an aqueous 10 μM Pt DEN solution containing 0.1 M LiClO ₄ . Scan rate was 10 mV · s ⁻¹	172
[Fig. 5-8] Cyclic voltammogram of a Pt DEN-grafted ITO electrode in 0.5 M H ₂ SO ₄ . Scan rate was 100 mV · s ⁻¹	173
[Fig. 5-9] Cyclic voltammograms obtained using a conventional, three-electrode electrochemical cell consisting of an ITO working electrode (r = 3 mm), a Ag/AgCl reference electrode, and a Pt counter electrode. The electrolyte solution contained 50 mM Tris buffer (pH 9.0), 10 mM MgCl ₂ , and (A) 1 mM AP, (B) 5 mM APP, and (C) no redox-active couple. Scan rate was 50 mV · s ⁻¹	175
[Fig. 5-10] Cyclic voltammograms of the Fc-D-modified ITO electrode in the absence and presence of 1 mM AP in a Tris buffer (pH 9.0) containing 10 mM MgCl ₂ . Scan rate was 50 mV · s ⁻¹	180
[Fig. 5-11] Cyclic voltammograms of 1 mM AP obtained from the bare IDA (A) and the Fc-D-modified IDA electrode (B).	

The potential of generator electrodes of the bare IDA and the Fc-D modified IDA electrode was swept and the potential of collector electrodes of the bare IDA and the Fc-D-modified IDA electrode was held at -0.8 and -0.6 V, respectively. Scan rate was $5 \text{ mV} \cdot \text{s}^{-1}$181

[Fig. 5-12] Cyclic voltammograms of 1 mM AP obtained from the bare ITO electrode and the Pt DEN-grafted ITO electrode. Scan rate was $50 \text{ mV} \cdot \text{s}^{-1}$184

[Fig. 5-13] Cyclic voltammograms of the Pt DEN-grafted ITO electrode in the absence and presence of 1 mM AP in a Tris buffer (pH 9.0) containing 10 mM MgCl_2 . Scan rate was $50 \text{ mV} \cdot \text{s}^{-1}$185

[Fig. 5-14] Cyclic voltammograms of 1 mM AP obtained from the bare IDA (A) and the Pt DEN-grafted IDA electrode (B). The potential of generator electrodes of the bare IDA and the Pt DEN-grafted IDA electrode was swept and the potential of collector electrodes of the bare IDA and the Pt DEN-grafted IDA electrode was held at -0.8 and -0.6 V, respectively. Scan rate was $5 \text{ mV} \cdot \text{s}^{-1}$186

[Fig. 6-1] An optical microscope image of ITO micropatterns obtained during microfabrication. The microscope image was obtained with unmodified three parts of ITO micropatterns (WE = working electrode, RE = reference electrode, CE = counter electrode).200

[Fig. 6-2] Linear sweep voltammograms of 10 mM $\text{CrCl}_3 \cdot 6\text{H}_2\text{O}$ (scan rate $0.1 \text{ V} \cdot \text{s}^{-1}$) at the ITO electrode.206

[Fig. 6-3] Optical microscope images of ITO micropatterns

after Cr electrodeposition with different deposition time. ...	207
[Fig. 6-4] Linear sweep voltammograms of 10 mM $\text{H}_2\text{PtCl}_6 \cdot 6\text{H}_2\text{O}$ (scan rate $0.1 \text{ V} \cdot \text{s}^{-1}$) at the ITO electrode.	208
[Fig. 6-5] Optical microscope images of ITO micropatterns after Pt electrodeposition with various conditions of applying voltage and deposition time.	209
[Fig. 6-6] An optical microscope image of ITO micropatterns after $\text{L}_2\text{-ePt}$ electrodeposited for 2500 s.	213
[Fig. 6-7] An optical microscope image of ITO micropatterns after $\text{L}_2\text{-ePt}$ electrodeposited for 500 s.	214
[Fig. 6-8] Cyclic voltammograms obtained on $\text{L}_2\text{-ePt/ITO}$ surface in 10 mM $m\text{-PD}$ solution containing 10 mM PBS (pH 7.4) solution. Scan rate was $4 \text{ mV} \cdot \text{s}^{-1}$	215
[Fig. 6-9] Open circuit potential of poly- $m\text{-PD/L}_2\text{-ePt}$ electrode measured in 10 mM PBS solution at pH 7.4.	216
[Fig. 6-10] An optical microscope image of ITO micropatterns obtained during microfabrication of the integrated three-electrode system.	219
[Fig. 6-11] Cyclic voltammograms obtained in 1 mM $\text{Fc}(\text{MeOH})_2$ containing 2 M KCl, using a ITO as a working electrode and Pt electrodeposited on ITO surface as a counter electrode and Ag/AgCl (solid line) or poly- $m\text{-PD/L}_2\text{-ePt}$ (dotted line) as a reference electrode.	220
[Fig. 6-12] Cyclic voltammograms obtained in 1 mM $\text{Fc}(\text{MeOH})_2$ containing 2 M KCl, using a ITO IDA electrode as a working electrode and Pt electrodeposited on ITO surface as a counter electrode and Ag/AgCl (solid line) or poly- $m\text{-PD/L}_2\text{-ePt}$	

ePt (dotted line) as a reference electrode. Scan rate was 5 mV · s ⁻¹	221
[Fig. A-1] Overall mask layout.	231
[Fig. A-2] Single sensor mask layout.	232
[Fig. A-3] Mask layout of part of the integrated three- electrode system structure.	232
[Fig. B-1] Potential of the working electrode during one voltammetric cycle. The potential is cycled between the vertex potentials -0.4 V and +0.4 V. Scan rate is 1 mV · s ⁻¹	238
[Fig. B-2] Cyclic voltammetry recorded at a 3D IDA electrode.	239
[Fig. B-3] Model geometry.	246
[Fig. B-4] Customized mesh used for the 3D IDA analysis.	256

1. Introduction

1.1. Background and Overview

With the development of life sciences and biomedical technologies, the detection of biomolecules with low abundance and the acquisition of ultraweak biological signals have become a bottleneck in these fields. Therefore, there is an urgent need to develop highly sensitive analytical methods coupled with the specificity of biological recognition events [1]. However, owing to the inherent background signals of various analytical instrumentals and limitations of classical analytical methodologies, improving the sensitivities via either traditional physical methods or simple chemical and biocatalytic processes seems remote in terms of meeting the practical demands. Progress in nanotechnology and biotechnology has led to convenient and promising ways for developing novel analytical methods with high sensitivity. As a result, a series of novel signal amplification strategies have been recently designed using various materials and molecular biology methods [2]. By combining these strategies with biosensors and biochips, many practical bioanalytical methods and biosensing technologies have been proposed.

Achieving ultrahigh sensitivity requires innovative approaches that can be coupled with different amplification platforms and processes. Nanotechnology offers unique opportunities for creating highly sensitive and innovative biosensing devices and ultrasensitive bioassays. Generally, signal amplification strategies are based on functional materials employing appropriate labels. The unique optical [3–6], photophysical [7], electronic [8], and catalytic [9–11] properties of functional materials turn them into ideal labels for biorecognition and biosensing processes. There are six ways to achieve this as mentioned herein. i) Accelerating the electron transfer or obtaining a sensitized optical signal by taking advantage of the good conductivity and unique optical characteristics of micro/nano materials. ii) Achieving optical, electrical or visual analysis by using the catalytic and enzyme mimetic functions of micro/nano materials. This method has been applied for the analysis of small biomolecules, proteins, and genes. iii) Developing stripping voltammetry, electrochemiluminescence, fluorescence or mass spectrometry analysis by using the tag molecules [12,13]; for example, the electrochemiluminescent behaviors of quantum dots. These tags

can be further amplified by ordered assembly, click chemistry or direct synthesis of the multiple quantum dots in the framework of either dendrimer or polymer. iv) Various materials are used as the carriers of signaling molecules, which include both redox active and optical molecules with fluorescence, or infrared, ultraviolet, and Raman adsorptions. Catalysts such as enzymes can also be employed as signaling molecules, because they accelerate the chemical or biological reactions to enhance the signals or produce molecules with redox activity or optical character. v) Taking advantage of the optical–electrical properties of nanomaterials to realize either electrochemiluminescent or photoelectrochemical signal amplification, which promotes the rapid development. vi) Selective concentration of the chemicals and biomolecules with low abundance by using biofunctionalized materials and various techniques.

These novel signal amplification strategies have been used in various electrochemical detections such as voltammetric analysis, impedance analysis, capacitance analysis, electro–chemiluminescent analysis, and photoelectrochemical analysis; optical detections such as chemiluminescent analysis,

fluorescent analysis and infrared, ultraviolet, and Raman analysis; mass spectrometric analysis and development of imaging technologies such as grayscale scanning imaging, scanning electrochemical microscopy imaging, chemiluminescence imaging, fluorescence imaging, Raman spectral imaging and mass spectral imaging. When introducing these strategies in biosensors and biochips, the established methods can conveniently be used for the detections of chemicals, small biomolecules, proteins, cells, and carbohydrate sites on cell surfaces [14]. Some methods can even realize quasi-single-molecule detection. Coupled with a protein array and CCD, the developed chemiluminescence imaging techniques can greatly increase the number of detection channels and improve the detection throughput. Furthermore, as a result of the competition among the primary target surface, secondary signal surface, and ensuing silver enhancement, an information transfer strategy has been proposed for the visualization of the target. More recently, a method for the target-cell-specific delivery, imaging, and detection of intracellular microRNA using multifunctional nanoprobe has been proposed [15].

Results of the research on (bio)sensors till date show that

chemical approaches towards sensing need to rely on signal amplification in order to detect analytes at ultralow concentrations. The primary objectives of this dissertation were to develop new strategies for signal amplification in chemical/bio sensors for sensitive sensing applications, and improve the analytical performance of the electrochemical system in heterogeneous redox catalysis and miniaturization. This thesis is organized into five main chapters. In chapter 2, we present a unique method for the sensitive and selective detection of Hg^{2+} ions using DNA-modified gold microshells, which can be individually manipulated using a micropipette and act as a micro SERS probe for the analysis of small sample volumes. Chapter 3 presents the development and implementation of an indirect detection assay leveraging electrokinetic trapping to preconcentrate and indirectly detect non fluorescent analytes on a microfluidic chip. In chapter 4, we discuss electrochemical redox cycling based on three-dimensional interdigitated array (3D IDA) electrodes for signal amplification to enhance the sensitivity of chip-based immunosensors. Chapter 5 presents a method for constructing functional nanostructures, which showed electrocatalytic

activity for *p*-aminophenol redox reaction, indium tin oxide (ITO) surfaces by decorating the ITO surfaces with two different types of dendrimers. In chapter 6, we present a reliable three-electrode system fabricated on a microchip. The optimization of the parameters pertaining to the reference electrode fabrication and micro system operation has been described in this chapter. The analytical performance of our three-electrode system microchip was successfully demonstrated by analyzing common electroactive species. Finally, chapter 7 summarizes the conclusions and contributions of this work.

1.2. References

- [1] H. Ju, X. Zhang, J. Wang, *NanoBiosensing, Principles, Development and Application*, Biological and Medical Physics, Biomedical Engineering, **2011**.
- [2] J. Lei, H. Ju, *Chem. Soc. Rev.* **2012**, *41*, 2122.
- [3] P. Mulvaney, *Langmuir* **1996**, *12*, 788.
- [4] M. M. Alvarez, J. T. Khoury, T. G. Schaaff, M. N. Shafigullin, I. Vezmar, R. L. Whetten, *J. Phys. Chem. B* **1997**, *101*, 3706.
- [5] A. P. Alivisatos, *J. Phys. Chem.* **1996**, *100*, 13226.
- [6] L. E. Brus, *Appl. Phys. A Mater.* **1991**, *53*, 465.
- [7] A. N. Shipway, E. Katz, I. Willner, *ChemPhysChem* **2000**, *1*, 18.
- [8] R. F. Khairutdinov, *Colloid J.* **1997**, *59*, 535.
- [9] L. N. Lewis, *Chem. Rev.* **1993**, *93*, 2693.
- [10] V. Kesavan, P. S. Sivanand, S. Chandrasekaran, Y. Kolytyn, A. Gedanken, *Angew. Chem., Int. Ed.* **1999**, *38*, 3521.
- [11] R. Ahuja, P.-L. Caruso, D. Möbius, W. Paulus, H. Ringsdorf, G. Wildburg, *Angew. Chem., Int. Ed.* **1993**, *33*, 1033.
- [12] G. Lai, J. Wu, H. Ju, F. Yan, *Adv. Funct. Mater.* **2011**, *21*, 2938.
- [13] L. Ding, W. Cheng, X. Wang, S. Ding, H. Ju, *J. Am. Chem.*

Soc. **2008**, *130*, 7224.

[14] W. Cheng, L. Ding, S. Ding, Y. Yin, H. Ju, *Angew. Chem., Int. Ed.* **2009**, *48*, 6465.

[15] H. Dong, J. Lei, H. Ju, F. Zhi, H. Wang, W. Guo, Z. Zhu, F. Yan, *Angew. Chem., Int. Ed.* **2012**, *51*, 4607.

2. Mercury (II) Detection by SERS based on a Single Gold Microshell

2.1. Introduction

Surface-enhanced Raman scattering (SERS) is a powerful spectroscopy technique that can provide non-destructive and ultrasensitive characterization down to single molecular level, comparable to single-molecule fluorescence spectroscopy [1–10]. However, conventional substrates based on metals such as Ag, Au and Cu are required to either have roughened surfaces or be in the form of nanoparticles for a substantial SERS effect. This has severely limited the wide applications of SERS for practical purposes. Since the nanoparticles are invisible by conventional optical microscopy, it is difficult to place them on the point of interest and to ensure they are present. Individual nanoparticles are too small to be manipulated, and thus hard to remove from the surface after SERS measurements.

In our previous research, we demonstrated that the gold shell on a polystyrene microsphere 2 μm in diameter resulted in a strong SERS-active platform [11]. The gold microshell is larger than the conventional nanoparticles that have been

reported as SERS-active materials, while it has the smallest dimension that can be routinely recognized by a conventional optical microscope. In addition, the gold microshells can be easily and individually manipulated under a conventional optical microscope using a micropipette. The diameter of the gold microshell is comparable with that of the focal volume of a focused laser that is normally used for SERS measurements. To take advantage of the favorable features of the gold microshells, we demonstrated the potential of an on-chip microfluidic SERS decoding strategy for a micro-suspension array [12]. This system is based on the respectively encoded gold microshells by combination with a couple of the SERS tags. The SERS from the specially tailored surfaces was so strong that decoding of a microshell flowing in a microchannel needed only 1 ms.

Of particular interest has been detection of mercury, a highly toxic element that exists in metallic, inorganic, and organic forms. It is beyond question that mercury(II) ions are a widespread toxic contaminant in aquatic ecosystems and pose severe risk to human health and the environment [13,14].

In spite of many methods that have been developed, a method for sensitive and selective mercury detection in health and

environmental problems is much in demand. Recently, a great deal of effort has been exerted to develop Hg^{2+} ion sensors using organic chromophores [15], fluorophores [16,17], oligonucleotides [18,19], DNAzymes [20], conjugated polymers [21], microcantilevers [22], electrochemical methods [23], quantum dots [24], and gold nanoparticles (AuNPs) [25,26]. However, there remain limitations associated with the previously reported sensors with regard to their practical uses: insufficient selectivity and sensitivity, and interference from other competing metals. In these respects, SERS receives particular attention because it produces molecule-specific spectra which allow facile identification of the molecular analyte in an aqueous mixture without extensive separation procedures [27]. de Mello et al. recently reported spectroscopic detection of Hg^{2+} ions using the affinity between AuNPs and mercury(II) ions [28]. This method involves the use of droplet-based microfluidics combined with SERS detection. Despite these advances, there has been relatively little progress toward the development of selective, practical and ‘turn-on’ signaling type spectroscopic methods for detection of Hg^{2+} ions. Inspired by the strong SERS enhancement surface and the characteristic

size of the gold microshells, we propose a new way to detect Hg^{2+} ions. The SERS probe fabricated in this work is an oligonucleotide–modified gold microshell, which is inexpensive and can be easily and precisely manipulated. It allows highly sensitive and selective screening of Hg^{2+} ions from a small volume of given sample solution.

2.2. Experimental

2.2.1. Materials and reagents

Thiolated tetramethylrhodamine (TAMRA)-tagged DNA oligomer was purchased from BIONEER Corporation (Daejeon, Korea). The sequence of this modified oligomer was 5'-HS-(CH₂)₆-CTT GTT TCT CCC CCC TGT TTC TTG-TAMRA-3', containing a thiol at 5' and tetramethylrhodamine at 3'. Amine-terminated polystyrene bead (PS-NH₂) was procured from Bangs Laboratories, Inc. (Fishers, IN, USA) and used as received. Absolute ethanol was purchased from Merck Chemicals (Darmstadt, Germany). Mercury perchlorate, other metal perchlorate salts, Tris-(2-carboxyethyl) phosphine hydrochloride (TCEP), sodium phosphate monobasic, formaldehyde, Tetrakis(hydroxymethyl)phosphonium chloride (THPC), hydrogen tetrachloroaurate (III) trihydrate were obtained from Aldrich (Milwaukee, WI, USA). Sulfuric acid and hydrogen peroxide were purchased from J. T. Baker (Phillipsburg, NJ, USA) and used without further purification. Deionized double distilled water was used to prepare all the solutions.

2.2.2. Preparation of gold microshells

2.2.2.1. Gold nanoparticle synthesis

AuNPs were synthesized by following a procedure reported previously. Sodium hydroxide (0.5 mL, 1 M) in water and 1 mL of THPC solution (prepared by adding 12 μ L of 80% THPC in water) were added to 45 mL of deionized H₂O and stirred. Next, HAuCl₄ trihydrate (2.0 mL, 27 mmol) in water was added quickly to the solution and was stirred for 5 min. The color of the solution changed from colorless to brown. The resulting brown solution was stored in refrigerator at 4°C when not used immediately.

2.2.2.2. Attachment of AuNP seed layers to amine-terminated polystyrene beads (PS-NH₂)

0.5 mL of PS-NH₂ solution and 5 mL water were mixed in a centrifuge tube. The mixture was centrifuged at 2000 rpm for 5 min and redispersed in water after the supernatant was removed. The PS-NH₂ solution was washed three more times and then redispersed in 5 mL water. After drying overnight in a vacuum oven, the PS-NH₂ (0.05 g) and 0.5 mL water were mixed in a centrifuge tube to prepare 10% PS-NH₂ dispersed

in water. The PS-NH₂ solution was sonicated until PS-NH₂ was well dispersed in water. And then, 5 mL of colloidal AuNPs were added to the PS-NH₂ solution. The centrifuge tube was shaken gently for a few minutes and then kept quiescent for 2 h. The mixture solution was centrifuged at 2000 rpm for 5 min and the supernatant was decanted before 5 mL water was added. The sequential processes of centrifugation, decanting, and adding water were repeated several times. Finally the slightly red particles (PS-NH₂/AuNP) were dispersed again in 5 mL water. The solution was stored in refrigerator at 4°C, when not used immediately.

2.2.2.3. Preparation of electroless Au plating solution

Potassium carbonate (250 mg, 0.018 mmol) was dissolved in 1000 mL of water in a reaction bottle. To an aqueous solution of potassium carbonate was added 15 mL of 1% HAuCl₄ under stirring. The color of the solution changed from pale yellow to colorless. This colorless solution was used in the electroless plating steps for gold microshells formation.

2.2.3. Functionalization of gold microshells with ss-DNA

1 mg gold microshell was dispersed in 1 mL of 10% ethanol aqueous buffer solution (10 mM PBS, pH 7.4). For the preparation of DNA–modified gold microshell, the ss–DNA was incubated for 1 h in 1 mM TCEP to reduce disulfide bound oligomer. DNA–modified gold microspheres were synthesized by incubating 100 μ M of ss–DNA in 1 mL of the gold microshell solution. The final concentration of oligonucleotide was 3 μ M. After standing for 48 h at room temperature, the samples were centrifuged and dispersed in 1 mL of 10% ethanol aqueous buffer solution (10 mM PBS, pH 7.4).

2.2.4. Trapping a DNA–modified single gold microshell at the tip of the micropipette and manipulation

Micropipettes were fabricated by heating and pulling borosilicate glass capillaries (Harvard Apparatus Inc., GC150F–10) in a laser–based micropipette puller device (Sutter Instruments Inc., P–2000) and stored in a petri dish on the top of an adhesive tape. At first, a DNA–modified single gold microshell placed on a slide glass. It follows that the DNA–modified single gold microshell on the slide glass was trapped at the end of a micropipette by pulling gently and

released into a small drop of Hg^{2+} ion solution. SERS spectra of the DNA-modified gold microshell were obtained by focusing the Raman laser probe through an optical microscope.

2.2.5. Instruments

SERS spectra were obtained using a homemade Ramboss Micro-Raman system spectrometer with a 632.8 nm line from a 20 mW He/Ne laser (Model LGK7665) as the excitation source. The homemade Ramboss Micro-Raman system spectrometer was equipped with a TE cooled (-50°C) charged-coupled device (CCD) camera (1024×128 pixels). The laser beam was focused on a spot approximately $2 \mu\text{m}$ in diameter through an objective lens of $\times 100$ magnification. The grating (1200 grooves mm^{-1}) and the slit provided a spectral resolution of 4 cm^{-1} . Calibration of the spectrometer was conducted using the Raman band of a silicon wafer at 520 cm^{-1} , with which the peak intensities of the adsorbates on gold microshells were normalized. Field Emission-Scanning Electron Microscopy (FE-SEM) measurements were made using a Hitachi S-4800 at an accelerating voltage of 15 kV.

2.3. Results and Discussion

2.3.1. Principle of sensor operation

The sensing principle is the conformational change of the nucleic acid strands that are immobilized on a gold microshell. It is analogous to the molecular beacon which involves a thymine (T)-rich single-stranded DNA (ssDNA) through specific T-Hg²⁺-T complex formation. It was reported that the Hg²⁺ ion can selectively bind between thymine bases of the two strands and promote these T-T mismatches to form stable T-Hg²⁺-T base pairs [29]. Applying this phenomenon to the specific strands on the mobile gold microshells, the presence of Hg²⁺ ions in the sample solution triggers generation of SERS signals, which is a sensitive function of the distance between the gold microshell surface and the Raman tags at the end of the oligonucleotide strands. The gold microshells, 2 μm in diameter, were fabricated by a three-step procedure. Briefly, colloidal gold nanoparticles were synthesized by following a procedure reported previously [30] and attached to amine-terminated polystyrene beads (PS-NH₂) as seed layers [31]. The microbeads as-prepared were electroless-plated in a gold-plating solution in the presence of reducing reagents.

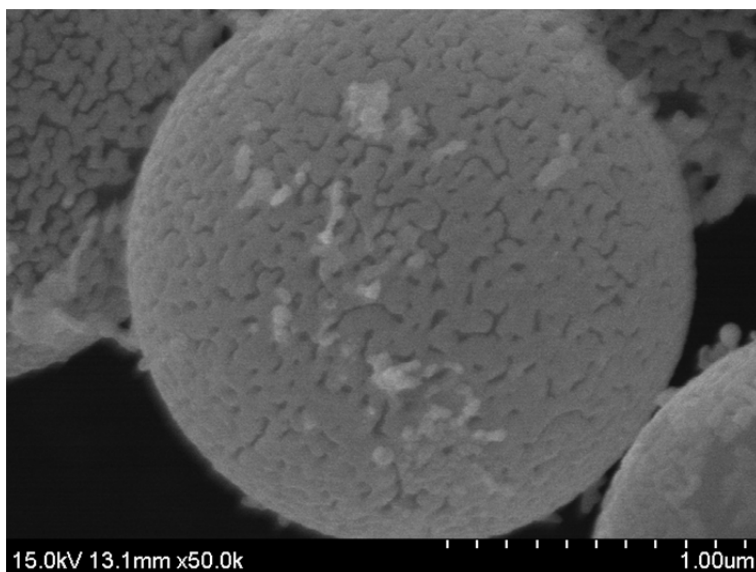


Fig. 2-1 Scanning electron microscopy (SEM) image of gold microshells composed of (PS-NH₂/AuNPs) with the diameter of 2 µm.

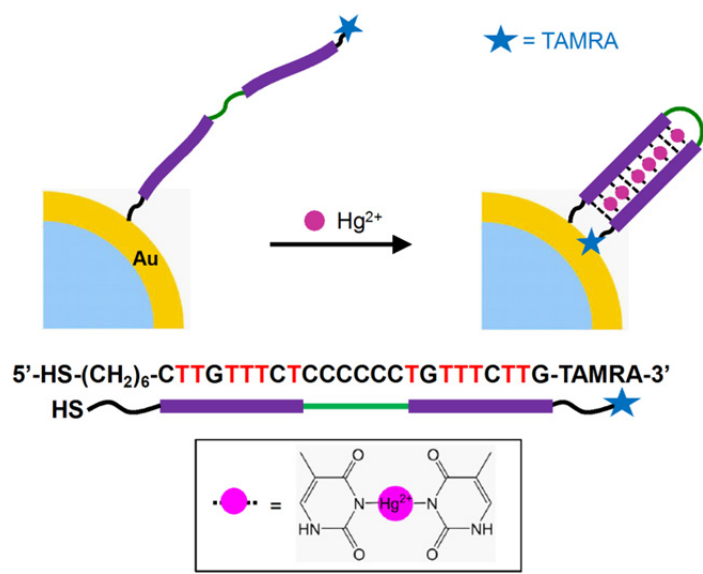


Fig. 2-2 Schematic description of the SERS sensor for Hg²⁺ ion detection.

The gold microshells were checked by scanning electron microscopy (SEM) as shown in Fig. 2-1. The sequence of the probe DNA was 5'-HS-(CH₂)₆-CTT GTT TCT CCC CCC TGT TTC TTG-tetramethylrhodamine-3'. The probe DNA was doubly labelled with thiol and tetramethylrhodamine (TAMRA) at the 5'- and the 3'-end, respectively, and this could be spontaneously immobilized on the gold microshell surface and produce SERS signals. The Hg²⁺ ion sensing strategy is simple and is illustrated in Fig. 2-2. In the absence of Hg²⁺ ions, the probe DNA is in an open conformation and the average distance between TAMRA as a Raman reporter and the surface is expected to be relatively large. In the presence of Hg²⁺ ions, the probe DNA folds into the T-Hg²⁺-T mediated hairpin structure and this conformational change draws the TAMRA moiety close to the surface. The Raman reporters in the vicinity of the gold surface, which was specially tailored, are much more likely to produce strong SERS signals. The spectra in Fig. 2-3 were collected from individual DNA-modified gold microshells on a glass slide. Every DNA-modified gold microshell can easily be recognized through a conventional optical microscope (inset in Fig. 2-3), and a laser beam can be

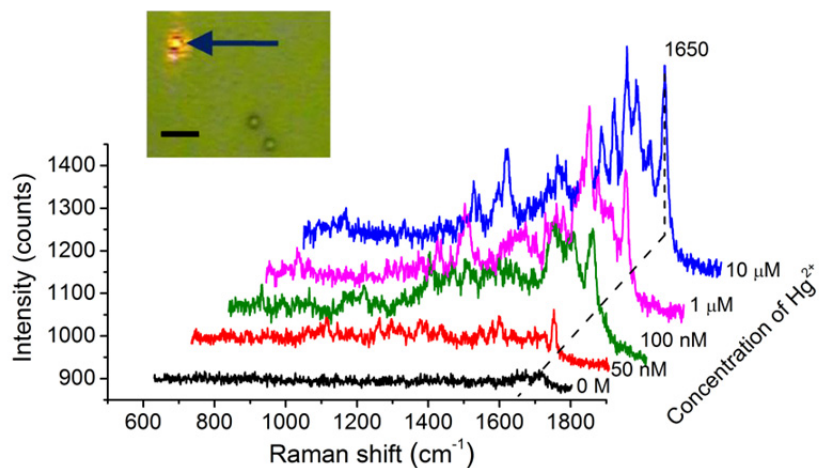


Fig. 2–3 SERS spectra obtained from DNA–modified gold microspheres at a variety of Hg^{2+} ion concentrations. The most prominent peak of TAMRA is observed at 1650 cm^{-1} . Inset: An optical microscopic image of DNA–modified gold microspheres placed on a slide glass. The laser probe is indicated by an arrow. Scale bar in an inset is $10\ \mu\text{m}$.

focused on the center of a single DNA–modified gold microshell. Considering the focal volume of the laser beam, the size of a single gold microshell corresponds to the largest scale of the spherical SERS–active substrate that is generated from its entire surface. Beads larger than the gold microshells employed in this study give SERS signals from only part of their surface. Beads smaller than the gold microshells are hard to see, manipulate, and remove from the surface. On the other hand, the gold microshells in this study are the smallest beads that can be individually handled by currently available manipulating tools operating under a conventional optical microscope.

2.3.2. Sensitivity of Hg^{2+} sensor

The spectra in Fig. 2–3 show the change in SERS intensity as a function of Hg^{2+} ion concentration. The increasing trend of SERS signals in response to augmented Hg^{2+} ion concentration is in good accordance with the expected mechanism shown in Fig. 2–2. This result strongly supports the suggested scenario that the locked hairpin structure and the TAMRA Raman–active probe located close to the gold microshell surface leads to an increased SERS signal from the TAMRA Raman reporters. The

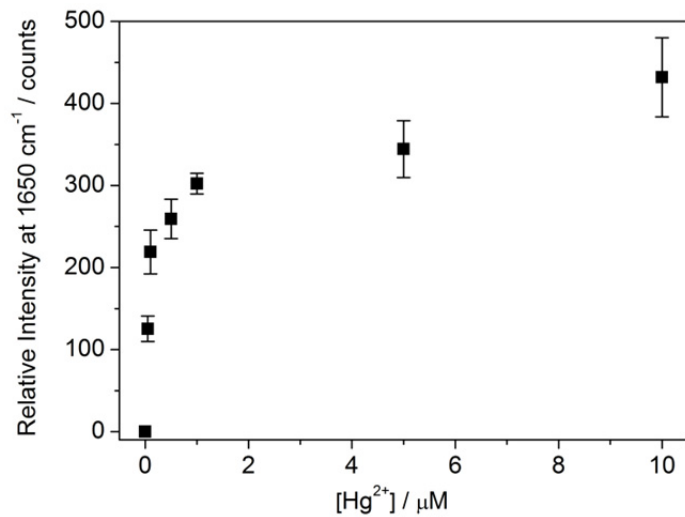


Fig. 2-4 A calibration curve for Hg^{2+} ions. The error bars denote the standard deviations taken from at least four independent measurements.

limit of detection is estimated to be 50 nM. The SERS intensity is saturated above several μM of Hg^{2+} ions. Although the dynamic range is below micromolar concentration, highly selective detection of Hg^{2+} ions in the presence of excess interfering ions is not reproducible enough to be applied for practical uses. Improvement in analytical aspects such as further enhancement in SERS signals and metal ion preconcentration are expected to lead to detection of even lower concentrations of Hg^{2+} ions than is shown in this study, with high precision.

2.3.3. Selectivity of Hg^{2+} sensor

The selectivity of the sensor was determined in the presence of various competing divalent metal ions such as Mg^{2+} , Ca^{2+} , Ba^{2+} , Mn^{2+} , Fe^{2+} , Co^{2+} , Ni^{2+} , Cu^{2+} , Zn^{2+} , Cd^{2+} , and Pb^{2+} at 50 μM concentrations (Fig. 2–5). Among the metal ions tested, Hg^{2+} shows exceptionally high changes in SERS intensity compared to the other metal ions. Likewise the response of this micro-SERS sensor to Hg^{2+} ions is unaffected by the presence of a mixture of metal ions.

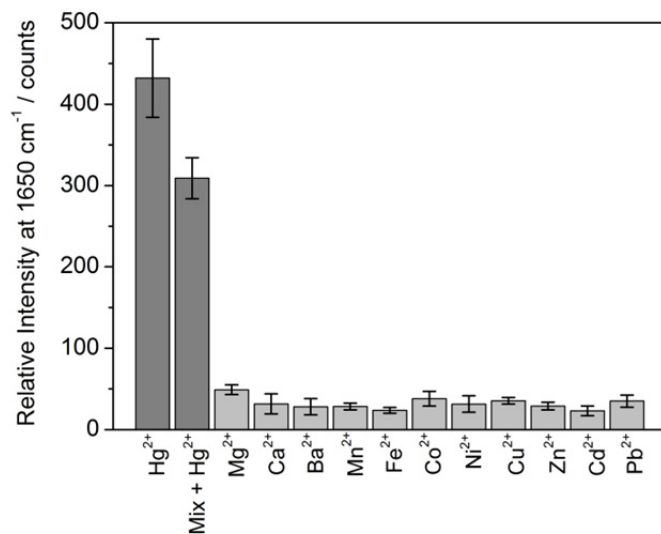


Fig. 2–5 Selectivity of our SERS probe over various divalent metal ions (10 μM for Hg^{2+} and 50 μM for other metal ions) and a mixture of metal ions (10 μM each of Mg^{2+} , Ca^{2+} , Ba^{2+} , Mn^{2+} , Fe^{2+} , Co^{2+} , Ni^{2+} , Cu^{2+} , Zn^{2+} , Cd^{2+} , Pb^{2+} plus Hg^{2+}). The error bars represent the standard deviations taken from at least four independent measurements.

2.3.4. Application for small volume analysis

Individual manipulation of a single gold microshell is a useful advantage for a mobile SERS probe. This feature indicates that a single gold microshell could be translocated to any place of interest where it is desired to obtain a SERS spectrum. The single DNA-modified gold microshell in this work is small enough to be immersed in a sub-microliter solution and thereby expected to possibly give SERS spectra corresponding to the analytes in a small sample volume. The ability to detect mercury(II) ions in a sample solution was probed by using a single DNA-modified gold microshell, which was carried by a micropipette linked to a micro-manipulator. The single DNA-modified gold microshell was trapped at the end of a micropipette tip (Fig. 2-6), and then dipped into 5 μL of Hg^{2+} solution. The SERS spectrum from the single DNA-modified gold microshell successfully indicates the presence of Hg^{2+} ions in the sample solution.

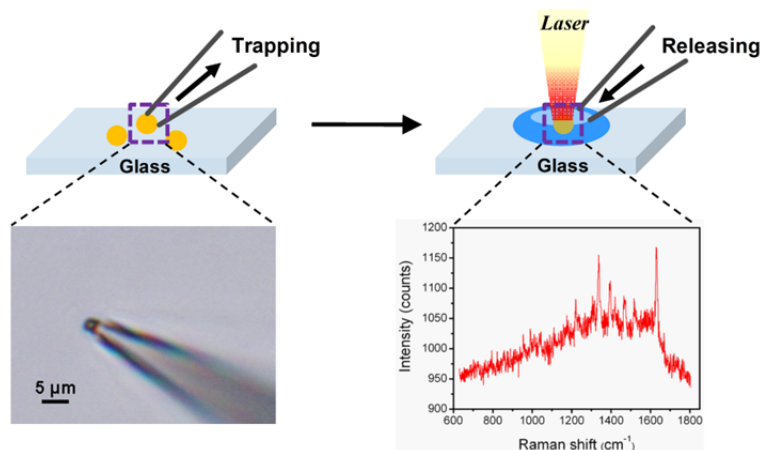


Fig. 2-6 Scheme of transferring and placing a single DNA-modified gold microshell on the point of interest. DNA-modified gold microspheres sprinkled on a glass slide, trapped at the tip end of a micropipette (gray), and then released into the Hg^{2+} solution (blue) of small volume. An optical microscope image shows a DNA-modified single gold microshell at the end of a micropipette tip. The SERS spectrum was obtained from the DNA-modified single gold microshell after reaction with 5 μL of the 10 μM Hg^{2+} ion solution.

2.4. Conclusion

We have demonstrated a SERS micro-probe for the detection of mercury(II) ions based on a single DNA-modified gold microshell. The underlying principle is simple but the results are clear and show sensitive and selective mercury(II) ion detection, as demonstrated by the detection limit of 50 nM and negligible response to other metal ions. The single DNA-modified gold microshell can be individually recognized and manipulated under a conventional optical microscope. The DNA-modified single gold microshell can be precisely translocated into a Hg^{2+} ion solution using a typical micropipette and plays the role of a sensitive SERS probe responding to the Hg^{2+} ions in small sample volumes. The proposed strategy and analytical method in this work offers a new opportunity for small volume analysis of not only Hg^{2+} ions but also toxic metal ions in environmental and biological samples.

2.5. References

- [1] S. Nie, S. R. Emory, *Science* **1997**, *275*, 1102.
- [2] K. Kneipp, Y. Wang, H. Kneipp, L. T. Pereman, I. Itzkan, R. R. Dasari, M. S. Feld, *Phys. Rev. Lett.* **1997**, *78*, 1667.
- [3] J. P. Camden, J. A. Dieringer, J. Zhao, R. P. Van Duyne, *Acc. Chem. Res.* **2008**, *41*, 1653.
- [4] Y. W. C. Cao, R. Jin, C. A. Mirkin, *Science* **2002**, *297*, 1536
- [5] Z. Chen, S. M. Tabakman, A. P. Goodwin, M. G. Kattah, D. Daranciang, X. Wang, G. Zhang, X. Li, Z. Liu, P. J. Utz, K. Jiang, S. Fan, H. Dai, *Nat. Biotechnol.* **2008**, *26*, 1285.
- [6] D. Graham, D. G. Thompson, W. E. Smith, K. Faulds, *Nat. Nanotechnol.* **2008**, *3*, 548.
- [7] P. K. Jain, X. Huang, I. H. El-Sayed, M. A. El-Sayed, *Acc. Chem. Res.* **2008**, *41*, 1578.
- [8] X. Qian, X.-H. Peng, D. O. Ansari, Q. Yin-Goen, G. Z. Chen, D. M. Shin, L. Yang, A. N. Young, M. D. Wang, S. Nie, *Nat. Biotechnol.* **2008**, *26*, 83.
- [9] Z.-Q. Tian, B. Ren, J.-F. Li, Z.-L. Yang, *Chem. Commun.* **2007**, 3514.
- [10] Y. Wang, H. Wei, B. Li, W. Ren, S. Guo, S. Dong, E. Wang, *Chem. Commun.* **2007**, 5220.

- [11] L. Piao, S. Park, H. B. Lee, K. Kim, J. Kim, T. D. Chung, *Anal. Chem.* **2010**, *82*, 447.
- [12] S. Lee, S. Joo, S. Park, H. C. Kim, T. D. Chung, *Electrophoresis* **2010**, *31*, 1623.
- [13] Q. Wang, D. Kim, D. D. Dionysiou, G. A. Sorial, D. Timberlake, *Environ. Pollut.* **2004**, *131*, 323.
- [14] E. M. Nolan, S. J. Lippard, *Chem. Rev.* **2008**, *108*, 3443.
- [15] E. Coronado, J. R. Galan–Mascaros, C. Marti–Gastaldo, E. Palomares, J. R. Durrant, R. Vilar, M. Gratzel, M. K. Nazeeruddin, *J. Am. Chem. Soc.* **2005**, *127*, 12351.
- [16] H. N. Kim, M. H. Lee, H. J. Kim, J. S. Kim, J. Yoon, *Chem. Soc. Rev.* **2008**, *37*, 1465.
- [17] J. S. Kim, D. T. Quang, *Chem. Rev.* **2007**, *107*, 3780.
- [18] A. Ono, H. Togashi, *Angew. Chem., Int. Ed.* **2004**, *43*, 4300.
- [19] Z. Zhu, Y. Su, J. Li, D. Li, J. Zhang, S. Song, Y. Zhao, G. Li, C. Fan, *Anal. Chem.* **2009**, *81*, 7660.
- [20] J. Liu, Y. Lu, *Angew. Chem., Int. Ed.* **2007**, *46*, 7587.
- [21] X. Liu, Y. Tang, L. Wang, J. Zhang, S. Song, C. Fan, S. Wang, *Adv. Mater.* **2007**, *19*, 1471.
- [22] X. Xu, T. G. Thundat, G. M. Brown, H.–F. Ji, *Anal. Chem.*

2002, 74, 3611.

[23] D. Han, Y.-R. Kim, J.-W. Oh, T. H. Kim, R. K. Mahajan, J. S. Kim, H. Kim, *Analyst* **2009**, 134, 1857.

[24] R. Freeman, T. Finder, I. Willner, *Angew. Chem., Int. Ed.* **2009**, 48, 7818.

[25] Y.-R. Kim, R. K. Mahajan, J. S. Kim, H. Kim, *ACS Appl. Mater. Interfaces* **2010**, 2, 292.

[26] B.-C. Ye, B.-C. Yin, *Angew. Chem., Int. Ed.* **2008**, 47, 8386.

[27] C. H. Munro, W. E. Smith, P. C. White, *Analyst* **1995**, 120, 993

[28] G. Wang, C. Lim, L. Chen, H. Chon, J. Choo, J. Hong, A. J. de Mello, *Anal. Bioanal. Chem.* **2009**, 394, 1827.

[29] Y. Miyake, H. Togashi, M. Tashiro, H. Yamaguchi, S. Oda, M. Kudo, Y. Tanaka, Y. Kondo, R. Sawa, T. Fujimoto, T. Machinami, A. Ono, *J. Am. Chem. Soc.* **2006**, 128, 2172.

[30] T. Pham, J. B. Jackson, N. J. Halas, T. R. Lee, *Langmuir* **2002**, 18, 4915.

[31] S. L. Westcott, S. J. Oldenburg, T. R. Lee, N. J. Halas, *Langmuir* **1998**, 14, 5396.

3. Electrokinetic Concentration on a Microfluidic Chip using Polyelectrolytic Gel Plugs for Small Molecule Immunoassay

3.1. Introduction

The characterization of trace amounts of biologically active small molecules (molecular weight less than 1000 Da) is critical in clinical and environmental analyses [1,2]. Many small molecules such as steroid/thyroid hormones, catecholamine, eicosanoids, and synthetic drugs/herbicides act as important agonists or antagonists of specific target proteins [3]. As such, the small molecule–biomacromolecule interaction constitutes one of the most significant biological networks, encompassing protein–drug, protein–ligand, and enzyme–substrate complexes [4]. Conventional characterization methods for collection, identification, and/or quantitative analysis of small molecule–biomacromolecule interactions such as affinity chromatography [5], mass spectrometry [6], capillary electrophoresis [7], surface plasma resonance [8], nuclear magnetic resonance [9], and X–ray crystallography are available. However, most of these methods involve labor intensive, time–consuming, or

complicated processes for sample preparation.

In general, immunoassay methods can be categorized into two, i.e. competitive and noncompetitive immunoassays. The competitive immunoassay has been mostly employed to analyze small molecules [10], which rarely have more than one distinct epitopes required for detection by noncompetitive immunoassays, representatively, sandwich-type assay. However, the sensitivity of the competitive immunoassays is much lower than sandwich-type immunoassay and severely relies on the affinity of antibodies [11]. In this regard, there have been many attempts to develop antibodies with higher antigen-binding affinities [12]. These efforts include genetic manipulation of antibodies and *in vitro* affinity maturation of antibodies [13]. Seeking new procedures is another strategy to improve the sensitivity of the competitive immunoassays that are applicable to small molecules. Recently a single-chain variable-fragment library was selected by the phage-display method for the discovery of a general or specific recognition module, and the analog which can differentiate the binding profile toward small molecule was rationally designed [14]. It requires no sophisticated antibody engineering to synthesize

artificial antibodies with better affinity.

Preconcentration of the sample prior to analysis is a crucial step in microfluidic systems because it can directly lead to lower detection limit. There are many techniques available for sample preconcentration in microfluidic devices, including isotachopheresis [15–17], isoelectric focusing [18–21], field-amplified sample stacking [22–24], solid-phase extraction [25–27], electrokinetic trapping [28–37], and temperature-gradient focusing [38]. Among such a variety of preconcentration schemes, electrokinetic trapping has received particular attention since the first demonstration at the interface between a micro- and nanochannel on a microfluidic chip [39]. There was another approach based on concentration polarization [40]. By creating an electric double-layer (EDL) overlap in charged nanochannels or nanoporous polymers, co-ions were excluded so that the nanostructure acted as a counterion permselective channel. When an electric field was applied across the ion-permselective nanochannel, local electric field gradients and the corresponding concentration polarization allowed sample preconcentration. With a simple fluid-handling protocol, this process enabled highly efficient

analysis of any charged biomolecules on a microfluidic chip.

In our previous research, we brought polyelectrolytic gel electrode (PGE) into microfluidic chip systems for a variety of applications, *e.g.* velocimetry/cytometry [41], iontronic diodes/logic gates [42], complete blood cell counter [43], ultra-fast iondepletion micromixer [44], and efficient preconcentrator [45,46]. The PGEs were photopolymerized in glass microfluidic channels and exhibited desirable properties for ion engineering including low impedance, high frequency response, good reproducibility and long-term stability. Highly charge-selective polymer [poly-2-acrylamido-2-methyl-1-propanesulfonic acid (pAMPSA)] for electrokinetic trapping possesses particularly useful characteristics for microfluidic preconcentration based on the phenomenon of concentration polarization [45]. In principle, the negatively charged polyelectrolytic gel (pAMPSA) plugs facing each other can be easily photopolymerized in the microchannel. Due to the anionic charge of the polyelectrolyte backbones, cations are selectively permitted to pass through the pAMPSA phases. When an electric field was applied across the two pAMPSA plugs, cations in the microchannel near the region between the pAMPSA plugs

were extracted to the reservoirs in which the electrodes were immersed. Obviously, anions are rejected from the negatively charged polyelectrolytic gel plugs (pAMPSA) by electrostatic repulsion. If cations are extracted faster than supplied by mass transport in the microchannel, the local ionic charge balance breaks in the region between the pAMPSA plugs. As a consequence, an ion depletion region would appear and possibly expand as a function of the applied voltage and time [45]. Combined with electroosmotic flow (EOF), ion depletion could produce a spot at which ions were preconcentrated.

In this chapter, we propose a new way to enable even more sensitive detection of small molecules by combining the effective sample preconcentration on a microfluidic chip with bead-based competitive immunoassay. Biotin (cis-hexahydro-2-oxo-1-H-thieno-3,4-imidazolin-4-valeric acid; vitamin H) was selected in this study as a model of small targets because of its physiological importance as a water-soluble vitamin for cellular function and growth, thereby maintaining human health, vitality, and well-being. Fluorescent indicators (biotin-4-fluorescein) conjugated on magnetic microbeads were to be displaced by the unlabeled analytes. Subsequent electrokinetic

preconcentration of the displaced indicators in the microfluidic chip markedly intensifies the signals from the preconcentrated indicators, leading to a novel strategy for sensitive immunoassay of unlabeled small analytes.

3.2. Experimental

3.2.1. Reagents

All reagents were used as received without further purification. Monoclonal mouse anti-biotin antibody, D-biotin, and biotin-4-fluorescein were purchased from Invitrogen (Carlsbad, CA, USA). Carboxyl-terminated magnetic microbeads (BioMag[®] Maxi) were received from Bangs Laboratories, Inc. (Fishers, IN, USA). Tris(hydroxymethyl)aminomethane was obtained from Acros (Geel, Belgium). 2-acrylamido-2-methyl-1-propanesulfonic acid (AMPSA), 2-hydroxy-4'-(2-hydroxyethoxy)-2-methylpropiophenone (photoinitiator), N,N'-methylenebisacrylamide (cross-linker), 3-(trimethoxysilyl)propylmethacrylate (TMSMA), N-(3-dimethylaminopropyl)-N'-ethylcarbodiimide hydrochloride (EDC), bovine serum albumin (BSA), 2-iminobiotin, desthiobiotin, and sodium azide were purchased from Aldrich (St. Louis, MO, USA). Hexamethyldisilazane (HMDS) was received from J.T. Baker (Phillipsburg, NJ, USA). Sodium chloride, potassium chloride, sodium hydroxide, potassium phosphate dibasic, hydrochloric acid, and

ethylenediaminetetraacetic acid (EDTA) were purchased from Daejung (Siheung, Korea). 18 M Ω cm deionized (DI) water was used to prepare all aqueous solutions (Barnstead NANOpure[®], Thermo Scientific Inc., USA).

3.2.2. Preparation of antibody-conjugated magnetic microbeads

The conjugation of carboxyl-terminated magnetic microbeads with anti-biotin antibody was performed according to the instructions provided by the vendor (Bangs Laboratories, Inc.). Briefly, the magnetic beads (250 μ L, 20 mg/mL) were washed twice in coupling buffer (10 mM K₂HPO₄, 0.15 M NaCl, pH 5.5) and magnetically separated. After addition of 100 μ L EDC (40 mg/70 mL H₂O) solution, they were stirred for 15 min at room temperature. 250 μ L of anti-biotin antibody (1.0 mg/mL) was added to the solution and stirred non-magnetically for 3 h at 37°C. After conjugation, the mixture was magnetically separated to remove unbound antibodies. The antibody-conjugated magnetic microbeads were rinsed with washing buffer (10 mM Tris-HCl, 0.15 M NaCl, 0.1% w/v BSA, 0.1% NaN₃, 1 mM EDTA, pH 7.4), magnetically separated,

redispersed in Tris buffer (10 mM Tris-HCl, pH 8.3), and finally stored in a refrigerator until used.

3.2.3. Competitive immunoassay

Different concentrations of biotin were used as target small molecule in this study. The target molecules (biotin) were diluted in Tris buffer (10 mM Tris-HCl, pH 8.3). A 250 μ L volume of the antibody-conjugated magnetic microbeads was mixed with 250 μ L of 10 μ M fluorescent indicators (biotin-4-fluorescein) solution in a 1.5 mL Eppendorf tube, and resulting mixture was incubated for 1 h at 37°C. After conjugation, the mixture was magnetically separated to remove unbound fluorescent indicators and resuspended in 250 μ L of Tris buffer. And then, 250 μ L of biotin solution was added to the suspension and incubated for 1 h at 37°C for competitive immunoreaction. Subsequently, the solution of displaced indicators was retrieved by separating the magnetic microbeads under magnetic field and injected into a microfluidic chip for electrokinetic preconcentration.

3.2.4. Fabrication of microfluidic chips

Microfluidic chips with 60 μm wide and 30 μm deep microchannels were fabricated by standard photolithography as we reported previously [47]. In brief, Corning 2947 precleaned slide glasses (75 mm \times 25 mm, 1 mm thick, Corning, USA) were used as substrates. A slide glass was cleaned in a piranha solution ($\text{H}_2\text{SO}_4\text{:H}_2\text{O}_2 = 3\text{:}1$, J. T. Baker, USA) for 45 min and then washed with DI water several times. WARNING: Piranha solution reacts violently with organic solvents, and should be handled with extreme care. After removing the moisture on the surface with an air blower, the cleaned slide glass was dehydrated on a hot plate at 150°C for 3 min and then cooled to room temperature. The slide was then spincoated (YS-100MD, Won Corp., Korea) with HMDS at 6000 rpm for 30 s. It was then coated with a photoresist (PR; AZ4620, Clariant, USA) at 6000 rpm for 30 s. After soft baking the PR on a hot plate at 100°C for 90 s, the slide glass was cooled to room temperature and aligned under a pattern mask. The PR on the slide was exposed to UV light (365 nm) with an intensity of 15 mW/cm² for 10 s (MDE-4000, Midas, Korea) at AZ400K developer (Clariant, USA) for 100 s. The slide glass was then washed with DI water, and the PR was hard-baked on a hot plate at

150 °C for 15 min. Adhesion tape was attached to reverse side of the slide glass in order to protect it from the etching solution. The slide glass was etched with a 6:1 buffered oxide etch solution (J.T. Baker, USA) for 35 min at 25°C with stirring. The etched slide glass was washed with DI water. After taking off the adhesion tape, the slide glass was sonicated (3510E–DTH, Branson, USA) for 10 min to get rid of the glass particles. The etched glass was then drilled at the positions for the reservoirs with a 2 mm–diameter diamond drill at 18,000 rpm and cleaned in a piranha solution for 30 min to remove the remaining PR. It was then covered with another flat slide glass, which was also cleaned in a piranha solution for the same duration. The pair of slide glasses was permanently attached to each other by thermal bonding. DI water between the glasses prevented the formation of air bubbles during the bonding process. The glasses were heated at 600°C in a furnace (CRF–M15, Ceber, Korea) for 6 h at which time they were slowly cooled in the furnace to room temperature over 10 h.

3.2.5. Polyelectrolytic gel plugs (pAMPSA) fabrication process

Polyelectrolytic gel plugs were fabricated by UV photopolymerization. The highly charge-selective polymer (pAMPSA) used in this study is a kind of polyelectrolytic polymer gels which have ion permeable nanoporous network. Monomer, photoinitiator, cross-linker concentration, UV intensity, and exposure time are important factors to control the polymer pore size that determines the efficiency and selectivity of ion extraction. 2 M aqueous AMPSA was the monomer that was used to create the negatively charged polyelectrolytic gel plug. It was prepared with a photoinitiator (2%) and a cross-linker (2%). Before polymerization, the microchannel was coated with 0.5% TMSMA to covalently link the polyelectrolytic gel plugs to the glass surface at room temperature for 30 min. The TMSMA-coated microchannel was cleaned with deionized water and methanol, and was filled with the monomer solution. The microchannel was aligned under a patterned mask film to determine the desired location of the polymers and exposed to UV light at 15 mW/cm^2 for 2 s. The pAMPSA plugs in the microchannel were washed and stored in 10 mM KCl solution.

3.2.6. Instrumentation

Electrokinetic preconcentration was monitored by an inverted epifluorescence microscope (Eclipse TE 2000–U, Nikon, Japan) equipped with a 100 W mercury lamp and a CCD camera (CV–S3200, JAI Corporation, Japan). Movies and images were captured by Pinnacle Studio 9 software (Pinnacle Systems Inc., USA). Electric voltages by two DC power suppliers (XDL 35–5P, Xantrex Inc., England) were applied to platinum electrodes immersed into reservoirs of the microfluidic chip.

3.3. Results and Discussion

3.3.1. The mechanism of electrokinetic concentration polarization

The schematic view of the experimental procedure is shown in Fig. 3-1. First, magnetic microbeads, which were conjugated with fluorescent indicators (biotin-4-fluoresceins; MW 644.71) bound on immobilized antibodies, were dispersed in Tris buffer solution (10 mM Tris-HCl, pH 8.3) and mixed with unlabeled target small molecules (biotin; MW 244.31). This resulted in target-induced displacement of the fluorescent indicators that were retrieved by separating the magnetic microbeads under magnetic field. Second, the solution of displaced indicators was injected into a microfluidic chip for electrokinetic preconcentration near the ion depletion region between the negatively charged polyelectrolytic gel (pAMPSA) plugs that had been photopolymerized.

In principle, the preconcentration process in this system can be elucidated on the basis of concentration polarization that results from selective ion extraction. Under an electric field, cations only are rapidly extracted through the pAMPSA plugs and anions are expelled to fulfill the condition of thermodynamic

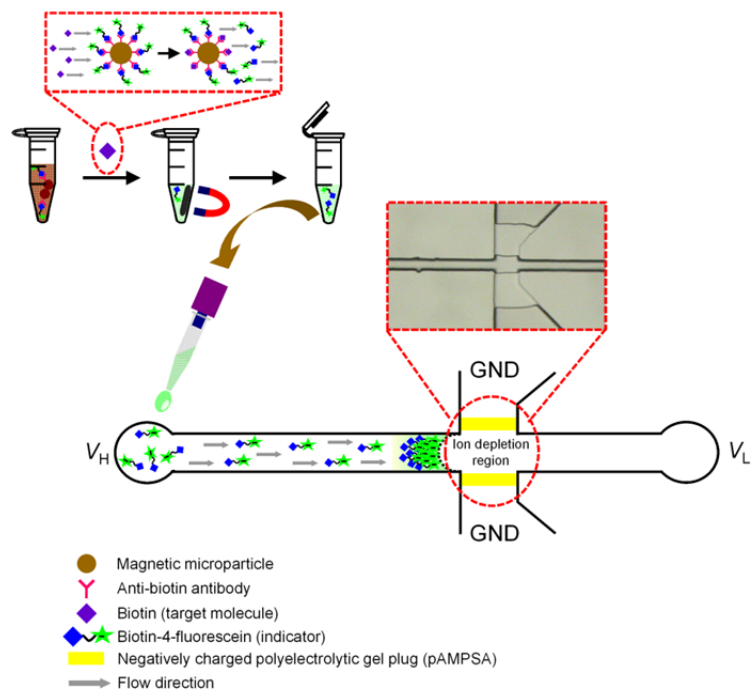


Fig. 3-1 Schematic illustration of small molecule detection by combining the effective sample preconcentration on a microfluidic chip with bead-based competitive immunoassay. The enlarged view is an optical micrograph showing a microchannel section incorporating the polyelectrolytic gel plugs.

charge balance as shown in Fig. 3-2. Against the electroosmotic flow (EOF), the anions, which used to be present between the pair of pAMPSA plugs, feel the electrophoretic force to upstream in the microchannel. Thus, electrophoretic force as well as thermodynamic repulsion due to charge balance make ion depletion region appears between the pair of pAMPSA plugs (Fig. 3-2C). As the anions are driven to upstream and meet the cations coming from the inlet of the microchannel by EOF, ions are highly concentrated in vicinity to the ion depletion region. As a consequence, the negatively charged indicators, which have been injected in the inlet and delivered in the EOF flow, are stopped from passing through the ion depletion region and stacked in front of the ion depletion boundary (Fig. 3-1). On the other hand, if it is necessary for cations to be concentrated, the negatively charged polyelectrolytic gel (pAMPSA) should be replaced with positively charged polyelectrolytic gel plugs and the polarity should be switched as well. Under this condition, an electric field could selectively extract the anions in the main microchannel through the positively charged polyelectrolytic gel plugs, leading to local ion depletion. As a consequence, cations

would be stacked in front of the ion depletion boundary in the same way.

3.3.2. Electrokinetic preconcentration of fluorescent indicators

Fig. 3-2 illustrates the mechanism involved in the sample preconcentration process based on electrokinetic trapping on a pAMPSA-based microfluidic chip. When applying voltages at V_H , V_L , and GND of 8 V, 3 V, and float, respectively, the fluorescent indicators in Tris buffer solution were driven by EOF to move along the microchannel (Fig. 3-2A). When the GND (chassis ground) electrodes on the chip were set to the ground potential, cations instantly passed through the negatively charged polyelectrolytic gel plug, pAMPSA, and anions expelled from the near pAMPSA plugs to maintain charge neutrality (Fig. 3-2B). As a result, an ion depletion region develops between the pAMPSA pair (Fig. 3-2C) and then fluorescent indicators were stacked near the ion-depleted region (Fig. 3-2D).

To confirm sample preconcentration by electrokinetic trapping, the behavior of anionic fluorescent indicators (biotin-

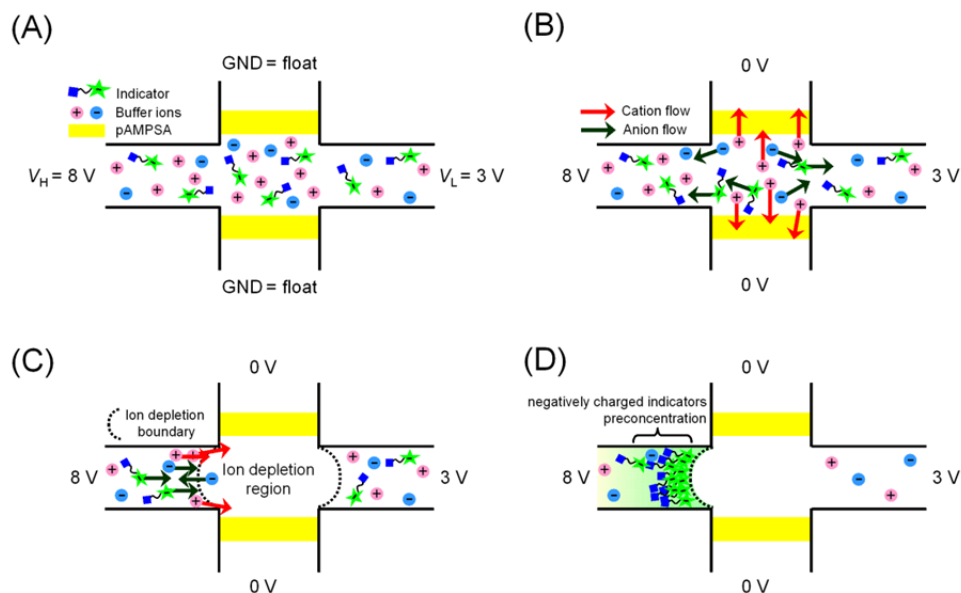


Fig. 3–2 Sample preconcentration process based on electrokinetic trapping. (A) Voltages at V_H , V_L , and GND of 8 V, 3 V, and float, respectively. The solution of displaced indicators flows along the sample and analysis channel. (B) GND is 0 V. Only cations are extracted through the negatively charged polyelectrolytic gel plugs, pAMPSA, while anions are expelled from the interface between the pair of pAMPSA plugs and solution. (C and D) Then, the ion depletion region expands along the main microchannel. Negatively charged indicators are stacked to the left of the ion depletion boundary due to the concentration polarization. Red and green arrows indicate cation and anion movement near the pAMPSA, respectively.

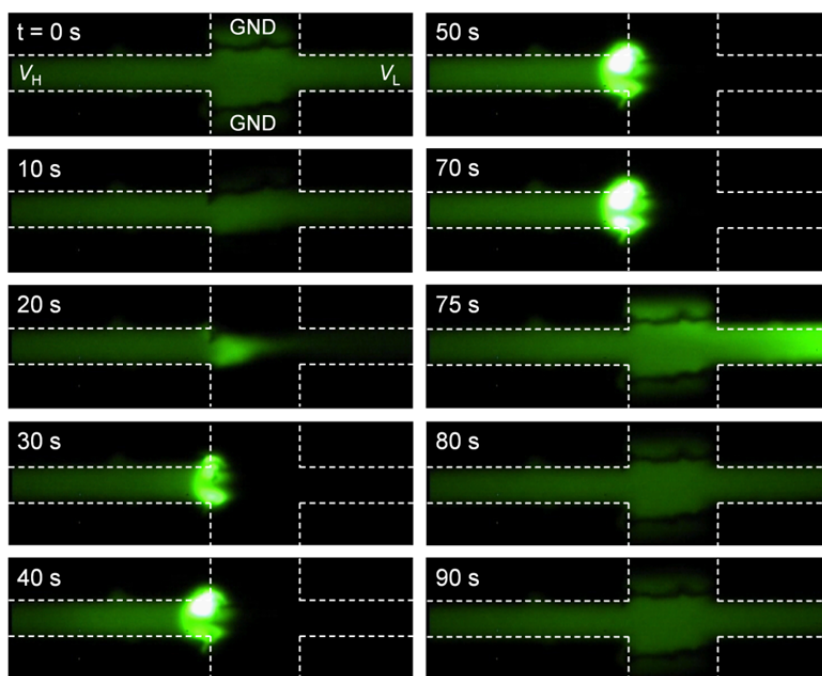


Fig. 3-3 Examples of sample preconcentration. The microchannel was filled with 5 μM biotin-4-fluorescein in Tris buffer (10 mM Tris-HCl, pH 8.3). When V_H , V_L , and GND were 8 V, 5 V, and 0 V, respectively, biotin-4-fluorescein was rapidly preconcentrated in the microchannel (0~70 s). The preconcentrated biotin-4-fluoresceins were redispersed into the sample solution by setting the GND electrode float (70~90 s).

4-fluorescein) was monitored using a fluorescence microscope. Fig. 3-3 shows that 5 μ M fluorescent indicator molecules in 10 mM Tris-HCl at pH 8.3 was preconcentrated in the microchannel. Under an applied electric field, the fluorescent indicators started to be concentrated at the left side of the ion depletion region between the negatively charged polyelectrolytic gel plug. When the GND electrodes were floated, the fluorescent indicators began to redisperse in the sample solution and flow along the microchannel.

3.3.3. Displacement and subsequent preconcentration

Fig. 3-4 shows optical and fluorescence micrographs of the magnetic microbeads on which the anti-biotin antibodies conjugated with the fluorescent indicators were immobilized. In the presence of unlabeled biotin targets, we observed a significant decrease in fluorescence on the indicator-conjugated magnetic microbeads. This tells that the non-fluorescent biotin targets kicked out the fluorescent indicators and bound with the antibodies (Fig. 3-5). In contrast, when we added fluorescent indicators in the solution of magnetic microbeads conjugated with unlabeled biotin targets, no

significant fluorescence was observed on the magnetic beads. It indicates that indicator-induced displacement of the nonfluorescent biotin targets were negligible (Fig. 3-6). These results ensured that the native biotin targets had sufficiently higher binding affinity to the anti-biotin antibody than the biotin-4-fluorescein indicators.

Fig. 3-7 is a series of fluorescence micrographs obtained during the electrokinetic trapping preconcentration of indicators, which were released from the microbeads by 100 nM biotin targets in the sample. By applying voltages at V_H , V_L , and GND of 8 V, 3 V, and 0 V, respectively, the fluorescent indicators started to be concentrated at the left side of the ion depletion region. As the time elapsed, the electrokinetic trapping of the fluorescent indicators proportionally intensified the fluorescence from the preconcentrated spot as shown in Fig. 3-7.

3.3.4. Sensitivity

To see if this method can provide quantitative information, we recorded the fluorescence intensities of collected indicators that had been generated from competitive immunoreactions at a

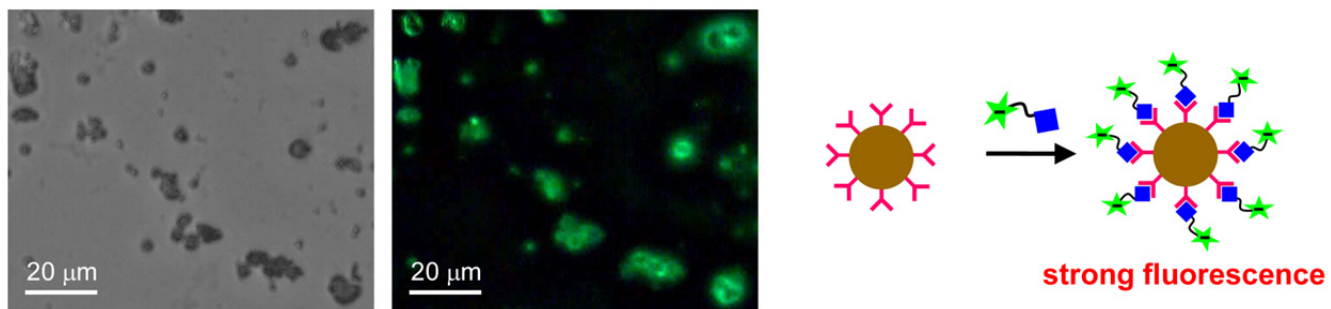


Fig. 3-4 Optical (left) and fluorescence (right) micrographs of magnetic microbeads bearing the fluorescent indicators (biotin-4-fluorescein).

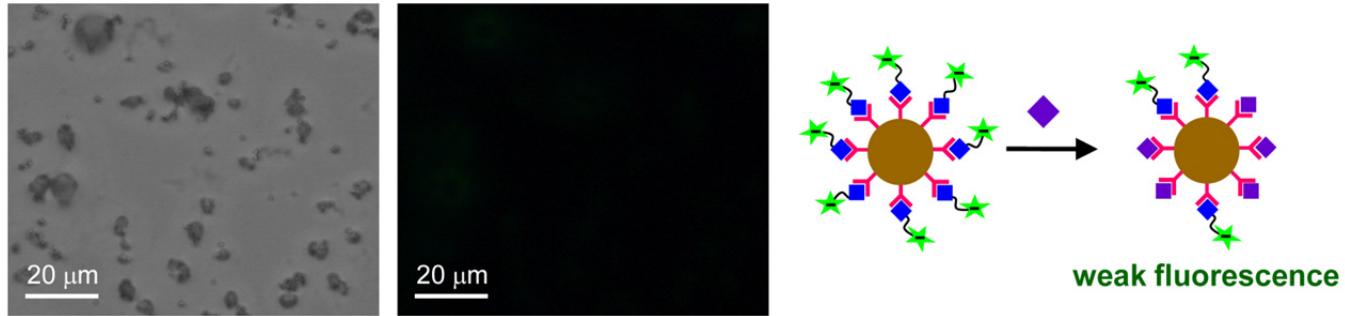


Fig. 3–5 Optical (left) and fluorescence (right) micrographs obtained from the magnetic microbeads after competitive immunoreaction with unlabeled biotin targets and subsequent washing. The fluorescent indicators (biotin–4–fluoresceins) previously conjugated with the antibodies were washed out.

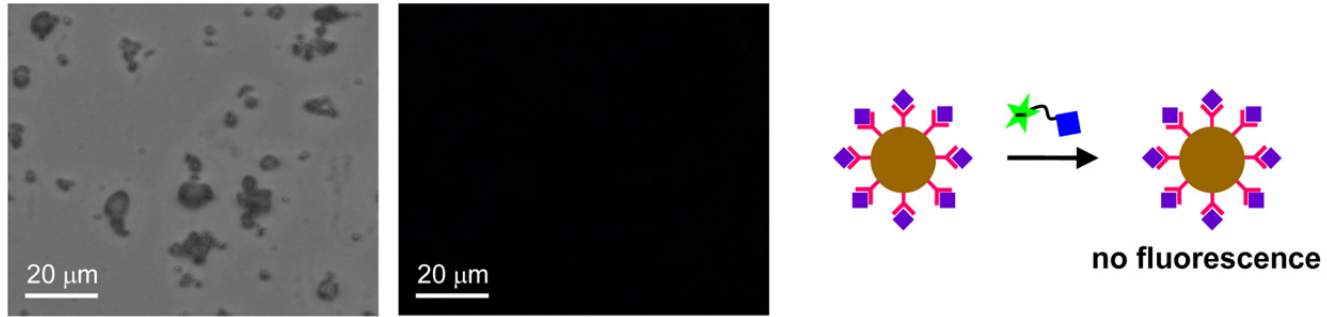


Fig. 3-6 Optical (left) and fluorescence (right) micrographs obtained from the magnetic microbeads conjugated with the unlabeled biotin target after be exposed to the fluorescent indicators in the solution.

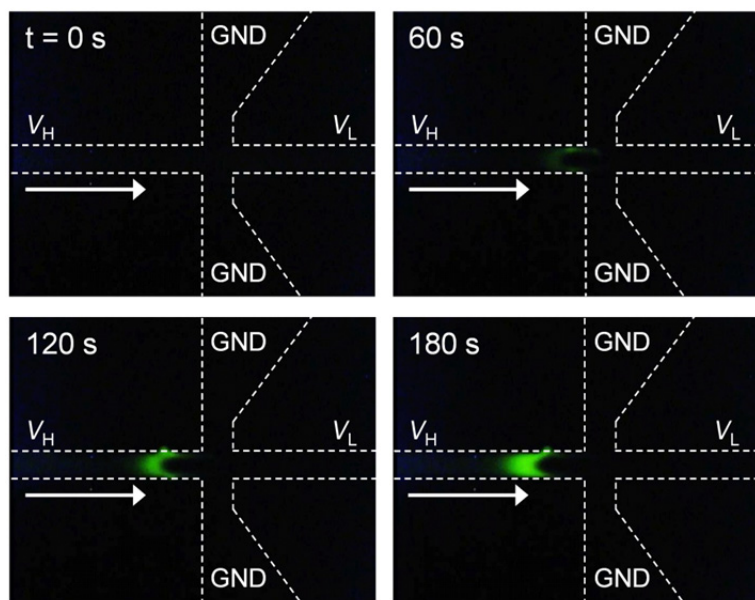


Fig. 3–7 A series of fluorescence micrographs obtained during the electrokinetic preconcentration of the fluorescent indicators displaced by 100 nM biotin. $V_H = 8$ V, $V_L = 3$ V, and GND = 0 V.

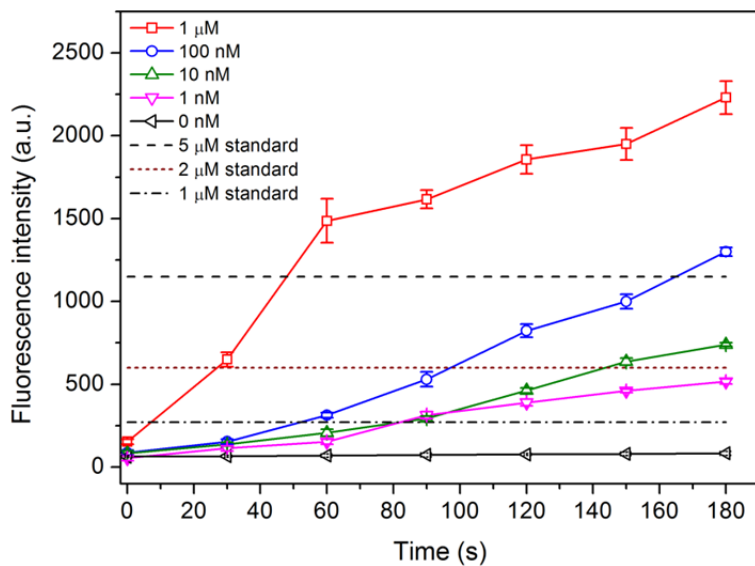


Fig. 3–8 Fluorescence intensity profiles of the concentrated indicators displaced by 1 μM , 100 nM, 10 nM, and 1 nM biotin during electrokinetic preconcentration. The horizontal dotted lines are the fluorescence intensities of 1, 2, and 5 μM standard indicator solutions for comparison.

series of concentrations of the analyte (1 μM , 100 nM, 10 nM, and 1 nM). The entire concentration experiment was carried out in about 3 min. The fluorescence intensities of preconcentrated indicators were calibrated using the standard fluorescein solutions (Fig. 3–8). As shown in Fig. 3–8, the fluorescence intensities linearly increased during the preconcentration process. The fluorescence from a 1 nM biotin solution reached the intensity as strong as 2 μM standard fluorescein solution within 3 min, which corresponds to ~ 2000 -fold amplification in intensity. It appears that the fluorescence intensity could reach its maximum and the fluorescent indicators concentration caused no more increase for the 1 μM analyte. The fluorescence intensity for 1 nM was sufficiently higher than that for zero concentration. The limit of detection is estimated to be *ca.* 1 nM.

3.3.5. Specificity

In order to evaluate the specificity of this immunoassay system, we carried out the same experiment with biotin analogs such as biocytin, 2-iminobiotin, desthiobiotin instead of the biotin target to that shown in Fig. 3–9. Fluorescence intensity

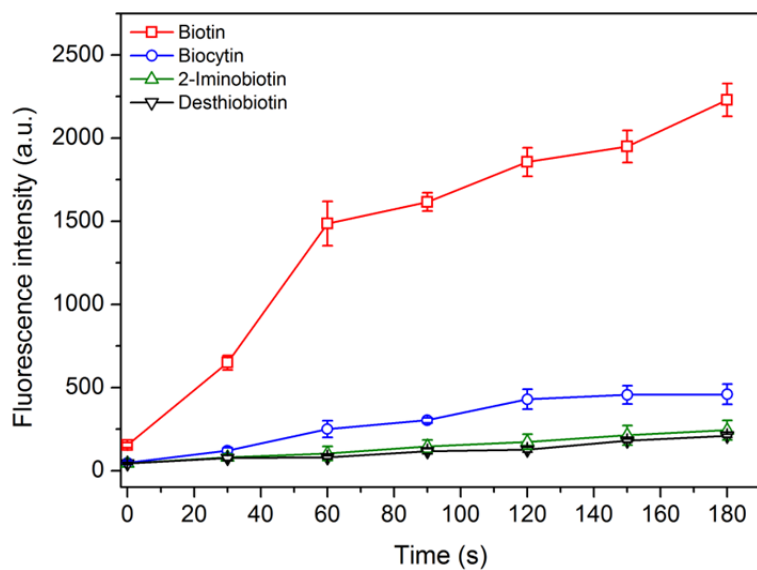


Fig. 3–9 Specificity of the proposed immunoassay over a few target analogs ($1 \mu\text{M}$ for all) which were biocytin, 2-iminobiotin, and desthiobiotin. The profile obtained from $1 \mu\text{M}$ native biotin was plotted again for comparison.

was monitored during the electrokinetic trapping of indicator molecules displaced by 1 μM biotin and compared with that obtained from the other analogs at same concentrations. Among the target molecule and its various analogs tested, native biotin target showed exceptionally high changes in fluorescence intensity compared to the other analogs. This result shows that a negligible amount of the fluorescen indicators were displaced by the biotin analogs. Therefore, the specificity of the anti-biotin antibody on the microbeads was high enough to guarantee this method as a reliable immunoassay for small molecule analysis.

3.4. Conclusion

The electrokinetic preconcentration on a pAMPSA-based microfluidic chip was combined with competitive immunoassay to enhance the sensitivity of small molecule immunoanalysis. The preconcentration was based on the phenomenon of concentration polarization near the pAMPSA plug. A negatively charged polyelectrolytic gel (pAMPSA) plug was employed to effectively extract cations and induce ion depletion for electrokinetic accumulation of charged fluorescent indicators. The anionic fluorescent indicators stacked in the trapping zone tremendously boosted up the local fluorescence intensity. Sensitive and selective analysis of small molecule targets was successfully accomplished based on the proposed scheme. And the mechanisms involved in the displacement reaction and preconcentration were well understood and proved by the relevant experiments. Although this work is a proof-of-concept, what it indicates is significant. The proposed and demonstrated method is expected to be generally applied to competitive immunoassay, particularly powerful for practical immunoassay of small molecular targets. Harnessing a variety of microfluidic chip technologies, it has great potential to evolve

toward portable and integrated immunoassay devices for highthroughput screening of small molecules.

3.5. References

- [1] X. H. Wang, S. Wang, *Sensors* **2008**, *8*, 6045.
- [2] J. Mitchell, *Sensors* **2010**, *10*, 7323.
- [3] H. Gohlke, G. Klebe, *Angew. Chem., Int. Ed.* **2002**, *41*, 2644.
- [4] R. Tian, S. Xu, X. Lei, W. Jin, M. Ye, H. Zou, *Trends Anal. Chem.* **2005**, *24*, 810.
- [5] N. Mano, K. Sato, J. Goto, *Anal. Chem.* **2006**, *78*, 4668.
- [6] S. Strano–Rossi, F. Molaioni, F. Rossi, F. Botrè, *Rapid Commun. Mass Spectrom.* **2005**, *19*, 1529.
- [7] M. A. Martinez–Gomez, S. Sagrado, R. M. Villanueva–Camanas, M. J. Medina–Hernandez, *Electrophoresis* **2006**, *27*, 3410.
- [8] D. Lössner, H. Kessler, G. Thumshirn, C. Dahmen, B. Wiltschi, M. Tanaka, W. Knoll, E. K. Sinner, U. Reuning, *Anal. Chem.* **2006**, *78*, 4524.
- [9] J. Feeney, *Angew. Chem., Int. Ed.* **2000**, *39*, 290.
- [10] D. Wild, *The Immunoassay Handbook*, Elsevier Ltd., New York, **2005**.
- [11] N. Kobayashi, K. Iwakami, S. Kotoshiba, T. Niwa, Y. Kato, N. Mano, J. Goto, *Anal. Chem.* **2006**, *78*, 2244.
- [12] J. W. Kehoe, B. K. Kay, *Chem. Rev.* **2005**, *105*, 4056.

- [13] E. T. Boder, K. S. Midelfort, K. D. Wittrup, *Proc. Natl. Acad. Sci. U.S.A.* **2000**, *97*, 10701.
- [14] M. Y. Cha, H. Y. Lee, Y. Ko, H. Shim, S. B. Park, *Bioconjugate. Chem.* **2011**, *22*, 88.
- [15] W. N. Vreeland, S. J. Williams, A. E. Barron, A. P. Sassi, *Anal. Chem.* **2003**, *75*, 3059.
- [16] P. Gebauer, P. Boček, *Electrophoresis* **2002**, *23*, 3858.
- [17] A. Wainright, S. J. Williams, G. Ciambone, Q. Xue, J. Wei, D. Harris, *J. Chromatogr. A* **2002**, *979*, 69.
- [18] H. Cui, K. Horiuchi, P. Dutta, C. F. Ivory, *Anal. Chem.* **2005**, *77*, 1303.
- [19] D. Kohlheyer, J. C. T. Eijkel, S. Schlautmann, A. van den Berg, R. B. M. Schasfoort, *Anal. Chem.* **2007**, *79*, 8190.
- [20] W. Tan, Z. H. Fan, C. X. Qiu, A. J. Ricco, I. Gibbons, *Electrophoresis* **2002**, *23*, 3638.
- [21] J. Wen, Y. Lin, F. Xiang, D. W. Matson, H. R. Udseth, R. D. Smith, *Electrophoresis* **2000**, *21*, 191.
- [22] Y. Mourzina, D. Kalyagin, A. Steffen, A. Offenhäusser, *Talanta* **2006**, *70*, 489.
- [23] B. Jung, R. Bharadwaj, J. G. Santiago, *Electrophoresis* **2003**, *24*, 3476.

- [24] J. Lichtenberg, E. Verpoorte, N. F. de Rooij, *Electrophoresis* **2001**, *22*, 258.
- [25] W. Yang, X. Sun, T. Pan, A. T. Woolley, *Electrophoresis* **2008**, *29*, 3429.
- [26] C. Yu, M. H. Davey, F. Svec, J. M. J. Fréchet, *Anal. Chem.* **2001**, *73*, 5088.
- [27] B. S. Broyles, S. C. Jacobson, J. M. Ramsey, *Anal. Chem.* **2003**, *75*, 2761.
- [28] R. Dhopeswarkar, L. Sun, R. M. Crooks, *Lab Chip* **2005**, *5*, 1148.
- [29] A. V. Hatch, A. E. Herr, D. J. Throckmorton, J. S. Brennan, A. K. Singh, *Anal. Chem.* **2006**, *78*, 4976.
- [30] K. W. Hoeman, J. J. Lange, G. T. Roman, D. A. Higgins, C. T. Culbertson, *Electrophoresis* **2009**, *30*, 3160.
- [31] S. M. Kim, M. A. Burns, E. F. Hasselbrink, *Anal. Chem.* **2006**, *78*, 4779.
- [32] Y. Wang, K. Pant, Z. Chen, G. Wang, W. F. Diffey, P. Ashley, S. Sundaram, *Microfluid. Nanofluid.* **2009**, *7*, 683.
- [33] H. Yu, Y. Lu, Y. Zhou, F. Wang, F. He, X. Xia, *Lab Chip* **2008**, *8*, 1496.
- [34] S. J. Kim, Y. A. Song, J. Han, *Chem. Soc. Rev.* **2010**, *39*,

912.

[35] J. Astorga–Wells, H. Swerdlow, *Anal. Chem.* **2003**, *75*, 5207.

[36] S. Song, A. K. Singh, B. J. Kirby, *Anal. Chem.* **2004**, *76*, 4589.

[37] M. Shen, H. Yang, V. Sivagnanam, M. A. M. Gijs, *Anal. Chem.* **2010**, *82*, 9989.

[38] D. Ross, L. E. Locascio, *Anal. Chem.* **2002**, *74*, 2556.

[39] Y.–C. Wang, A. L. Stevens, J. Han, *Anal. Chem.* **2005**, *77*, 4293.

[40] D. Hlushkou, R. Dhopeswarkar, R. M. Crooks, U. Tallarek, *Lab Chip* **2008**, *8*, 1153.

[41] H. Chun, T. D. Chung, H. C. Kim, *Anal. Chem.* **2005**, *77*, 2490.

[42] J.–H. Han, K. B. Kim, H. C. Kim, T. D. Chung, *Angew. Chem., Int. Ed.* **2009**, *48*, 3830.

[43] K. B. Kim, H. Chun, H. C. Kim, T. D. Chung, *Electrophoresis* **2009**, *30*, 1464.

[44] H. Chun, H. C. Kim, T. D. Chung, *Lab Chip* **2008**, *8*, 764.

[45] H. Chun, T. D. Chung, J. M. Ramsey, *Anal. Chem.* **2010**, *82*, 6287.

[46] K. B. Kim, J.-H. Han, H. C. Kim, T. D. Chung, *Small* **2012**, *8*, 378.

[47] K. B. Kim, J.-H. Han, H. C. Kim, T. D. Chung, *Appl. Phys. Lett.* **2010**, *96*, 143506.

4. Electrochemical Signal Amplification for Immunosensor based on 3D Interdigitated Array Electrodes

4.1. Introduction

Signal amplification is undoubtedly crucial for the sake of sensitive immunosensors with low detection limits [1–3]. One of the ways to amplify signal for sensitive biosensing is to generate as many signaling molecules per biospecifically-bound target as possible by employing appropriate labels. There have been reported different types of labels, e.g. metal nanoparticles [4,5], magnetic particles [6,7], quantum dots [8], silica nanoparticles [9,10] and so on. Amongst those, enzymes are still most widely used as labels [11–13] because of the high turnover frequencies and reaction selectivities [14,15]. Alkaline phosphatase (ALP) is commonly employed as an enzyme label in immunoassays and p-aminophenyl phosphate (APP) is adopted as an enzyme substrate in such sensors [16]. It allows a steady reaction rate for a prolonged time and shows long-term stability even in nonsterile environments. For these reasons, a number ALP-based electrochemical immunosensors

have been developed [17–19]. To accomplish higher signal amplification for electrochemical immunosensors, the enzymatic amplification is usually combined with additional amplification step such as redox cycling of enzymatically produced electroactive species. That is to say, it is to not only increase the number of the electroactive species but also regenerate them for cycling the faradaic reactions. In redox cycling, electrochemically oxidized (or reduced) species are reduced (or oxidized) enzymatically [20,21], chemically [22–24], or electrochemically [25,26]. Regenerated electroactive species participate in elevating faradaic current by being re-oxidized (or re-reduced). It is obvious that more cycling of a given electroactive molecule created by the enzyme leads to larger current from the electrochemical immunosensor. In this regard, additional enzymes [27–31] or chemical reagents [32–36] were used to achieve extra signal amplification through redox cycling process and turned out to be significantly successful.

Multi-enzymatic system for redox cycling [37–40] is a conventional approach for sensitive biological assays. However, co-immobilization of the multiple enzymes on the electrode surface tends to bring about complicate issues that require

considerable effort to find the conditions for fabricating, operating, and storage. For example, since the redox cycling efficiency of multi-enzymatic systems is a sensitive function of the enzyme kinetics and the amount of dissolved or immobilized enzymes, it needs sophisticated design of corresponding enzyme-modified electrodes to ensure stable and reproducible enzyme activities for the expected redox cycling efficiency. Chemical regeneration is a strong option to take for this purpose [32–36]. In this method, the electroactive species coming from an enzyme label is homogenously oxidized (or reduced) by a chemical reagent in the solution, instead of enzyme, to be ready to get reduced (or oxidized) again. Compared with multi-enzyme systems, this allows simple but sensitive electrochemical detection by just adding chemical reagents. However, strong reducing (or oxidizing) agents themselves for rapid chemical reaction may be electrochemically oxidized (or reduced), resulting in high background currents [32,33]. That is why the electron transfer of such reducing (or oxidizing) agents should be as slow at electrodes as possible while the homogeneous redox reaction must be fast. This requirement could limit the range of

applicable electrode materials. Still, there are a few issues in chemical amplification to tackle toward point-of-care diagnostics.

Electrochemical redox cycling of enzyme-generated electroactive species is another doable approach for signal amplification [41]. It needs generator-collector electrodes system that gives enlarged current difference directly leading to enhanced signal [42-44]. The generator electrode oxidize or reduce the analytes of interest, which are then transported, mostly by diffusion, to the collector electrode to be reduced or oxidized. There have been reported a few electrode systems, *e.g.* interdigitated array (IDA) electrodes [45-49], twin-electrode thin-layer cell (TETLC) [50-52], rotating ring-disc electrodes (RRDE) [53,54], and a micromachined wall-jet ring-disc electrode (WJRDE) [55]. The IDA electrodes have received particular interests in that as many band pairs as we want and a narrow spacing between the two neighbored electrodes are allowed so as to make diffusion layers overlapped around the generator and collector electrodes. As one electrode gets closer to the other, the redox species formed at the generator electrode reach the collector electrode

in shorter time by spontaneous transport, diffusion, to be regenerated. This triggers a feedback redox loop to effectively amplify the faradaic current. The electrochemical signal amplification for immunosensors, as such, attracts much attention because it needs neither additional enzyme nor chemicals. For signal amplification, it adds no variable originating from biological/chemical additives to given immunosensing system.

In this chapter, we proposed 3 dimensional electrochemical redox cycling as an alternative approach to achieve much simpler and more efficient amplification that is to be combined with enzymatic generation of electroactive species, *viz.*, signaling molecules. The devised 3D IDA has a straightforward design to realize redox cycling with minimal side effects such as chemical contamination, stability of the additives, and so forth. We fabricated it by simply bonding two IDA electrodes with a 5 μm width and 10 μm gap between the bottom and ceiling, which were apart from each other by several tens of micrometers, corresponding to the height of the microchannel. To evaluate the 3D IDA chip, voltammetric responses to electroactive species in the microchannel were investigated in

terms of its redox cycling efficiency, computed concentration profiles, and hysteresis. We confirmed the geometric configuration effect of electrodes from the comparison study with the four different systems, *i.e.* two straight electrodes in parallel, Open-2D IDA, Closed-2D IDA, 3D IDA. Encouraged by the best results from 3D IDA, we applied 3D IDA to electrochemical immunosensing. The prepared platform for 3D IDA-based immunosensors had an indium tin oxide (ITO) electrode modified with electrografted electroactive ferrocene (Fc) as an electron mediator, alkaline phosphatase (ALP) as an enzyme label, and *p*-aminophenyl phosphate (APP) as an enzyme substrate. Here we present the immunosensing performances of the 3D IDA for mouse IgG and cardiac troponin I (cTnI), a specific biomarker of myocardial damage, in human serum.

4.2. Experimental

4.2.1. Chemicals and materials

All reagents were used as received without further purification. Human cardiac troponin I (cTnI), cardiac troponin I free human serum, monoclonal mouse anti-cardiac troponin I (Mab: 19C7, 16A11) were purchased from HyTest (Turku, Finland). The alkaline phosphatase (ALP) labeling kit was received from Dojindo Molecular Technologies, Inc. (Rockville, MD, USA). The conjugation of ALP with monoclonal mouse anti-cardiac troponin I was performed according to the instructions provided by the vendor (Dojindo Molecular Technologies, Inc.). Mouse IgG, anti-mouse IgG, ALP-conjugated anti-mouse IgG, bovine serum albumin (BSA), N,N'-disuccinimidyl carbonate (DSC), N,N'-Diisopropylethylamine (DIPEA), toluene, sodium perchlorate, lithium perchlorate, magnesium chloride, and 1,1'-ferrocenedimethanol were purchased from Sigma-Aldrich (St. Louis, MO, USA). (Hydrazinocarbonyl)ferrocene was obtained from Tokyo Chemical Industry Co. (Tokyo, Japan). 4-aminophenyl phosphate (APP) monosodium salt hydrate was received from Gold Biotechnology, Inc. (St. Louis, MO, USA).

N-(6-aminohexyl)aminomethyltriethoxysilane (AHAMTES) was obtained from Gelest (Morrisville, PA, USA). Hexamethyldisilazane (HMDS), ethanol, and acetone were received from J. T. Baker (Phillipsburg, NJ, USA). Tris(hydroxymethyl)aminomethane (Tris) was obtained from Acros (Geel, Belgium). Sodium chloride, potassium chloride, acetonitrile, sodium hydroxide, and hydrochloric acid were purchased from Daejung (Siheung, Korea). Phosphate buffered saline (PBS, pH 7.4) solution consisted of 10 mM phosphate and 0.1 M NaCl. Tris buffer (pH 9.0) solution for enzymatic reaction contained 50 mM Tris and 10 mM MgCl₂, and the pH was adjusted by adding 1.0 M HCl dropwise. 18 M Ω ·cm deionized (DI) water was used to prepare all aqueous solutions (Barnstead NANOpure[®], Thermo Scientific Inc., USA).

4.2.2. Device fabrication

The IDA microelectrodes were fabricated by standard photolithography and etching processes. The fabrication scheme is illustrated in Fig. 4-1A~C. ITO-coated glass slides (75 mm \times 25 mm, 1.1 mm thick, Sigma-Aldrich, USA) were used as substrates. An ITO-coated glass slide was sequentially

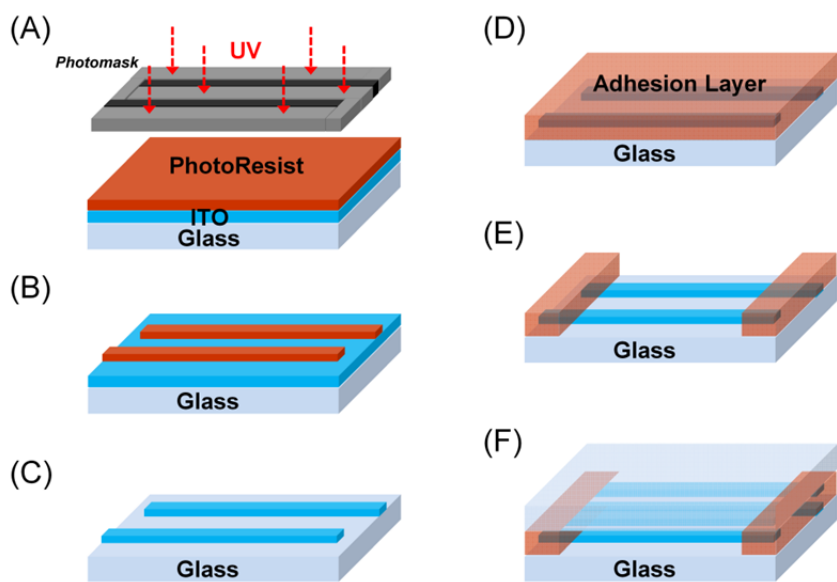


Fig. 4–1 Fabrication process of the 3D IDA device. (A) PR is coated on ITO substrate. Then, the PR film is exposed to UV light through a photomask. (B) The PR film is developed in a PR developer. (C) The exposed area of ITO is removed by etchant solution and the PR is removed. (D) An adhesion layer is deposited that ultimately determines the height of the channel. (E) The adhesion layer is removed to create fluidic channel. (F) Another IDA electrode is attached to construct the 3D IDA.

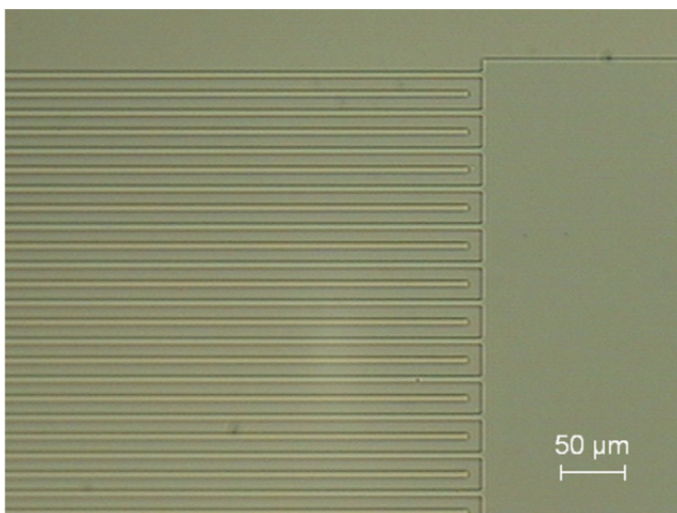


Fig. 4-2 An optical microscope image of part of ITO band pattern of IDA electrode. The 5 μm width, 10 μm gap, 2 mm long IDA electrode contains 25 bands on each side.

cleaned with ethanol, acetone, and DI water sequentially. After removing the moisture on the surface with an air blower, the cleaned ITO substrate was dehydrated on a hot plate at 120°C for 3 min and then cooled to room temperature. The substrate was spin-coated (YS-100MD, Won Corp., Korea) with HMDS at 7000 rpm for 30 s. The HMDS-coated substrate was placed on a hot plate at 120°C for 90 s and subsequently cooled at room temperature. Afterwards, the photoresist (PR; AZ4620, Clariant, USA) coated the surface of the substrate using a spin coater at 7000 rpm for 30 s. After soft baking the PR-coated substrate at 100°C for 90 s, the substrate was cooled at room temperature for 90 s immediately. Then, the substrate was aligned under a pattern-designed mask, and exposed to UV light (365 nm) for 11 s with a UV aligner (MDE-4000, Midas, Korea). The UV-exposed substrate was immersed into the AZ400K developer (Clariant, USA) for developing UV-exposed PR. The substrate was then washed with DI water and dried in clean air. Next, the substrate was hard-baked on a hot plate at 120°C for 15 min. After cooling at room temperature, the PR-patterned ITO substrate was etched with an etchant solution (TE-100, Transene Company, Inc., USA) at 60°C for 13 min,

which resulted in formation of IDA ITO microelectrodes. All photoresist residues were removed by rinsing the ITO microelectrodes with acetone using an ultrasonic cleaner (3510E-DTH, Branson, USA) for 2 min. The IDA microelectrode consisted of 25 pairs of microbands. The band length of the IDA was 2 mm and the width was 5 μm , and the gap was 10 μm . An optical microscope image of the IDA microelectrode is shown in Fig. 4-2.

The three-dimensional (3D) IDA device was fabricated by attaching two IDAs. In Brief, one IDA to be the ceiling was drilled at the positions for the reservoirs with a 2 mm-diameter diamond drill at 18,000 rpm. Then, two IDAs to be the ceiling and bottom were ultrasonically cleaned with ethanol, acetone, and DI water subsequently and dried under a stream of N_2 . A double-sided adhesive film (SK30C, Greentack Korea Co., Korea) was attached to the bottom IDA in order to assemble the ceiling IDA (Fig. 4-1D). After removing the adhesive film of the cavity for fluidic channel part (Fig. 4-1E), the two IDAs were conglutinated face to face by the double-sided adhesive layer (thickness: *ca.* 30 μm) and formed a 3D IDA device. The 3D IDA electrodes were aligned perpendicular to the channel,

as shown in Fig. 4-1F. Thus, the band length of the IDA is equal to the channel width. The channel height of 3D IDA is also the same as the thickness of the adhesion layer. Closed-2D IDA device consisted of a bottom IDA and a flat slide glass instead of the ceiling IDA.

4.2.3. Modeling and calculations

The calculations were performed using finite element simulation software (COMSOL Multiphysics, Stockholm, Sweden). The electrochemical system treated here is a simple outer-sphere heterogeneous electron transfer reaction at the electrodes, $O + ne^- \rightleftharpoons R$, where n is the number of electrons transferred. Two-dimensional structures of various type devices are simplified in rectangular unit cells. For the case of high overpotential applied to the electrodes, constant-concentration boundary conditions were applied based on the assumption of complete oxidation or complete reduction on the electrode surfaces. The steady state of the various type electrodes was characterized by assuming that the diffusion coefficients of the reduced and oxidized forms are the same [56], which leads to the result that the sum of oxidized (C_O)

and reduced (C_R) forms is constant over the diffusion space and is equal to the sum of the bulk concentration (C_{Bulk}) [57].

4.2.4. Electrode modification and procedures for measurements

A schematic of the preparation of an immunosensing layer is shown in Fig. 4–18. The top and bottom IDA electrodes were cleaned carefully. The inlet/outlet reservoirs were drilled onto the top IDA electrode prior to the washing step. To obtain ferrocene–modified electrodes, the IDA electrodes exposed to an aqueous 2 mM (Hydrazinocarbonyl)ferrocene solution containing 0.1 M LiClO₄ and the potential of the electrode was cycled three times between +1.2 and +1.8 V (*vs* Ag/AgCl) at 10 mV · s⁻¹. After the electrooxidative grafting of ferrocene, the modified IDA electrodes were rinsed with DI water and dried by N₂. The pretreated IDA electrodes were immersed in 20 mL of anhydrous toluene containing 0.5 mL AHAMTES for 24 h at room temperature to allow the formation of amine–terminated monolayer on glass surfaces. The substrates were taken out from the solution, rinsed with toluene and sonicated in toluene for 3 min. Next, the substrates were cured on a hot

plate at 120°C for 30 min to promote condensation of hydrogen-bonded silanols to form siloxane bonds and converts ammonium ions to the neutral and more reactive amine groups [58]. The amine groups at the surfaces were activated using a homobifunctional cross-linker DSC (20 mM in acetonitrile for 2 h) to amine-reactive NHS esters. A double-sided adhesive film was carefully cut to form a narrow slit by use of a razor blade. After rinsing and drying two IDAs with nitrogen, we put the adhesive film on one IDA and attached the other IDA to that. In this way, there was the double-sided adhesive film between two IDAs and the slit served as a channel that was to be filled with sample solutions. Therefore, the channel height was controlled by the thickness of the adhesive film. To immobilize anti-cTnI (or anti-mouse IgG) onto the DSC-activated surfaces within the channel, 10 µg/mL of anti-cTnI (or anti-mouse IgG) in PBS buffer was injected into the channel and incubated for 1 h, followed by washing with PBS buffer. Then the channel was filled with 1% BSA solution in PBS buffer for 30 min to block excess active groups and nonspecific binding sites on the surface. To detect the target antigen cTnI (or mouse IgG), various concentrations of cTnI (or mouse IgG) in

PBS buffer) in human serum was loaded, incubated for 1 h, and washed with PBS buffer. Following immunoreaction of anti-cTnI and cTnI (or anti-mouse IgG and mouse IgG), 10 $\mu\text{g}/\text{mL}$ of ALP conjugated anti-cTnI (or ALP conjugated anti-mouse IgG) in PBS buffer was injected into the channel and washed with PBS buffer after incubation for 30 min. For the detection of cTnI (or mouse IgG), the channel was filled with 1 mM APP in Tris buffer (50 mM Tris-HCl, 10 mM MgCl_2 , pH 9.0) and kept undisturbed during the enzymatic reaction for 10 min at room temperature.

4.2.5. Electrochemical measurements

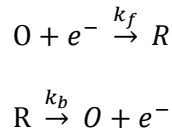
All electrochemical measurements were performed with a CH Instruments (Austin, TX, USA) model 750A electrochemical analyzer. A conventional three-electrode cell assembly was employed throughout the experiments, which involved a working ITO electrode, a platinum wire auxiliary electrode, and an Ag/AgCl reference electrode (RE-6, BASi, Stareton, UK). All potentials are reported versus Ag/AgCl reference at room temperature. Both the reference electrode and auxiliary electrode were immersed into a reservoir. Chronocoulometry

was performed at a generator electrode of +1.0 V and a collector electrode of -0.6 V. The chronocoulometric data were prepared for calibration curves by summing the charge from the generator and collector electrodes.

4.3. Theory

4.3.1. Electrochemical processes

The redox couple considered in this study could be represented by O (oxidized species) and R (reduced species), and their electrode reaction was governed by the following process:



Here k_f and k_b are forward (reduction) and backward (oxidation) rate constants, respectively, and they can be expressed as the following according to Butler–Volmer kinetics:

$$\begin{aligned} k_f &= k_0 \exp\left[\frac{-\alpha F(E - E^{o'})}{RT}\right] \\ k_b &= k_0 \exp\left[\frac{(1 - \alpha)F(E - E^{o'})}{RT}\right] \end{aligned}$$

where k_0 is the standard electron–transfer rate constant, α is the charge transfer coefficient. F is the Faraday constant, E is the applied potential and $E^{o'}$ the formal potential of the redox couple.

The mass transport of O and R species is often governed by diffusion, convection and electromigration according to the Nernst–Planck equation. By considering an unstirred solution

containing an excess supporting electrolyte, the effects of convection and electromigration can be neglected. Thus, the mass transport mechanism of these species is reduced to primarily a diffusion-controlled process:

$$\frac{\partial O}{\partial t} = D_O \nabla^2 O$$

$$\frac{\partial R}{\partial t} = D_R \nabla^2 R$$

where D_O , D_R , C_O and C_R are the diffusion coefficients and the concentrations of the electroactive species O and R , respectively.

For the boundaries, symmetric condition was applied at the two sides of the unit-cells and insulation condition imposed at the gaps. Moreover, inward flux for R and outward flux for O were applied to the generator (j_g) and the collector (j_c), respectively, with

$$j_g = k_0 \exp \left[\frac{-\alpha F (E_t - E^{o'})}{RT} \right] C_O - k_0 \exp \left[\frac{(1 - \alpha) F (E_t - E^{o'})}{RT} \right] C_R$$

$$j_c = k_0 \exp \left[\frac{-\alpha F (0 - E^{o'})}{RT} \right] C_O - k_0 \exp \left[\frac{(1 - \alpha) F (0 - E^{o'})}{RT} \right] C_R$$

4.3.2. Finite element simulations

Finite element simulations (FES) were performed on a Samsung DM-G650 equipped with a quad-core Intel i7-2600

processor (3.4 GHz) and 8 GB of RAM, running on a Windows 7 64-bit operating system. Simulations were carried out using COMSOL Multiphysics v4.3. The simulation was performed over a two-dimensional domain representing the geometry and dimensions of the various type devices employed in our experiments, as simplified in unit cells.

4.4. Results and Discussion

4.4.1. Current amplification by 3D IDA electrode

We fabricated the three-dimensional IDA devices including that with the IDA electrodes on the ceiling as well as the bottom in the microchannel. The goal is to find out the system that can maximize signal amplification by only heterogeneous electron transfer cycling, eventually leading to more sensitive electrochemical enzyme-based immunosensing. The prepared 3D IDA consists of a solution-filled channel and two closely spaced parallel IDA electrodes on the bottom and ceiling. The operation principle of the 3D IDA is plain and straightforward as schematically illustrated in Fig. 4-3. An electroactive species produced at the generator electrodes on the bottom diffuses toward the nearest electrodes, which are the collector electrodes on the bottom or ceiling, to be regenerated electrochemically. Theoretically, it is obvious that shorter distance between the neighboring electrodes would give rise to higher current amplification [59,60]. However, sub-micron scale of vertical distance between bottom and ceiling of the electrodes could be problematic for practical uses: cost to fabricate such IDA devices on a nano-scale, less reliable

irrigation of the solution and more probable malfunction due to clotting of blood samples if not heparinized, etc.. This led us to the 3D IDA platform that was expected to offer significant benefit from efficient electrochemical redox cycling as shown in the results below.

Fig. 4-4 shows the cyclic voltammograms of 1 mM ferrocenedimethanol ($\text{Fc}(\text{MeOH})_2$) in 2 M KCl as supporting electrolyte from the 3D IDA. At first, the generator and collector electrodes of the bottom IDA electrode were shorted to apply the same potential to both of them, working as a single electrode. And the top IDA electrodes on the ceiling were disconnected and we obtained cyclic voltammograms (non-feedback mode). In this case, no redox cycling was expected (dashed line and inset in Fig. 4-4) and thus the low peak current ($i_{\text{pa}} \approx 131 \text{ nA}$) was observed as a result of faradaic reaction limited by linear diffusion. On the other hand, the cyclic voltammogram (red line) in Fig. 4-4 was acquired by scanning potential of the two generator electrodes on the bottom and ceiling, respectively, while the potential of the two collector electrodes was fixed to be constant, -0.2 V (feedback mode). The current in the feedback mode (red line, $i_{\text{lim}} \approx 13 \text{ }\mu\text{A}$) was

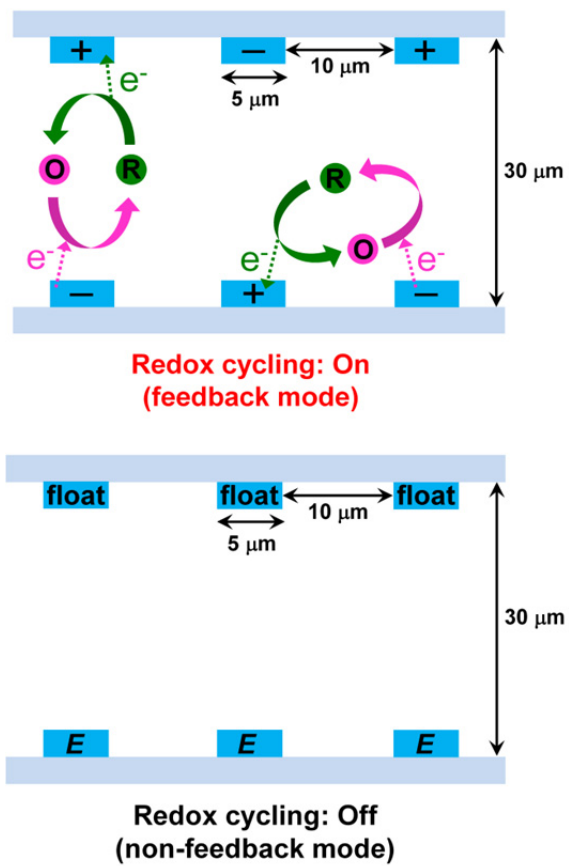


Fig. 4-3 Schematic illustration of redox cycling of the 3D IDA electrode.

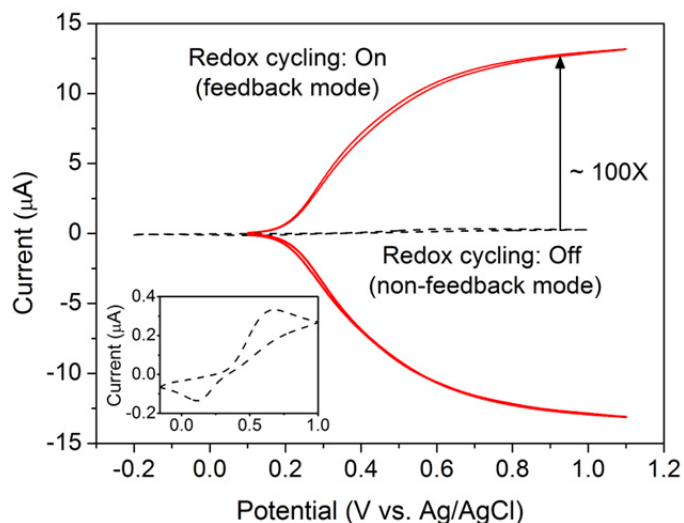


Fig. 4-4 Cyclic voltammograms of 1 mM $\text{Fc}(\text{MeOH})_2$ in 2 M KCl (scan rate $5 \text{ mV} \cdot \text{s}^{-1}$) at the 3D IDA electrode. The IDA electrodes on the bottom were swept while the top IDA electrodes on the ceiling were disconnected (dashed line, magnification shown in inset). The potential of generator electrodes of the top and bottom IDA was swept and the potential of collector IDA electrodes on the bottom and ceiling was held at -0.2 V (red line).

about 100 times higher than that in the non-feedback mode. The symmetric current in the feedback mode of the 3D IDA reveals that the collection efficiency was 99.4%.

4.4.2. Signal amplification of various types of devices

To assess the signal amplification of 3D alignment of IDA electrodes compared with the conventional 2D, we investigated the electrochemical responses of four different types of devices, *i.e.* two straight electrodes in parallel, Open-2D IDA, Closed-2D IDA, and 3D IDA. These devices except the Open-2D IDA had the microchannels with $\sim 30\ \mu\text{m}$ of height, and cut in the adhesive films made the side walls. The Open-2D IDA was directly exposed to bulk solution in the typical electrochemical cell (infinitely large thickness). Fig. 4-5 ~ 4-8 show the cyclic voltammograms obtained from the four types of devices in the presence of 1 mM $\text{Fc}(\text{MeOH})_2$ and 2 M KCl as the supporting electrolyte. The contribution of electrode surface area was eliminated by employing the voltammetric current density, current divided by active electrode surface area, instead of apparently recorded current. The surface area of parallel electrode, Open-2D IDA, Closed-2D IDA, and 3D IDA was

calculated to be about 0.4, 0.005, 0.005, and 0.01 cm^2 , respectively. All of the voltammograms (in the middle column in Fig. 4-5 ~ 4-8) exhibited the typical behavior of IDA, generator-collector system. The steady-state current densities of oxidation and reduction at the generator and collector electrodes, respectively, are perfectly symmetrical. Especially, current density of the 3D IDA was much greater than that of other devices as found in the middle in Fig. 4-8. This behavior tells that the alignment of two IDAs on the bottom and ceiling in the 3D IDA makes considerable contribution to higher signal amplification.

The right column in Fig. 4-5 ~ 4-8 shows the simulated concentration profiles of reduced molecules (C_{red}) for the different types of devices. In the case of the parallel electrode (Fig. 4-5), C_{red} linearly decreases from a maximum at the bottom (reducing) electrode to zero at the top (oxidizing) electrode. Closed-2D IDA is a kind of thin layer cell so that its concentration gradient in the height direction is linear and leads to a slight increase of the faradaic current than infinitely long distance diffusion system of Open-2D IDA (the right column in Fig. 4-6 ~ 4-7). In the 3D IDA, the electrochemical products

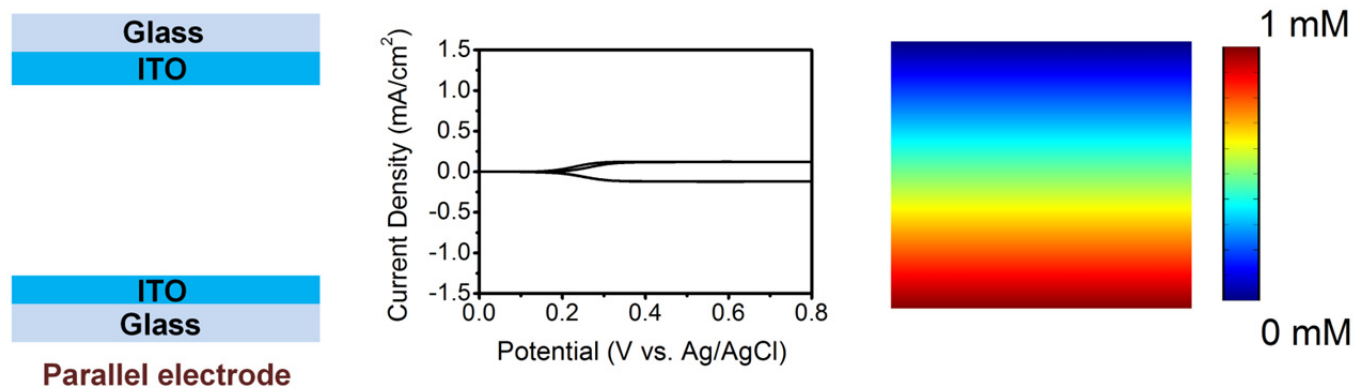


Fig. 4–5 Left side: Schematic diagram of parallel electrode. Middle: Electrode geometry dependence of voltammetric response of 1 mM $\text{Fc}(\text{MeOH})_2$ solution on the parallel electrode. Right side: Concentration profiles of $\text{Fc}(\text{MeOH})_2$ for the parallel electrode under steady–state conditions with applying oxidizing ($E1$) and reducing ($E2$) at the electrodes. The color scale shows the concentration distribution of oxidized molecules for the various types of devices (*red*: fully reduced, *blue*: fully oxidized). The microchannel height was set to be 30 μm .

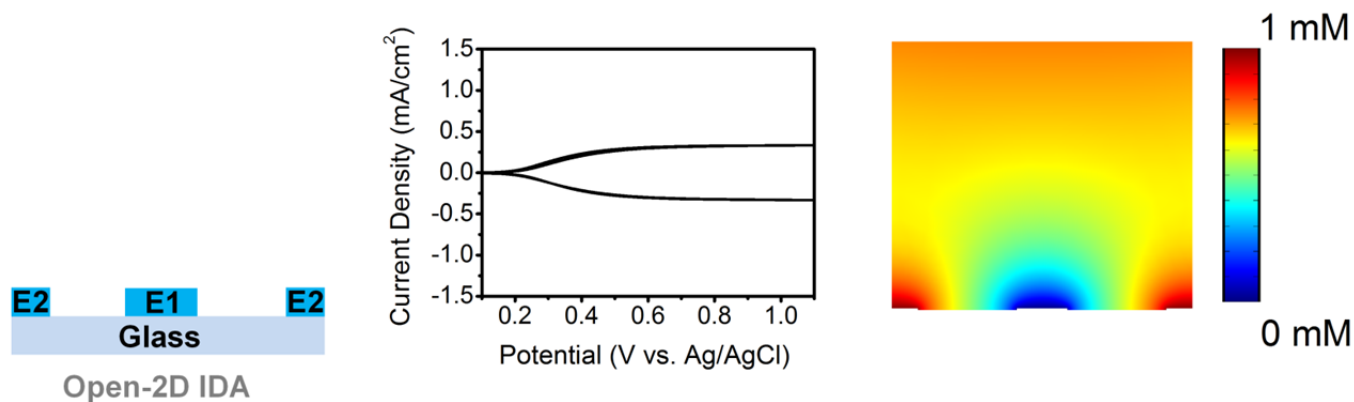


Fig. 4-6 Left side: Schematic diagram of Open-2D IDA. Middle: Electrode geometry dependence of voltammetric response of 1 mM $\text{Fc}(\text{MeOH})_2$ solution on the Open-2D IDA. Right side: Concentration profiles of $\text{Fc}(\text{MeOH})_2$ for the Open-2D IDA under steady-state conditions with applying oxidizing ($E1$) and reducing ($E2$) at the electrodes. The color scale shows the concentration distribution of oxidized molecules for the various types of devices (*red*: fully reduced, *blue*: fully oxidized).

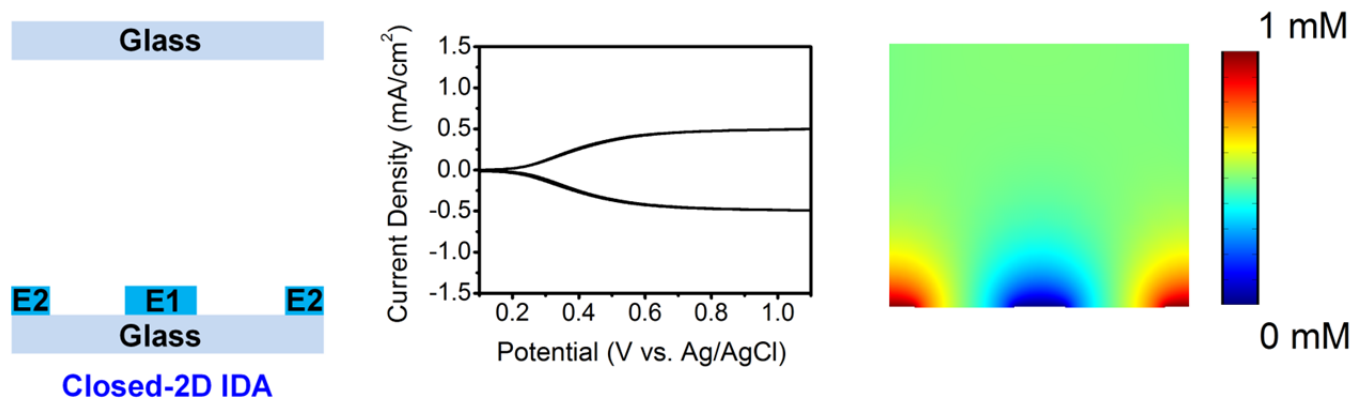


Fig. 4–7 Left side: Schematic diagram of Closed–2D IDA. Middle: Electrode geometry dependence of voltammetric response of 1 mM $\text{Fc}(\text{MeOH})_2$ solution on the Closed–2D IDA. Right side: Concentration profiles of $\text{Fc}(\text{MeOH})_2$ for the Closed–2D IDA under steady–state conditions with applying oxidizing ($E1$) and reducing ($E2$) at the electrodes. The color scale shows the concentration distribution of oxidized molecules for the various types of devices (*red*: fully reduced, *blue*: fully oxidized). The microchannel height was set to be 30 μm .

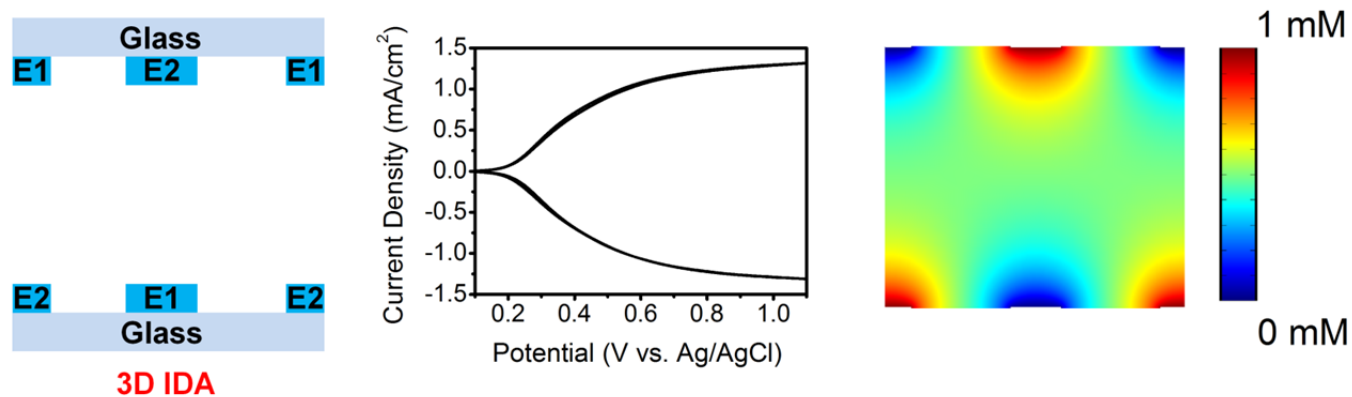


Fig. 4–8 Left side: Schematic diagram of 3D IDA. Middle: Electrode geometry dependence of voltammetric response of 1 mM Fc(MeOH)₂ solution on the 3D IDA. Right side: Concentration profiles of Fc(MeOH)₂ for the 3D IDA under steady-state conditions with applying oxidizing (*E1*) and reducing (*E2*) at the electrodes. The color scale shows the concentration distribution of oxidized molecules for the various types of devices (*red*: fully reduced, *blue*: fully oxidized). The microchannel height was set to be 30 μm .

diffuse to the nearest electrodes on the same plane as well as on the opposite side, and are regenerated. Thus, the concentration gradients in both lateral and vertical directions become much steeper between the top and bottom IDA electrodes. By simulation, we investigated the influence of the distance between top and bottom IDA electrodes, microchannel height, for signal amplification in the 3D IDA. Fig. 4-9 ~ 4-12 present a set of cyclic voltammograms and corresponding concentration profiles as a function of the distance between top and bottom IDA electrodes. The system reaches a steady-state very quickly, within 10 ms, for 30 μm the channel height. As predicted, longer time is needed for longer distance between top and bottom IDA electrodes. Narrower channel height and lateral inter-electrodes spacing lead to higher limiting current owing to steeper concentration gradient resulting from regeneration of reactants at closer places. As stated earlier, the channel height on the sub-micron scale would maximize electrochemical signals, but be unfavorable for practical applications such as electrochemical immunosensing of biological fluid samples. As a consequence of such considerations, the microchannel height of the proposed 3D IDA

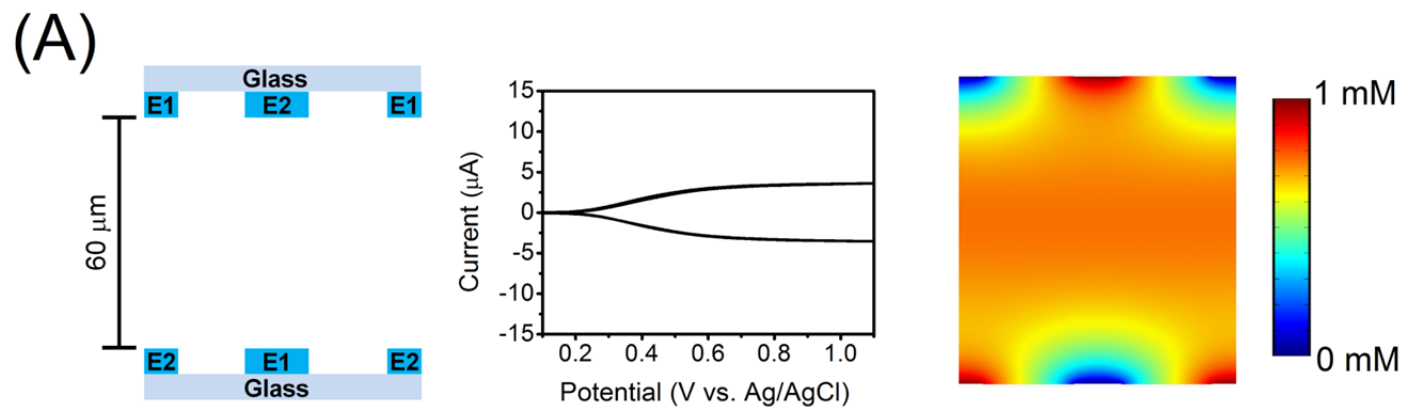


Fig. 4–9 Left side: Schematic diagram of different channel height of the 3D IDA. Middle: Channel height dependence of voltammetric response of 1 mM $\text{Fc}(\text{MeOH})_2$ solution on the device. Right side: Concentration profiles of $\text{Fc}(\text{MeOH})_2$ for the various channel height of the 3D IDA after a minimal time interval of 10 ms with applying oxidizing ($E1$) and reducing ($E2$) potentials at the electrodes. The color scale shows the concentration of oxidized molecules between top and bottom IDA electrodes (*red*: reduced, *blue*: oxidized). The scan rate was $5 \text{ mV} \cdot \text{s}^{-1}$.

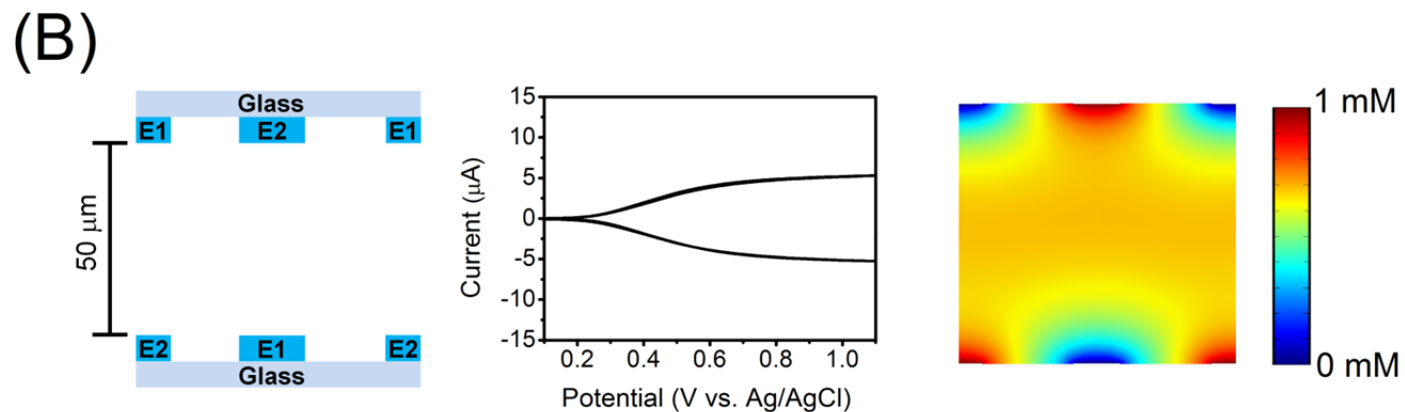


Fig. 4–10 Left side: Schematic diagram of different channel height of the 3D IDA. Middle: Channel height dependence of voltammetric response of 1 mM $\text{Fc}(\text{MeOH})_2$ solution on the device. Right side: Concentration profiles of $\text{Fc}(\text{MeOH})_2$ for the various channel height of the 3D IDA after a minimal time interval of 10 ms with applying oxidizing ($E1$) and reducing ($E2$) potentials at the electrodes. The color scale shows the concentration of oxidized molecules between top and bottom IDA electrodes (*red*: reduced, *blue*: oxidized). The scan rate was $5 \text{ mV} \cdot \text{s}^{-1}$.

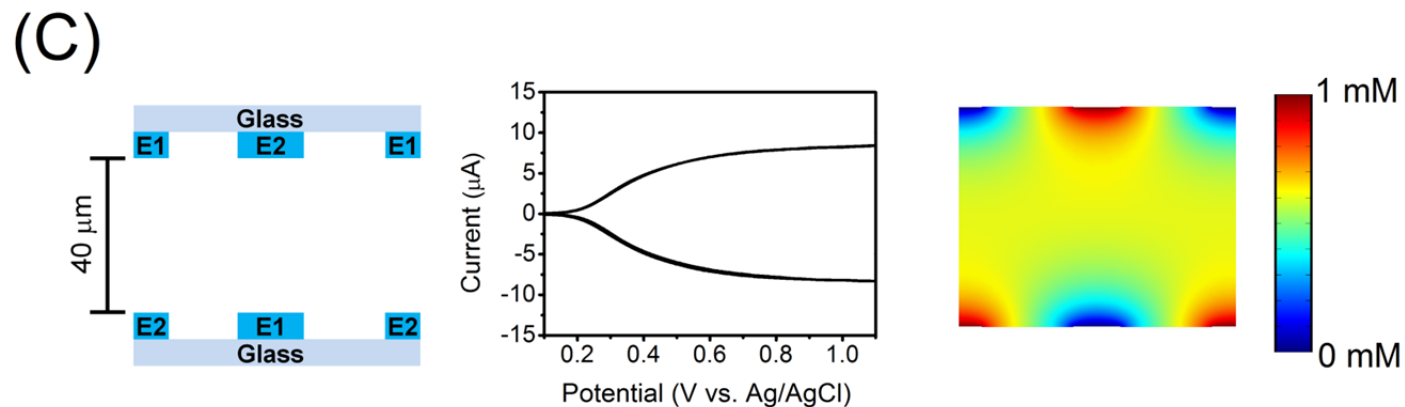


Fig. 4–11 Left side: Schematic diagram of different channel height of the 3D IDA. Middle: Channel height dependence of voltammetric response of 1 mM $\text{Fc}(\text{MeOH})_2$ solution on the device. Right side: Concentration profiles of $\text{Fc}(\text{MeOH})_2$ for the various channel height of the 3D IDA after a minimal time interval of 10 ms with applying oxidizing ($E1$) and reducing ($E2$) potentials at the electrodes. The color scale shows the concentration of oxidized molecules between top and bottom IDA electrodes (*red*: reduced, *blue*: oxidized). The scan rate was $5 \text{ mV} \cdot \text{s}^{-1}$.

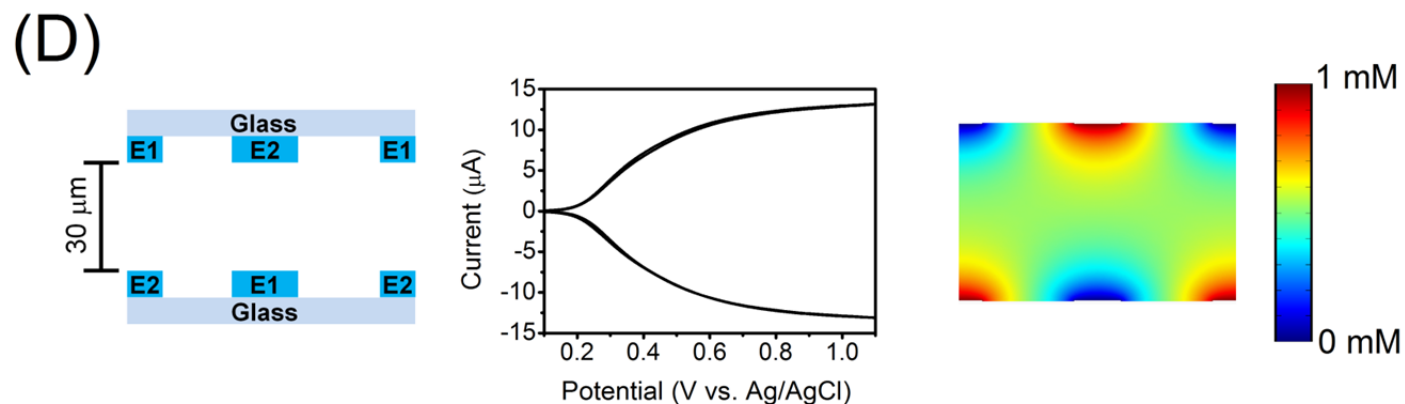


Fig. 4–12 Left side: Schematic diagram of different channel height of the 3D IDA. Middle: Channel height dependence of voltammetric response of 1 mM $\text{Fc}(\text{MeOH})_2$ solution on the device. Right side: Concentration profiles of $\text{Fc}(\text{MeOH})_2$ for the various channel height of the 3D IDA after a minimal time interval of 10 ms with applying oxidizing ($E1$) and reducing ($E2$) potentials at the electrodes. The color scale shows the concentration of oxidized molecules between top and bottom IDA electrodes (*red*: reduced, *blue*: oxidized). The scan rate was $5 \text{ mV} \cdot \text{s}^{-1}$.

platform was chosen to be $\sim 30 \mu\text{m}$.

4.4.3. Electrografting of ferrocene moieties on ITO electrodes

ITO as an electrode material for electrochemical sensors is attractive because of its low background current and high optical transparency. Paradoxically, the low background current of ITO comes from its poor electrocatalytic activity, which is not good for faradaic reaction of reactants. Concerning this problem, ferrocene (Fc) derivatives, whose Fc moiety acts as an electron mediator was immobilized onto ITO surfaces. Among the Fc derivatives, we have chosen the (hydrazinocarbonyl)ferrocene for electrografting agent because it is highly soluble in aqueous media and chemically stable. In this work, we did that by electrooxidative grafting of the terminal hydrazines. Briefly, the potential of the ITO electrode was cycled three times between 1.2 and 1.8 V (*vs.* Ag/AgCl) in an aqueous Fc derivative solution containing 0.1 M LiClO₄. Fig. 4-13 shows cyclic voltammograms obtained during the three consecutive cyclings, exhibiting the characteristic behavior of the electrooxidative grafting of hydrazines [61,62]. In the first

scan (solid line in Fig. 4-13), an irreversible anodic wave appeared at potentials larger than ~ 1.5 V, but the anodic currents dramatically diminished in the subsequent scans (dotted and dashed lines in Fig. 4-13). Initial electrochemical oxidation let the hydrazine-containing derivatives anchored on the ITO surface and inhibited further oxidation. After the electrooxidative grafting process, the resulting electrode was rinsed, and then used to confirm the presence of Fc moieties grafted on ITO surface. Fig. 4-14 shows cyclic voltammograms of a Fc-grafted (solid line) and a bare ITO (dashed line) electrode obtained in 1 M NaClO₄. The Fc-grafted ITO electrode showed reversible redox wave, which was not found on the bare ITO electrode. In addition, the Fc-grafted ITO electrode was robust and stable. Even after ultrasonic rinsing for 15 min in deionized water, the cyclic voltammogram of the Fc-grafted ITO electrode showed no significant change in the peak-shaped current behavior compared with the freshly Fc-grafted ITO electrode. It was also observed that the current linearly increased with scan rate in the range of 5~100 mV · s⁻¹ as expected for surface-confined electroactive species (Fig. 4-15 ~ 4-16). We also verified the presence of iron (Fe) on

the ITO after the electrochemical grafting of the Fc derivative using X-ray photoelectron spectroscopy (XPS) and confirmed the characteristic Fe(2p) peaks (Fig. 4-17A), which were absent on the bare ITO electrode (Fig. 4-17B). These results ensure the presence of Fc moieties on the ITO surface after the electrooxidative grafting process.

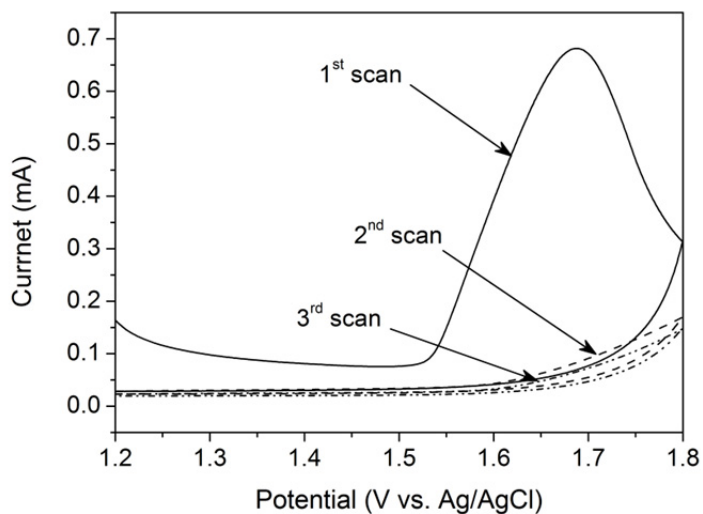


Fig. 4-13 Cyclic voltammograms obtained on ITO in an aqueous 2 mM (hydrazinocarbonyl)ferrocene solution containing 0.1 M LiClO₄. Scan rate was 10 mV · s⁻¹.

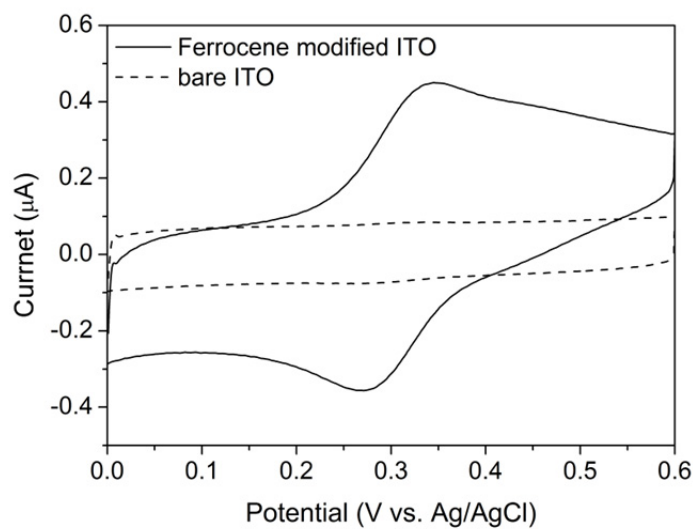


Fig. 4-14 Cyclic voltammograms of a Fc-grafted (solid line) and a bare ITO (dashed line) electrode in 1 M NaClO₄. Scan rate was 20 mV · s⁻¹.

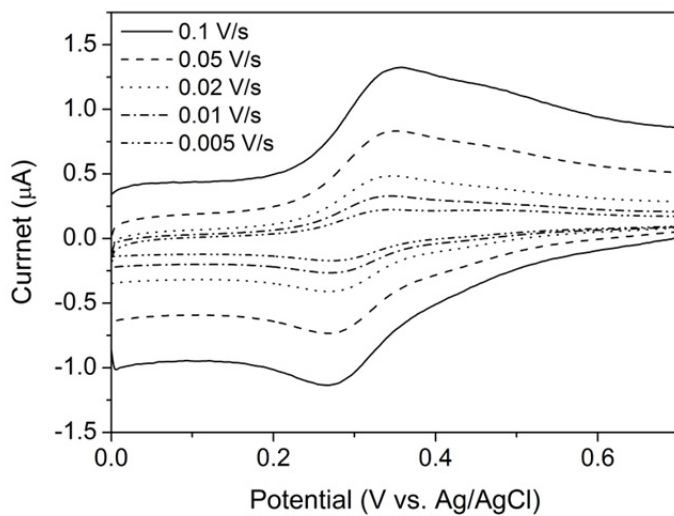


Fig. 4–15 Cyclic voltammograms of Fc–grafted ITO electrode in 1 M NaClO_4 at scan rates from 5 to 100 $\text{mV} \cdot \text{s}^{-1}$.

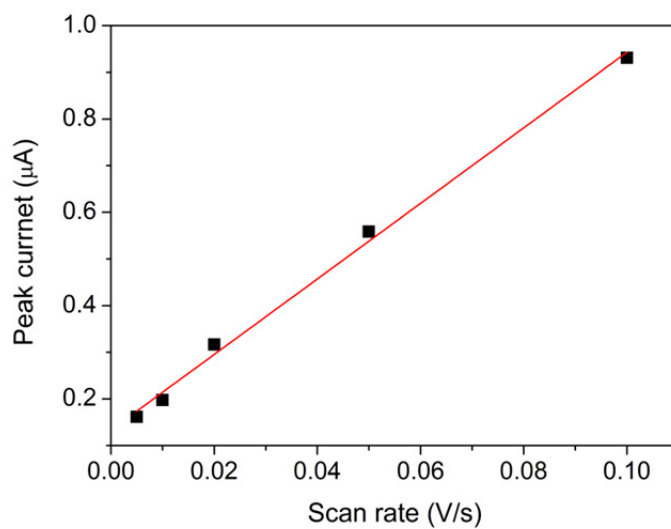


Fig. 4-16 Dependence of the oxidation peak current on the scan rates.

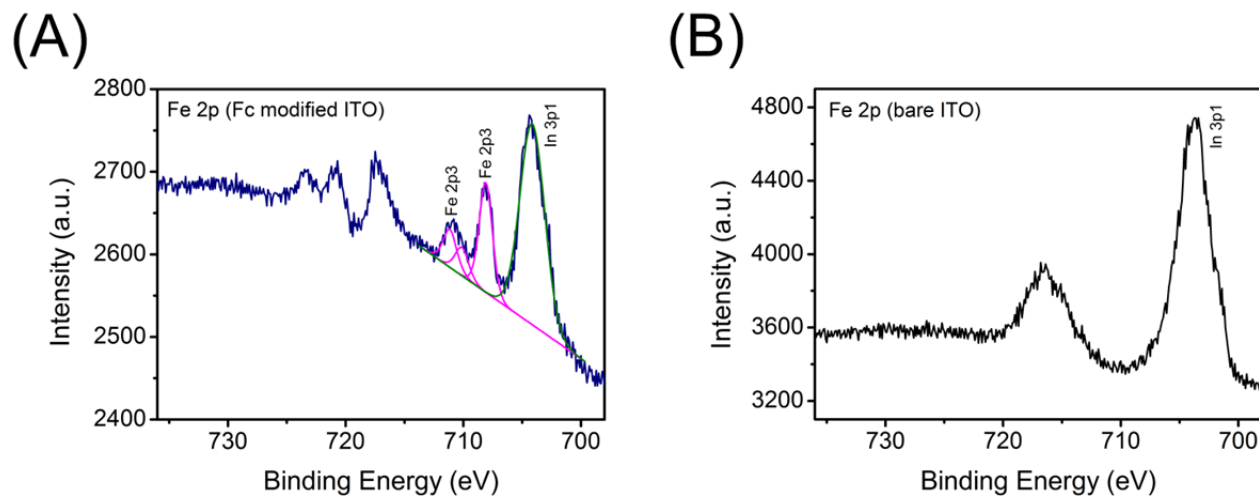


Fig. 4-17 XPS spectra for (A) Fc-modified and (B) a bare ITO electrode.

4.4.4. Immunosensing performance by dependence on electrode geometry

Fig. 4-18A shows the successive step for preparation of an immunosensing layer (see Section 4.2.4. for details). The actual immunosensing scheme is illustrated in Fig. 4-18B. In the sandwich-type heterogeneous immunosensing, the target antigens are captured between the antibody and the ALP-conjugated antibody. ALP converts APP into *p*-aminophenol (AP), which can be electrochemically oxidized to *p*-quinone imine (QI) on the Fc-grafted generator electrodes. The oxidized QI is then reduced back to AP at the collector electrodes, participating in redox cycling. Such a redox cycling process augments the electrochemical signal, leading to higher sensitivity.

In order to evaluate the presented signal amplification strategy for electrochemical immunosensor, we applied it to the detection of mouse IgG. For comparison study, Closed-2D IDA and 3D IDA were employed. Fig. 4-19 shows chronocoulograms obtained at a Closed-2D IDA with a series of concentrations of mouse IgG based on the immunosensing scheme on the left side in Fig. 4-19. Compared with

conventional electroanalytical techniques such as amperometry and linear scan voltammetry, chronocoulometry produces the responses that increased in proportional to the mouse IgG concentration and offered very stable and reproducible responses, indicating the charge was a good index to acquire quantitative information of antigen target in the sample solution. The calibration curve based on the charge data recorded at 300 s gave the calculated detection limit, *ca.* 100 fg/mL (red point and inset in Fig. 4-21). Fig. 4-20 shows a schematic diagram and chronocoulograms from an immunosensing system that employed the 3D IDA. Taking its geometric advantage, electrochemical amplification of effective redox cycling reached the level that was about 100 times higher or more than that of Closed-2D IDA. The detection limit obtained using the 3D IDA was *ca.* 10 fg/mL (black squares in Fig. 4-21). These results clearly showed that the 3D IDA can offer higher sensitivity and lower detection limit to enzyme-based electrochemical immunosensors without additional chemical or biological reagent.

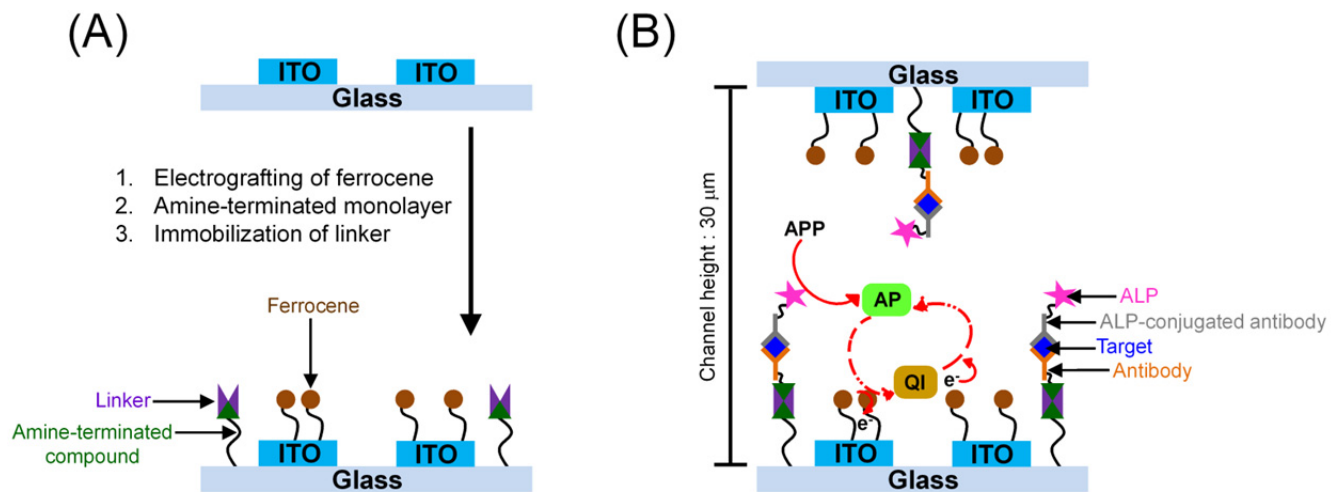


Fig. 4-18 (A) Schematic illustration of the preparation of an immunosensing layer. (B) Schematic view for electrochemical detection of target antigen.

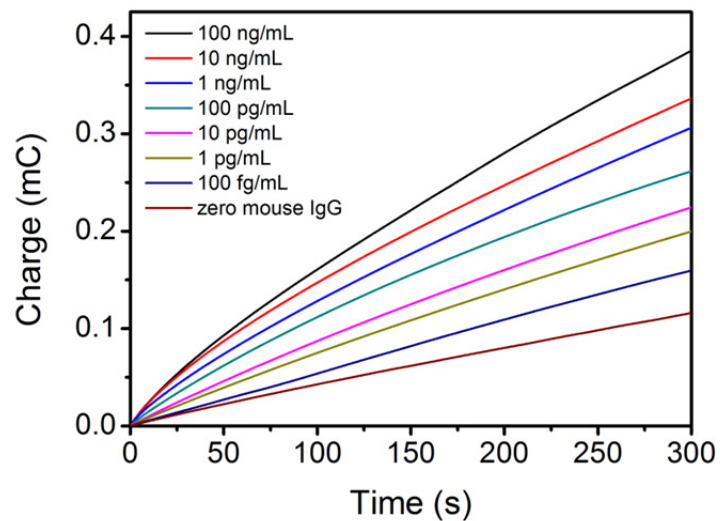
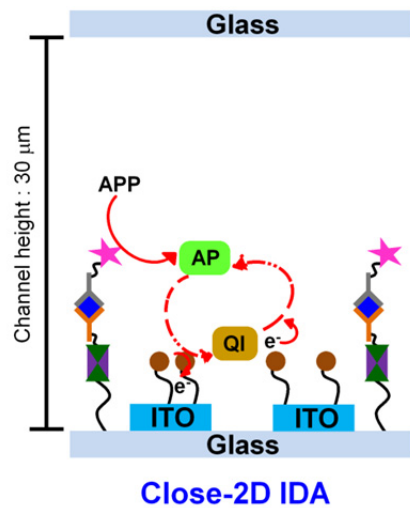


Fig. 4–19 Immunosensing scheme (left) and chronocoulograms (right) of the electrochemical immunosensor for the Closed–2D IDA.

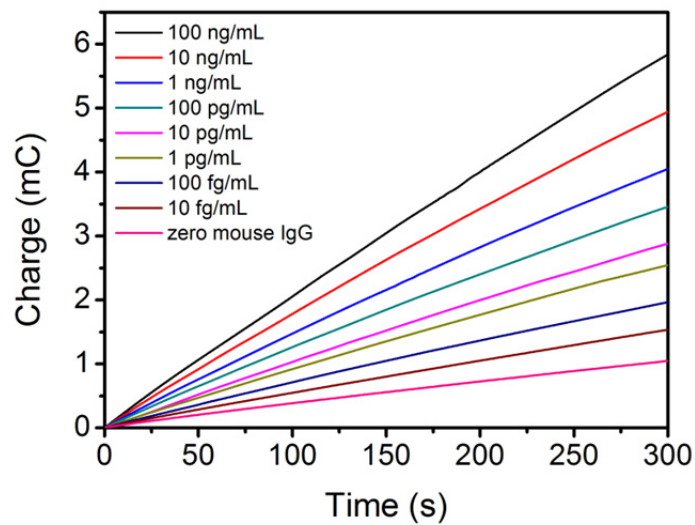
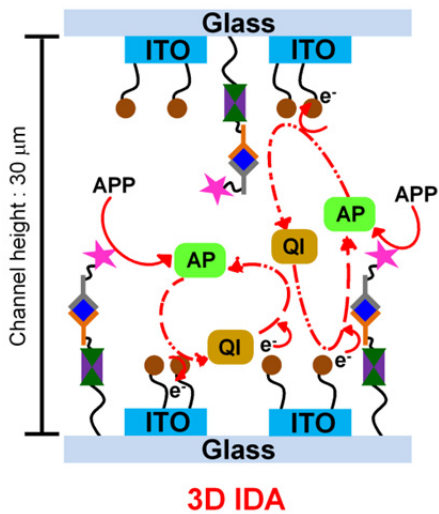


Fig. 4–20 Immunosensing scheme (left) and chronocoulograms (right) of the electrochemical immunosensor for the 3D IDA.

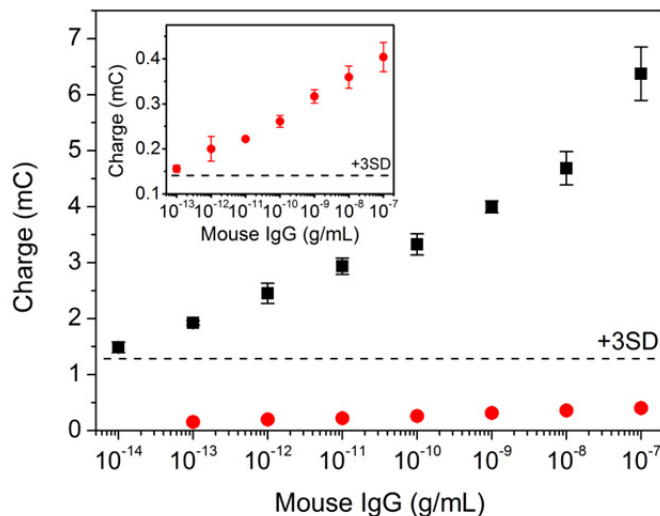


Fig. 4-21 Calibration curves obtained with Closed-2D IDA (red circles, magnification shown in inset) and 3D IDA (black squares) electrodes for the detection of mouse IgG. The dashed line corresponds to three times the standard deviation of the charge at the concentration of zero. The error bars represent the standard deviations taken from at least three independent measurements.

4.4.5. Sensitive detection of cTnI using 3D IDA electrode

Encouraged by the enhanced signal amplification of the 3D IDA, we explored the feasibility of the 3D IDA as an electrochemical immunosensor platform for the detection of cTnI, which is a specific biomarker of myocardial damage. It is well known that cTnI can be also used for therapeutic monitoring and risk stratification of acute myocardial infarction (AMI) [63]. Fig. 4-22 shows the representative chronocoulograms from 3D IDA for various concentrations of cTnI, which were spiked into human sera. The detection limit was ca. 100 fg/mL from the signal-to-noise ratio of 3 on the basis of the standard deviation (SD) at a zero concentration of cTnI (Fig. 4-23). This shows that the electrochemical signal amplification for immunosensing can be much more efficient by introducing 3D IDA platform for clinical analysis of cTnI in human serum.

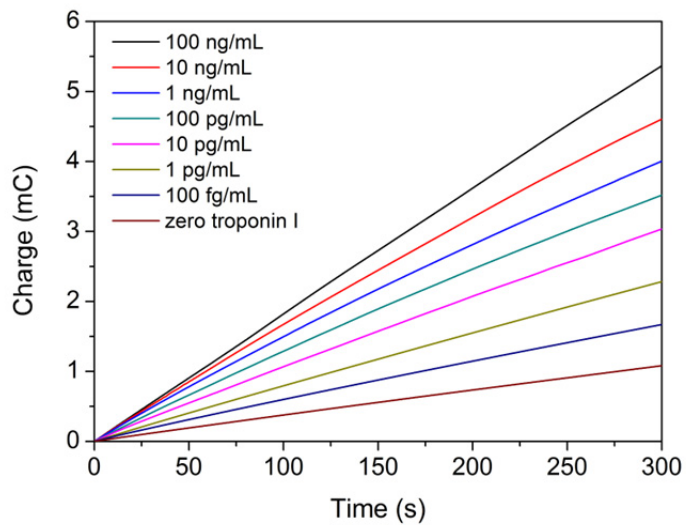


Fig. 4-22 Chronocoulograms obtained with the 3D IDA for various concentration of cTnI in human serum.

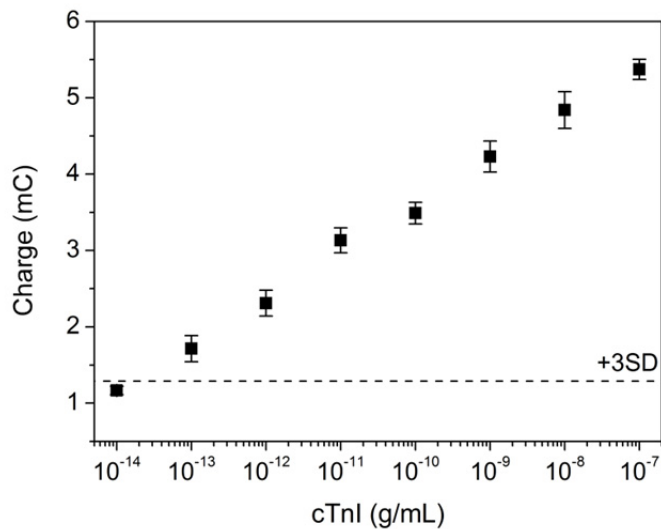


Fig. 4–23 Calibration curve for the detection of cTnI. The dashed line corresponds to three times the standard deviation of the charge at the concentration of zero. The error bars denote the standard deviations taken from at least three independent measurements.

4.5. Conclusion

We proposed and demonstrated a new strategy for signal amplification based on geometrically efficient redox cycling in the 3D IDA device that contained a thin layer of solution confined between two closely spaced parallel IDA electrodes. The proposed 3D IDA device was fabricated and proved to successfully work as a generator–collector system with nearly perfect collection efficiency. The signal amplification was a sensitive function of geometric configuration, inter–electrodes distance, generator–collector spacing of IDA electrodes on the bottom and ceiling. Considering various factors for practical immunoassay, the channel dimension of 3D IDA device was carefully chosen. The poor electrocatalytic surface of the ITO electrodes was modified by electrografting electron–mediating materials. The combination between 3D IDA and modified ITO enabled extra amplification, which was markedly strong, of electrochemical enzymatic immunosensing signals of target antigen, mouse IgG and cTnI. Importantly, the proposed and demonstrated method in this work requires no addition of chemical reagent or biological additives such as redox enzymes. The signal amplification in this work can be directly applied to

practical sensors owing to its compatibility with the general ELISA-based procedure, saving the effort for modifying the analytical procedure. Furthermore, this method can be combined with other analytical units, *e.g.* chip-based Coulter counter [64,65], for blood analysis and allow integration of parallel immunosensors for multiple targets on a single chip. We envision that this approach will provide a general protocol in fabricating more sensitive and integrated redox cycling-based biosensors.

4.6. References

- [1] S. Brakmann, *Angew. Chem., Int. Ed.* **2004**, *43*, 5730.
- [2] N. L. Rosi, C. A. Mirkin, *Chem. Rev.* **2005**, *105*, 1547.
- [3] N. C. Tansil, Z. Gao, *Nano Today* **2006**, *1*, 28.
- [4] W. Xu, X. Xue, T. Li, H. Zeng, X. Liu, *Angew. Chem., Int. Ed.* **2009**, *48*, 6849.
- [5] J. Wang, Y. Shan, W.-W. Zhao, J.-J. Xu, H.-Y. Chen, *Anal. Chem.* **2011**, *83*, 4004.
- [6] A. Fu, W. Hu, L. Xu, R. J. Wilson, H. Yu, S. J. Osterfeld, S. S. Gambhir, S. X. Wang, *Angew. Chem., Int. Ed.* **2009**, *48*, 1620.
- [7] B. S. Munge, A. L. Coffey, J. M. Doucette, B. K. Somba, R. Malhotra, V. Patel, J. S. Gutkind, J. F. Rusling, *Angew. Chem., Int. Ed.* **2011**, *50*, 7915.
- [8] R. Freeman, X. Liu, I. Willner, *J. Am. Chem. Soc.* **2011**, *133*, 11597.
- [9] J. Wang, G. Liu, M. H. Engelhard, Y. Lin, *Anal. Chem.* **2006**, *78*, 6974.
- [10] S. Zanarini, E. Rampazzo, L. D. Ciana, M. Marcaccio, E. Marzocchi, M. Montalti, F. Paolucci, L. Prode, *J. Am. Chem. Soc.* **2009**, *131*, 2260.
- [11] S. Hwang, E. Kim, J. Kwak, *Anal. Chem.* **2005**, *77*, 579.

- [12] T. Porstmann, S. T. Kiessig, *J. Immunol. Methods* **1992**, *150*, 5.
- [13] J. Wang, G. Liu, M. R. Jan, *J. Am. Chem. Soc.* **2004**, *126*, 3010.
- [14] I. Rosen, J. Rishpon, *J. Electroanal. Chem.* **1989**, *258*, 27.
- [15] M. Santandreu, F. Céspedes, S. Alegret, E. Martínez-Fàbregas, *Anal. Chem.* **1997**, *69*, 2080.
- [16] H. T. Tang, C. E. Lunte, H. B. Halsall, W. R. Heineman, *Anal. Chim. Acta* **1988**, *214*, 187.
- [17] Z. P. Aguilar, W. R. Vandaveer IV, I. Fritsch, *Anal. Chem.* **2002**, *74*, 3321.
- [18] J. Wang, A. Ibáñez, M. P. Chatrathi, A. Escarpa, *Anal. Chem.* **2001**, *73*, 5323.
- [19] H. M. Nassef, M. C. B. Redondo, P. J. Ciclitira, H. J. Ellis, A. Frago, C. K. O'Sullivan, *Anal. Chem.* **2008**, *80*, 9265.
- [20] N. J. Forrow, N. C. Foulds, J. E. Frew, J. T. Law, *Bioconjugate Chem.* **2004**, *15*, 137.
- [21] S. Zhao, J. H. T. Luong, *Anal. Chim. Acta* **1996**, *327*, 235.
- [22] A. J. Bergren, M. D. Porter, *J. Electroanal. Chem.* **2007**, *599*, 12.
- [23] M.-Y. Wei, L.-H. Guo, H. Chen, *Microchim. Acta* **2006**,

155, 409.

[24] D. Zheng, N. Wang, F.-Q. Wang, D. Dong, Y.-G. Li, X.-Q. Yang, L.-H. Guo, J. Cheng, *Anal. Chim. Acta* **2004**, *508*, 225.

[25] W. R. Vandaveer IV, D. J. Woodward, I. Fritsch, *Electrochim. Acta* **2003**, *48*, 3341.

[26] C. Ma, N. M. Contento, L. R. Gibson II, P. W. Bohn, *ACS Nano* **2013**, *7*, 5483.

[27] A. L. Ghindilis, A. Makower, C. G. Bauer, F. F. Bier, F. W. Scheller, *Anal. Chim. Acta* **1995**, *304*, 25.

[28] B. Limoges, D. Marchal, F. Mavr e, J. M. Sav eant, *J. Am. Chem. Soc.* **2006**, *128*, 6014.

[29] S. Park, A. Singh, S. Kim, H. Yang, *Anal. Chem.* **2014**, *86*, 1560.

[30] Y. Astier, P. N. Bartlett, *Bioelectrochemistry* **2004**, *64*, 15.

[31] C. J. Stanley, R. B. Cos, M. F. Cardosi, A. P. F. Turner, *J. Immunol. Methods* **1998**, *112*, 153.

[32] J. Das, M. A. Aziz, H. Yang, *J. Am. Chem. Soc.* **2006**, *128*, 16022.

[33] J. Das, K. Jo, J. W. Lee, H. Yang, *Anal. Chem.* **2007**, *79*, 2790.

[34] A. Walter, J. Wu, G.-U. Flechsig, D. A. Haake, J. Wang.

- Anal. Chim. Acta* **2011**, *689*, 29.
- [35] M. R. Akanda, M. A. Aziz, K. Jo, V. Tamilavan, M. H. Hyun, S. Kim, H. Yang, *Anal. Chem.* **2011**, *83*, 3926.
- [36] M. R. Akanda, Y.-L. Choe, H. Yang, *Anal. Chem.* **2012**, *84*, 1049.
- [37] U. Wollenberger, F. Schubert, D. Pfeiffer, F. W. Scheller, *Trends Biotechnol.* **1993**, *11*, 255.
- [38] B. Serra, M. D. Morales, J. Zhang, A. J. Reviejo, E. H. Hall, J. M. Pingarron, *Anal. Chem.* **2005**, *77*, 8115.
- [39] C. G. Bauer, A. V. Eremenko, E. Ehrentreich-Förster, F. F. Bier, A. Makower, H. B. Halsall, W. R. Heineman, F. W. Scheller, *Anal. Chem.* **1996**, *68*, 2453.
- [40] T. J. Moore, M. J. Joseph, B. W. Allen, L. A. Coury Jr, *Anal. Chem.* **1995**, *67*, 1896.
- [41] A. Warsinke, A. Benkert, F. W. Scheller, *Fresenius J. Anal. Chem.* **2000**, *366*, 622.
- [42] O. Niwa, *Electroanalysis* **1995**, *7*, 606.
- [43] B. Elsholz, R. Wörl, L. Blohm, J. Albers, H. Feucht, T. Grunwald, B. Jürgen, T. Schweder, R. Hintsche, *Anal. Chem.* **2006**, *78*, 4794.
- [44] J. H. Thomas, S. K. Kim, P. J. Hesketh, H. B. Halsall, W. R.

- Heineman, *Anal. Chem.* **2004**, *76*, 2700.
- [45] O. Niwa, M. Morita, H. Tabei, *Anal. Chem.* **1990**, *62*, 447.
- [46] K. Hayashi, Y. Iwasaki, T. Horiuchi, K. Sunagawa, A. Tate, *Anal. Chem.* **2005**, *77*, 5236.
- [47] M. Morita, O. Niwa, T. Horiuchi, *Electrochim. Acta* **1997**, *42*, 3177.
- [48] K. Ueno, M. Hayashida, J.-Y. Ye, H. Misawa, *Electrochem. Commun.* **2005**, *7*, 161.
- [49] J. H. Thomas, S. K. Kim, P. J. Hesketh, H. B. Halsall, W. R. Heineman, *Anal. Biochem.* **2004**, *328*, 113.
- [50] T. Ito, K. Maruyama, K. Sobue, S. Ohya, O. Niwa, K. Suzuki, *Electroanalysis* **2004**, *16*, 2035.
- [51] T. R. L. C. Paixão, E. M. Richter, J. G. A. Brito-Neto, M. Bertotti, *J. Electroanal. Chem.* **2006**, *596*, 101.
- [52] B. Wolfrum, M. Zevenbergen, S. Lemay, *Anal. Chem.* **2008**, *80*, 972.
- [53] S. Han, J. Zhai, L. Shi, X. Liu, W. Niu, H. Li, G. Xu, *Electrochem. Commun.* **2007**, *9*, 1434.
- [54] S. Vesztergom, M. Y. G. G. Láng, *Electrochem. Commun.* **2011**, *13*, 378.
- [55] T.-H. Yang, S. Venkatesan, C.-H. Lien, J.-L. Chang, J.-

- M. Zen, *Electrochim. Acta* **2011**, *56*, 6205.
- [56] W. Zhang, I. Gaberman, M. Ciszowska, *Electroanalysis* **2003**, *15*, 409.
- [57] B. Jin, W. Qian, Z. Zhang, H. Shi, *J. Electroanal. Chem.* **1996**, *411*, 29.
- [58] J. Kim, G. J. Holinga, G. A. Somorjai, *Langmuir* **2011**, *27*, 5171.
- [59] M. A. G. Zevenbergen, D. Krapf, M. R. Zuiddam, S. G. Lemay, *Nano Lett.* **2007**, *7*, 384.
- [60] M. A. G. Zevenbergen, B. L. Wolfrum, E. D. Goluch, P. S. Singh, S. G. Lemay, *J. Am. Chem. Soc.* **2009**, *131*, 11471.
- [61] K. Malmos, J. Iruthayaraj, R. Ogaki, P. Kingshott, F. Besenbacher, S. U. Pedersen, K. Daasbjerg, *J. Phys. Chem. C* **2011**, *115*, 13343.
- [62] K. Malmos, J. Iruthayaraj, S. U. Pedersen, K. Daasbjerg, *J. Am. Chem. Soc.* **2009**, *131*, 13926.
- [63] U. Friess, M. Stark, *Anal. Bioanal. Chem.* **2009**, *393*, 1453.
- [64] H. Choi, K. B. Kim, C. S. Jeon, I. Hwang, S. Lee, H. K. Kim, H. C. Kim, T. D. Chung, *Lab Chip* **2013**, *13*, 970.
- [65] H. Choi, C. S. Jeon, I. Hwang, J. Ko, S. Lee, J. Choo, J.-H. Boo, H. C. Kim, T. D. Chung, *Lab Chip* **2014**, DOI:

10.1039/c4lc00238e.

5. Electrografting of an ITO Surface with Amine-Terminated Dendrimers and its Application to Electrocatalytic Reaction

5.1. Introduction

Surface functionalization has attracted considerable interest in recent years with the aim of designing surfaces with tailored properties (*e.g.* wettability, corrosion resistance, adhesion, lubricants, and biocompatibility) or operating functions ('smart' surfaces bearing stimuli-responsive architectures) [1–4]. Electrode surfaces modified by surface functionalization find applications in molecular electronics [5], bioelectronics [6,7], and in the development of charge transport devices [8] or sensors [9]. Particularly crucial for sensor studies, the controlled grafting of monolayers allows the design of complex recognition interfaces and provides responses (akin to those at the molecular level) for the associated transduction reactions [10].

There are three major issues involved in constructing such interfaces: control of the thickness and density of the deposited layer, which ideally, as a first step, requires the formation of a

monolayer, spatial control of the connected functional groups and robustness of the deposited layer versus temperature, solvents, and aging.

The most popular strategy for fabricating monolayers is the spontaneous two-dimensional adsorption of thiol derivatives, especially alkanethiols, onto the coinage metals (Pt, Au, Ag, Cu) to form self-assembled monolayers (SAMs) (Fig. 5-1) [11]. Although highly versatile, this strategy suffers from important limitations pertaining to the lack of thermal and long-term stability, narrow electrochemical window, and stochastic behavior of the gold-thiolate bond [11-13]. Besides, the spatial control of covalently bound functional groups is particularly difficult to achieve. Indeed, the direct self-assembly of alkylthiols covalently connected at their extremities to functional substrate generally leads to a 'bouquet'-like appearance for the objects on the surface, with empty spaces in between [11]. Dilution strategies with unfunctionalized alkylthiols allows tight packing of the alkyl chains on the surface and simultaneous connection of large functional objects on the surface, leading to small 'islands of objects', rather than a uniform distribution of objects on the

surface [14–18]. An alternative strategy for connecting organic moieties onto electrodes is the reductive grafting of aryldiazonium salts, resulting in the covalent attachment of phenyl derivatives onto the surface.

Electrografting, in particular, has gained tremendous attention over the last decade and is now a well–recognized method for surface functionalization [19–22]. Contrary to alkylthiol SAMs, the organic layers obtained from this method are generally highly stable, and are strongly resistant to heat, chemical degradation, and ultrasonication [19,23]. Furthermore, the method is easy to carry out and rapid (deposition time on the order of 10 s instead of 10~18 h for well–organized thiol–Au SAMs), and can be applied to a wide range of materials: carbon (graphite, glassy carbon, nanotubes, diamond), metals (Fe, Co, Ni, Cu, Zn, Pt, Au), semiconductors (SiH, SiO₂, SiOC...), indium tin oxide (ITO), and even organic polymers and dyes [21].

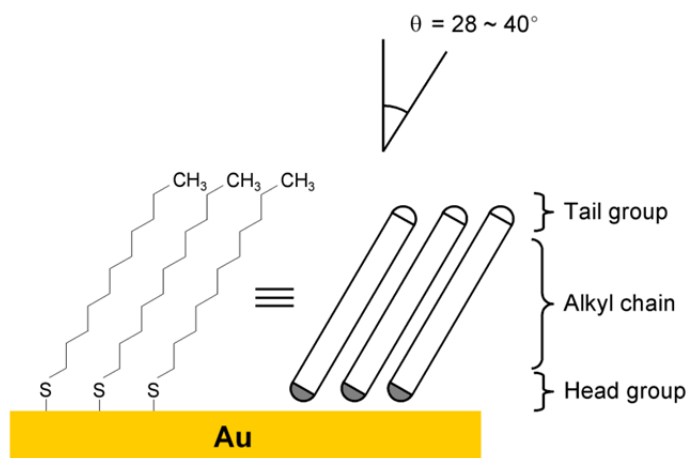


Fig. 5-1 Structure of alkythiols self-assembled monolayers.

Dendrimers are precise cauliflower-shaped macromolecules constructed from the central core, in either a divergent or a convergent way. In each generation, the number of branches increases two- (1 → 2 connectivity) or three-fold (1 → 3 connectivity). After several generations, the size of a dendrimer matches those of biological components. Their topologies afford desirable locations for the active sites (*e.g.* redox sites), and this combination makes them a powerful tool for studies of electron-transfer kinetics and thermodynamic parameters in biosystems [24]. Dendrimers have been the subject of extraordinary synthetic development in the fields of inorganic [25], organometallic [26,27], biochemical [28] and energy materials [29]. The large variety in structure and engineered functionalities [27] has endowed dendrimers with electron-transfer processes, which have far-reaching implications, for both fundamental studies and practical applications.

In this chapter, we report that amine-terminated dendrimers can be electrochemically grafted onto ITO surfaces, which can then be applied for spatially controlled functionalization of ITO with catalytic nanoparticles and electroactive materials. As

model systems, we prepared two different dendrimers, *i.e.* partially tethered ferrocenyl dendrimers (Fc-Ds) and Pt dendrimer-encapsulated nanoparticles (Pt DENs), using amine-terminated sixth generation polyamidoamine (G6-NH₂ PAMAM) dendrimers, and subsequently immobilized the dendrimers onto ITO surfaces via electrooxidative grafting of the terminal amines of dendrimers to the surfaces. The electrochemical experiments confirmed the immobilization of the different types of dendrimers onto the ITO surface. We also demonstrated the spatially controlled surface modification of ITO with catalytic dendrimers by applying the method to the ITO microelectrodes. The resulting electrografted dendrimer films were electrocatalytically active for the *p*-aminophenol redox reaction.

5.2. Experimental

5.2.1. Chemicals and materials

All reagents were used as received without further purification. Amine-terminated sixth-generation PAMAM (G6-NH₂ PAMAM) dendrimers, MgCl₂, K₂PtCl₄, NaBH₄, NaClO₄, LiClO₄, 1,1'-ferrocenedimethanol, ferrocenecarboxaldehyde, 4-aminophenol, and cellulose dialysis sacks (MW cutoff of 12,000) were purchased from Sigma-Aldrich (St. Louis, MO, USA). Tris(hydroxymethyl)aminomethane (Tris) was obtained from Acros (Geel, Belgium). Hexamethyldisilazane (HMDS), sulfuric acid, methanol, ethanol, and acetone were received from J. T. Baker (Phillipsburg, NJ, USA). 4-aminophenyl phosphate (APP) monosodium salt hydrate was purchased from Gold biotechnology[®] (St. Louis, MO, USA). Acetonitrile, sodium hydroxide, and hydrochloric acid were purchased from Daejung (Siheung, Korea). Tris buffer (pH 9.0) solution contained 50 mM Tris and 10 mM MgCl₂, and the pH was adjusted by adding 1.0 M HCl dropwise. 18 M Ω ·cm deionized (DI) water was used to prepare all aqueous solutions (Barnstead NANOpure[®], Thermo Scientific Inc., USA).

5.2.2. Synthesis of Pt DENs

200 mol equiv of an aqueous 200 mM K_2PtCl_4 was added to an aqueous 10 μ M G6-NH₂ PAMAM dendrimer solution. The mixture solutions were stirred for complete complexation between the metal ions and the interior amines of the dendrimers. Especially, the mixture (pH 5) of Pt ions and dendrimers was stirred for 76 h to ensure the complexation of the Pt ions to the intradendrimer tertiary amines. A stoichiometric excess of aqueous NaBH₄ was then added to the complex solution under vigorous stirring. Specifically, a 20-fold excess of NaBH₄ was added to the Pt ion-dendrimer complex solution. We kept the mixture solution (pH 7~8) in a closed vial for 24 h to ensure complete reduction of the complexed Pt ions. Finally, the synthesized Pt DENs solutions were dialyzed for 24 h using cellulose dialysis sacks to remove impurities.

5.2.3. Preparation of the Fc-D-modified ITO electrode

A schematic of the preparation of an Fc-D-modified layer is shown in Fig. 5-2. Briefly, an ITO electrode was ultrasonically and successively cleaned using ethanol, acetone, and water, and

subsequently dried with a stream of N₂. Then, the ITO electrode was cleaned further in a plasma cleaner/sterilizer (PDC-32G, Harrick Scientific, USA) at high power for 3 min. Immediately after the plasma treatment, the ITO electrodes were exposed to an aqueous 10 μM G6-NH₂ PAMAM dendrimer solution containing 0.1 M LiClO₄, and the potential of the electrode was cycled three times between 1.20 and 1.75 V (vs. Ag/AgCl) at 10 mV · s⁻¹. After the electrooxidative grafting of the terminal amines of dendrimers, the modified ITO electrodes were rinsed with DI water and dried using N₂. To immobilize the ferrocene onto the amine-terminated surfaces, 1 mM ferrocenecarboxaldehyde in methanol was incubated for 2 h followed by the slow addition of 0.5 M NaBH₄, and incubation for 1 h to reduce the carbon-nitrogen double bonds. After immobilization, the modified ITO electrodes were rinsed with methanol, ultrasonicated in DI water thoroughly for 3 min, and then blow-dried.

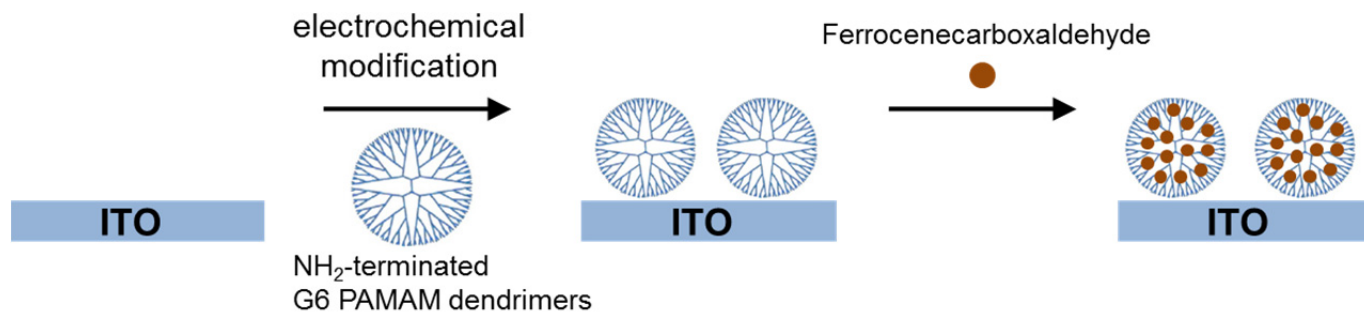


Fig. 5-2 Schematic illustration of the preparation of Fc-D modified ITO electrode.

5.2.4. Modification of ITO surfaces with Pt DENs

An ITO electrode was successively cleaned with ethanol, acetone, and water, and subsequently dried with a stream of N₂. The ITO electrode was cleaned further in a plasma cleaner/sterilizer at high power for 3 min. Immediately after the plasma treatment, the electrode was exposed to an aqueous 10 μM Pt DEN solution containing 0.1 M LiClO₄, and the potential of the electrode was cycled five times between 1.2 and 1.8 V (*vs.* Ag/AgCl) at a scan rate of 10 mV · s⁻¹. After the electrooxidative grafting of Pt DENs, the modified ITO was rinsed using DI water, ultrasonicated in DI water thoroughly for 3 min, and then blow-dried.

5.2.5. Fabrication of IDA microelectrode

The interdigitated array (IDA) microelectrodes were fabricated by standard photolithography and etching processes. ITO-coated glass slides (75 mm × 25 mm, 1.1 mm thick, Sigma-Aldrich, USA) were used as substrates. An ITO-coated glass slide was sequentially cleaned with ethanol, acetone, and DI water sequentially. After removing the moisture on the surface with an air blower, the cleaned ITO substrate was

dehydrated on a hot plate at 120°C for 3 min and then cooled to room temperature. The substrate was spin-coated (YS-100MD, Won Corp., Korea) with HMDS at 7000 rpm for 30 s. The HMDS-coated substrate was placed on a hot plate at 120 °C for 90 s and subsequently cooled at room temperature. Afterwards, the photoresist (PR; AZ4620, Clariant, USA) coated the surface of the substrate using a spin coater at 7000 rpm for 30 s. After soft baking the PR-coated substrate at 100°C for 90 s, the substrate was cooled at room temperature for 90 s immediately. Then, the substrate was aligned under a pattern-designed mask, and exposed to UV light (365 nm) for 11 s with a UV aligner (MDE-4000, Midas, Korea). The UV-exposed substrate was immersed into the AZ400K developer (Clariant, USA) for developing UV-exposed PR. The substrate was then washed with DI water and dried in clean air. Next, the substrate was hard-baked on a hot plate at 120°C for 15 min. After cooling at room temperature, the PR-patterned ITO substrate was etched with an etchant solution (TE-100, Transene Company, Inc., USA) at 60°C for 13 min, which resulted in formation of IDA ITO microelectrodes. All photoresist residues were removed by rinsing the ITO

microelectrodes with acetone using an ultrasonic cleaner (3510E-DTH, Branson, USA) for 2 min. The IDA microelectrode consisted of 25 pairs of microbands. The band length of the IDA was 2 mm and the width was 5 μm , and the gap was 10 μm .

5.2.6. Electrochemical measurements

All electrochemical measurements were performed with a CH Instruments (Austin, TX, USA) model 750A electrochemical analyzer. A conventional three-electrode cell assembly was employed throughout the experiments, which involved a working ITO electrode, a platinum wire counter electrode, and an Ag/AgCl reference electrode (RE-6, BASi, Stareton, UK). All potentials are reported versus Ag/AgCl reference at room temperature.

5.3. Results and Discussion

5.3.1. Preparation and characterization of Fc-D-modified electrodes

The immobilization of amine-terminated PAMAM dendrimers on the ITO surface was performed by electrooxidative grafting of the terminal amines. Briefly, the potential of the electrode was cycled three times between 1.25 and 1.75 V (*vs.* Ag/AgCl) in an aqueous 10 μ M G6-NH₂ PAMAM dendrimer solution containing 0.1 M LiClO₄. Fig. 5-3 shows the cyclic voltammograms obtained during the three consecutive scans. In the first scan (solid line in Fig. 5-3), an irreversible anodic wave appears at potentials larger than \sim 1.5 V. This has been previously attributed to the electrochemical oxidation of the amine group to its cation radical, which was followed by the formation of an oxygen-nitrogen bond on the ITO electrode. When the potential was repeatedly scanned (dotted and dashed lines in Fig. 5-3), the oxidation currents gradually diminish, which is attributable to the irreversible formation of a dendrimer coating on the ITO surface after the first scan.

Amine groups of the dendrimer-modified ITO surfaces were partially modified with ferrocenecarboxaldehyde, and the

resulting Schiff bases were reduced using NaBH_4 after the conjugation reaction (see section 5.2.3. for details). Fig. 5-4 shows the cyclic voltammograms of an Fc-D-modified (solid line) and bare ITO (dashed line) electrode obtained in 1 M NaClO_4 . The Fc-D-modified ITO electrode showed a reversible redox wave, which was not observed for the bare ITO electrode. It was also observed that the current linearly increased with scan rate over the range of 5~100 mV/s as expected for surface-confined electroactive species (Fig. 5-5 ~ 5-6).

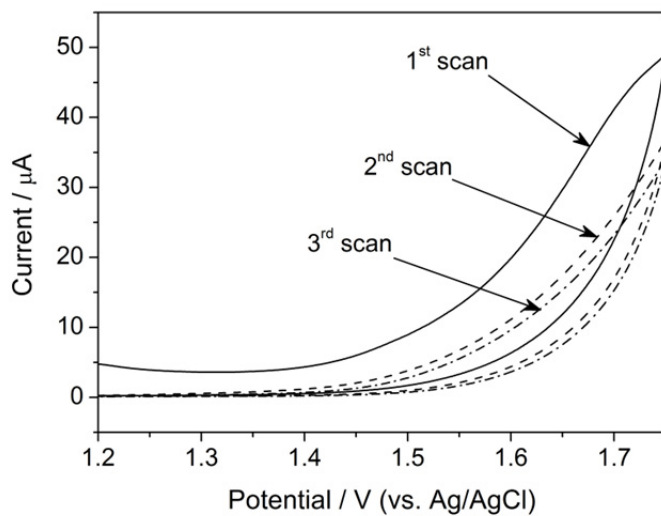


Fig. 5–3 Cyclic voltammograms obtained on ITO electrode in an aqueous 10 μM G6-NH₂ PAMAM dendrimer solution containing 0.1 M LiClO₄. Scan rate was 10 $\text{mV} \cdot \text{s}^{-1}$.

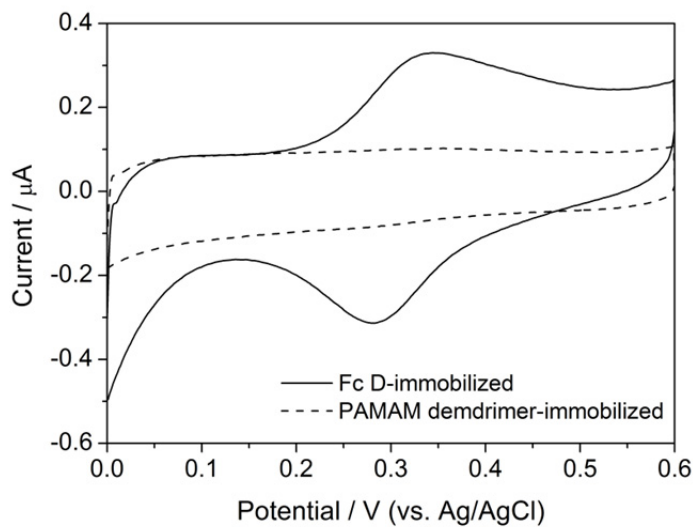


Fig. 5-4 Cyclic voltammograms of a Fc-D-modified (solid line) and a bare ITO (dashed line) electrode in 1 M NaClO_4 . Scan rate was $20 \text{ mV} \cdot \text{s}^{-1}$.

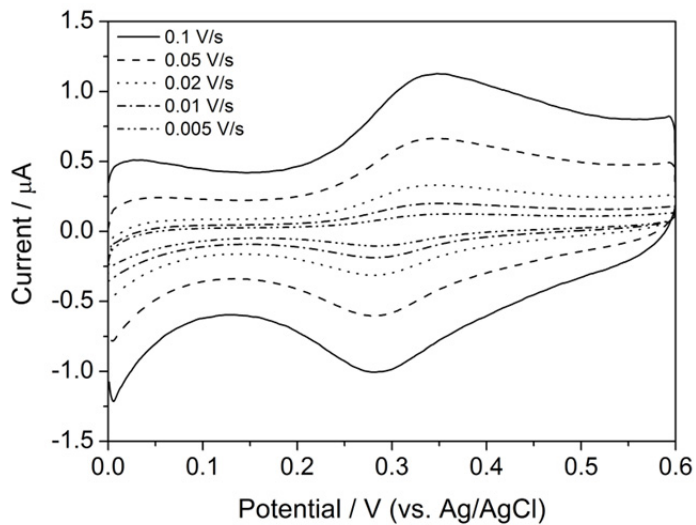


Fig. 5-5 Cyclic voltammograms of Fc-D-modified ITO electrode in 1 M NaClO_4 at scan rates from 5 to $100 \text{ mV} \cdot \text{s}^{-1}$.

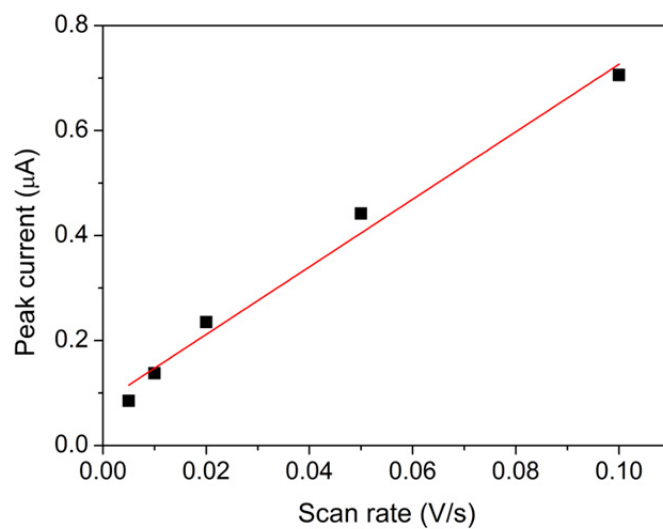


Fig. 5–6 Dependence of the oxidation peak current on the scan rates.

5.3.2. Immobilization of Pt DENs on ITO electrodes

The synthesized Pt DENs were then immobilized onto the ITO surfaces via electrooxidative grafting of the terminal amines of the dendrimers to the surfaces. Briefly, the potential of the ITO electrode was scanned five times between 1.2 and 1.8 V (*vs.* Ag/AgCl) in an aqueous 10 μ M Pt DEN solution containing 0.1 M LiClO₄. Fig. 5–7 shows the cyclic voltammograms obtained during the five consecutive scans; the voltammograms exhibit behavior characteristic of the electrooxidative grafting of amines. In the first scan (solid line in Fig. 5–7), an irreversible anodic wave appears at potentials larger than \sim 1.5 V, but the anodic currents dramatically diminish in subsequent scans. These observations suggested the electrochemical oxidation of the amine-terminated dendrimers encapsulating Pt nanoparticles followed by the irreversible formation of the Pt DEN film on the ITO surface.

After the electrooxidative grafting process, the resulting electrode was rinsed, ultrasonicated for 3 min, and then used for further electrochemical measurements to confirm the presence of Pt DENs grafted onto the ITO. Fig. 5–8 shows the cyclic voltammogram of a Pt DEN-grafted ITO electrode

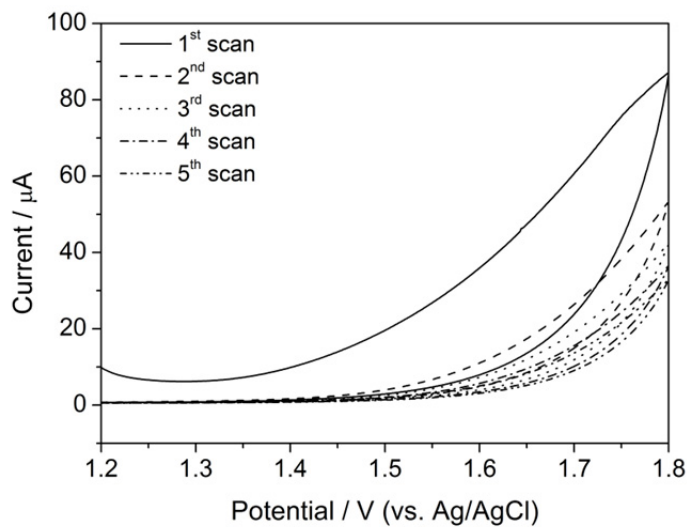


Fig. 5-7 Cyclic voltammograms obtained on ITO electrode in an aqueous 10 μM Pt DEN solution containing 0.1 M LiClO_4 . Scan rate was $10 \text{ mV} \cdot \text{s}^{-1}$.

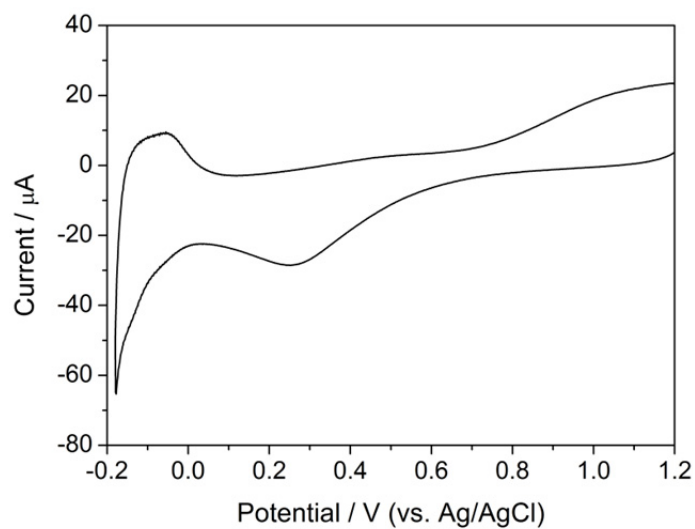


Fig. 5–8 Cyclic voltammogram of a Pt DEN-grafted ITO electrode in 0.5 M H_2SO_4 . Scan rate was $100 \text{ mV} \cdot \text{s}^{-1}$.

obtained in 0.5 M H₂SO₄. The Pt DEN-grafted ITO electrode showed characteristic redox waves observable on a Pt surface, *i.e.* redox peaks of Pt and hydrogen adsorption-desorption peaks.

5.3.3. Application of Fc-D and Pt DEN-grafted ITO electrodes to electrocatalysis

p-Aminophenyl phosphate (APP) is the most commonly used alkaline phosphatase (ALP) substrate. However, it is relatively unstable in aqueous solutions [30], and the electrooxidation of its ALP product, *p*-aminophenol (AP), on the surface of the ITO electrodes proceed slowly. In order to address this problem, Fc-D and Pt DENs, whose Fc moiety and encapsulated Pt nanoparticles acted as electron mediators, were immobilized onto the ITO surfaces. In this study, we tested the electrocatalytic activity of the ALP product such as AP using the different types of electrografted dendrimer films.

Prior to the electrochemical characterization of the two different types of immobilized dendrimer electrodes for AP, we first examined its electrochemical behavior in a conventional three-electrode system, a macroscopic ITO electrode. Fig. 5-

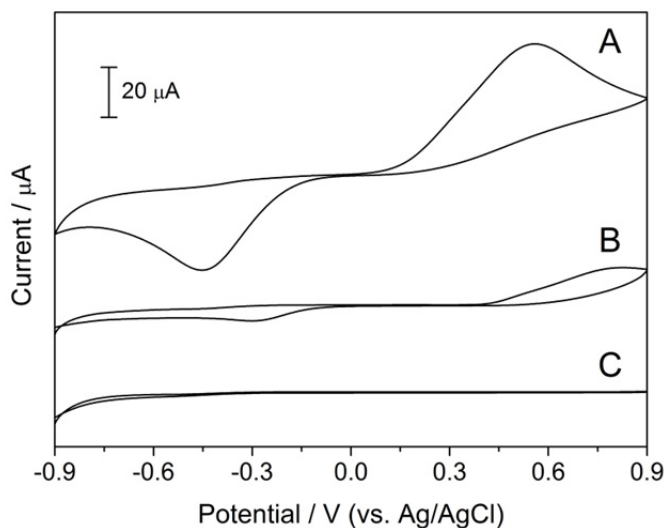


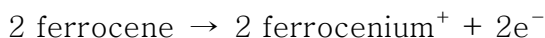
Fig. 5-9 Cyclic voltammograms obtained using a conventional, three-electrode electrochemical cell consisting of an ITO working electrode ($r = 3$ mm), a Ag/AgCl reference electrode, and a Pt counter electrode. The electrolyte solution contained 50 mM Tris buffer (pH 9.0), 10 mM MgCl_2 , and (A) 1 mM AP, (B) 5 mM APP, and (C) no redox-active couple. Scan rate was $50 \text{ mV} \cdot \text{s}^{-1}$.

9A shows a cyclic voltammogram obtained in a solution containing 50 mM Tris buffer (pH 9.0), 10 mM MgCl₂, and 1 mM AP. Compared to the nearly thermodynamically reversible behavior previously reported for AP on glassy carbon electrodes [31], AP voltammetry on ITO electrodes was far more sluggish. Nevertheless, the presence of both oxidation and reduction peaks indicates a quasireversible electron-transfer process [32], which suggests that a sufficient potential difference applied to the IDA electrode will result in redox recycling [33]. Fig. 5-9B compares the voltammetry of 5 mM APP to 1 mM AP (Fig. 5-9A) under identical electrochemical conditions. This comparison is important because, following a typical assay, the concentration of APP remains higher than that of AP. Accordingly, it is essential that the potential difference between the IDA electrodes be adequate to oxidize AP and reduce *p*-quinone imine (QI, oxidation product of AP) but not so extreme as to either oxidize or reduce APP. For completeness, Fig. 5-9C shows a cyclic voltammogram obtained under conditions identical to those used in parts A and B of Fig. 5-9 except in the absence of AP and APP. In the important potential region between -0.6 and +0.6 V, the

background current is very low. The relatively small cathodic current between -0.9 and -0.6 V probably arises from the kinetically slow proton reduction on ITO.

5.3.3.1. Electrocatalytic performance of Fc-D modified ITO electrode

To evaluate the electrocatalytic performance of the Fc-D-modified ITO electrode, we investigated the voltammetric responses to AP. In the presence of AP (solid line in Fig. 5-10), an irreversible peak appears near 0.3 V, indicating the redox-mediated oxidation of AP. The tethering of ferrocene to the dendrimer was employed to lower the overpotential of AP electrooxidation because the ITO electrodes show poor electrocatalytic activity for AP. The anodic peak potential negatively shifts from the oxidation potential of AP (0.6 V *vs.* Ag/AgCl) to that of the dendrimetric ferrocenyl groups (0.3 V *vs.* Ag/AgCl). This can be explained by the following mechanism:



where quinone imine (QI) is a molecule of AP, which has been oxidized by the loss of two electrons. When the potential scan was reversed, no cathodic peak corresponding to the reduction of QI was observed even in an extended negative potential sweep to -0.8 V. The oxidation reaction is thermodynamically favorable because the surface-immobilized ferrocenium is capable of oxidizing the solution-phase AP via a two-step mechanism. The reverse reaction, however, does not occur because it involves the thermodynamically unfavorable electron transfer from ferrocene to QI. The absence of a cathodic peak for QI reduction and the negative shift (which means less overpotential) of the anodic peak for AP oxidation strongly suggest that the AP oxidation occurs via the proposed redox reaction involving ferrocene. Features similar to the irreversible current reported herein have been previously described in other studies [34,35]. As a negative control, we obtained a cyclic voltammogram in the absence of AP. A low electrochemical response stemming from the Fc redox couple can be observed (dashed line in Fig. 5-10). We assumed that the low response was probably because of the redox reaction of

the surface-bound electroactive species at the surface of the Fc-D-modified electrode.

Encouraged by the electrocatalytic performance of the Fc-D-modified ITO electrode, the same experiments were carried out using a micropatterned IDA electrode. Fig. 5-11 shows the cyclic voltammograms of 1 mM AP at the bare IDA electrode compared to those for the Fc-D-modified IDA electrode. The generator and collector current values obtained at the Fc-D-modified IDA electrode (Fig. 5-11B) were higher than those obtained at the bare IDA electrode (Fig. 5-11A). These observations indicate that the electrooxidation of AP is significantly catalyzed by the tethering of the ferrocene inside the immobilized dendrimers. The symmetric current in the feedback mode of the Fc-D-modified IDA and bare IDA reveals that the collection efficiencies were 84.1 % and 90.4 %, respectively.

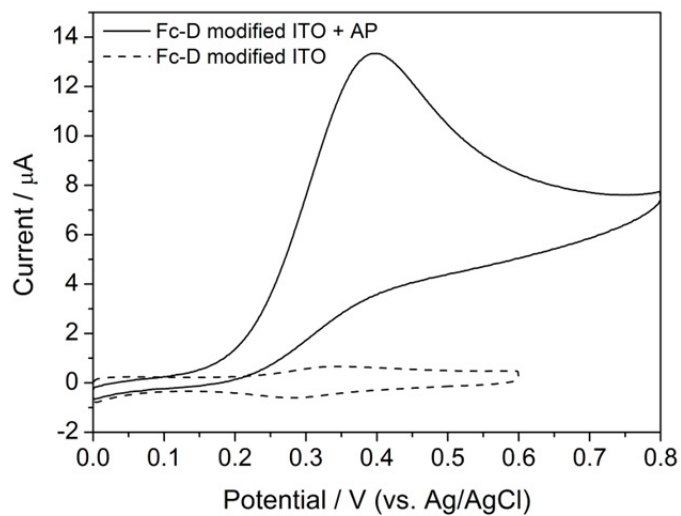


Fig. 5-10 Cyclic voltammograms of the Fc-D-modified ITO electrode in the absence and presence of 1 mM AP in a Tris buffer (pH 9.0) containing 10 mM MgCl_2 . Scan rate was 50 $\text{mV} \cdot \text{s}^{-1}$.

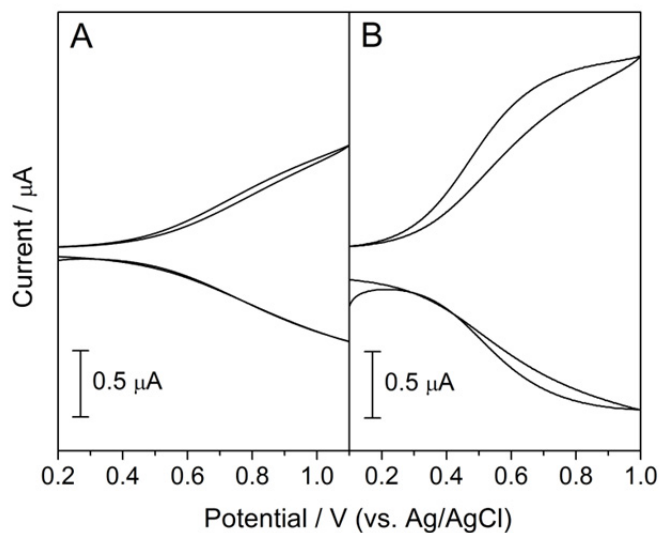


Fig. 5–11 Cyclic voltammograms of 1 mM AP obtained from the bare IDA (A) and the Fc–D–modified IDA electrode (B). The potential of generator electrodes of the bare IDA and the Fc–D–modified IDA electrode was swept and the potential of collector electrodes of the bare IDA and the Fc–D–modified IDA electrode was held at -0.8 and -0.6 V, respectively. Scan rate was $5 \text{ mV} \cdot \text{s}^{-1}$.

5.3.3.2. Electrocatalytic performance of Pt DEN-grafted electrode

After characterizing the Pt DEN-grafted ITO, we investigated the electrochemical features of the AP redox behavior on the Pt DEN-grafted ITO electrode. Fig. 5-12 shows the representative cyclic voltammograms of 1 mM AP in a Tris buffer (pH 9.0) containing 10 mM MgCl₂ on a Pt DEN-grafted and bare ITO electrode, respectively. The bare ITO electrode shows a significant peak potential difference ($\Delta E_p \approx 1.2$ V, solid line in Fig. 5-12) for the redox reaction of AP, while the Pt DEN-grafted ITO electrode shows a relatively small peak potential difference ($\Delta E_p \approx 0.55$ V, dashed line in Fig. 5-12). These results clearly demonstrate that the redox behavior of AP was electrocatalytically affected by the electronic mediation of the encapsulated Pt nanoparticles inside the dendrimers, leading to a drastic decrease in the ΔE_p value.

Fig. 5-13 shows the cyclic voltammograms in the absence and presence of 1 mM AP in Tris buffer (pH 9.0) containing 10 mM MgCl₂ on Pt DEN-grafted ITO electrodes at a scan rate of 50 mV · s⁻¹. In the absence of AP, a low background current in the important potential region between -0.4 and +0.4 V can be

observed (dashed line in Fig. 5-13). However, in the presence of AP, a reversible redox wave can be observed (solid line in Fig. 5-13), demonstrating successful electrocatalytic performance of the Pt DEN-grafted ITO electrodes. Both cathodic and anodic peaks are well defined, with a small peak potential difference compared to those for the bare ITO electrode.

To evaluate whether it was possible to amplify a response current using the Pt DEN-grafted IDA electrode, we measured the cyclic voltammograms of AP by using it as an ALP product. Fig. 5-14 shows the cyclic voltammograms of 1 mM AP at the Pt DEN-grafted IDA electrode compared to those of a bare IDA electrode. The current at the Pt DEN-grafted IDA (Fig. 5-14B) was about seven times higher than that at the bare IDA (Fig. 5-14A). The collection efficiencies, defined by the ratio of the collector current to the generator current, of the Pt DEN-grafted IDA and bare IDA electrode, were calculated as 92.7 % and 90.4%, respectively.

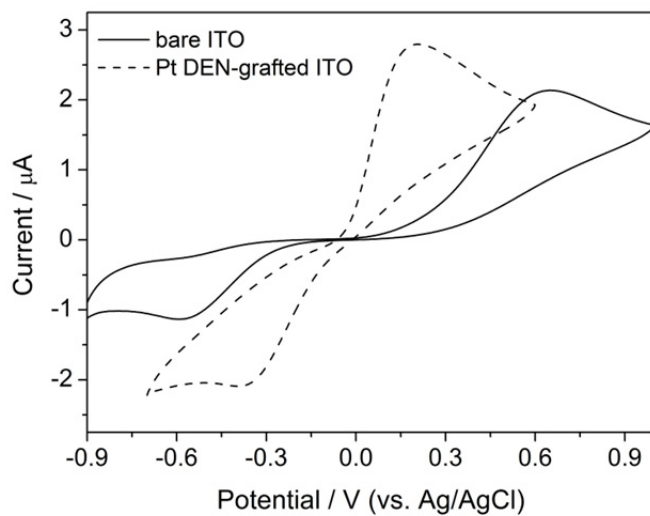


Fig. 5–12 Cyclic voltammograms of 1 mM AP obtained from the bare ITO electrode and the Pt DEN-grafted ITO electrode. Scan rate was $50 \text{ mV} \cdot \text{s}^{-1}$.

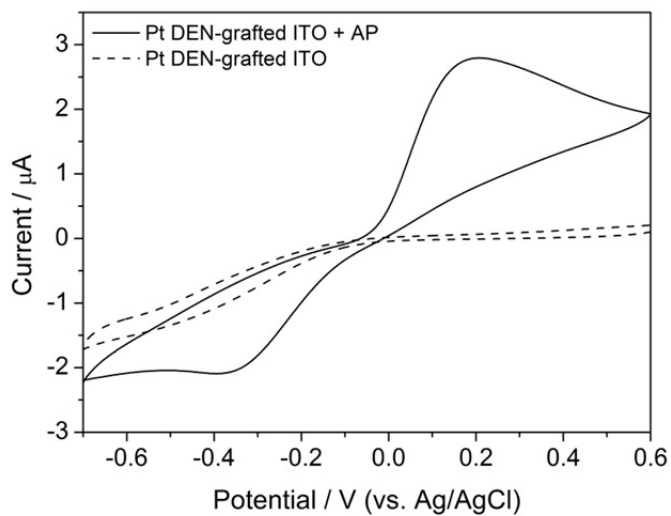


Fig. 5–13 Cyclic voltammograms of the Pt DEN-grafted ITO electrode in the absence and presence of 1 mM AP in a Tris buffer (pH 9.0) containing 10 mM MgCl_2 . Scan rate was 50 $\text{mV} \cdot \text{s}^{-1}$.

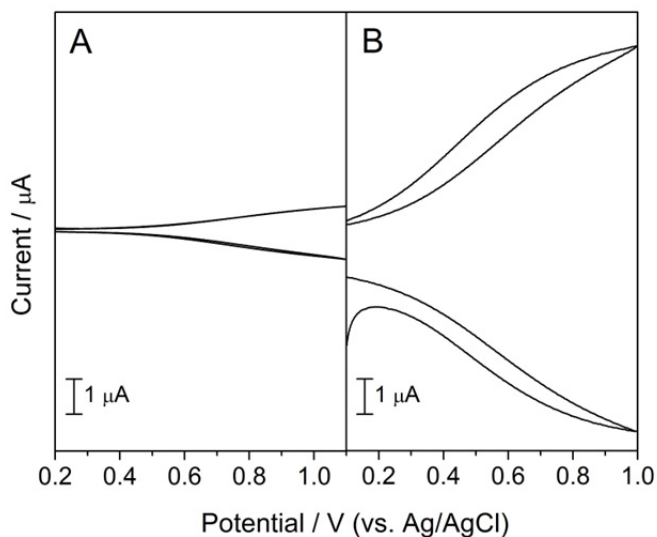


Fig. 5–14 Cyclic voltammograms of 1 mM AP obtained from the bare IDA (A) and the Pt DEN-grafted IDA electrode (B). The potential of generator electrodes of the bare IDA and the Pt DEN-grafted IDA electrode was swept and the potential of collector electrodes of the bare IDA and the Pt DEN-grafted IDA electrode was held at -0.8 and -0.6 V, respectively. Scan rate was $5 \text{ mV} \cdot \text{s}^{-1}$.

5.4. Conclusion

We have described a convenient method for the electrochemical grafting of ITO electrodes with amine-terminated PAMAM dendrimers. The electrooxidative grafting of dendrimers enabled the rapid modification of ITO surfaces with electroactive ferrocene or Pt nanoparticles, which were clearly confirmed through electrochemical measurements. Furthermore, the immobilized dendrimers were used as molecular carriers for partially tethered ferrocene moieties and encapsulating Pt nanoparticles, which showed electrocatalytic activity towards the *p*-aminophenol redox reaction. We envision that this approach will provide a general strategy for the surface functionalization of ITO with a variety of catalytic materials, which might be useful for a broad range of applications such as electrochemical sensors, optical electronics, energy conversion, and catalysis.

5.5. References

- [1] C. Simão, M. Mas–Torrent, N. Crivillers, V. Lloveras, J. M. Artés, P. Gorostiza, J. Veciana, C. Rovira, *Nat. Chem.* **2011**, *3*, 359.
- [2] J. Areephing, W. R. Browne, N. Katsonis, B. L. Feringa, *Chem. Commun.* **2006**, 3930.
- [3] C. Amatore, D. Genovese, E. Maisonhaute, N. Raouafi, B. Schollhorn, *Angew. Chem., Int. Ed.* **2008**, *47*, 5211.
- [4] J. Lahann, S. Mitragotri, T.–N. Tran, H. Kaido, J. Sundaram, I. S. Choi, S. Hoffer, G. A. Somorjai, R. Langer, *Science*, **2003**, *299*, 371.
- [5] B. Kim, J. M. Beebe, C. Olivier, S. Rigaut, D. Touchard, J. G. Kushmerick, X.–Y. Zhu, C. D. Frisbie, *J. Phys. Chem. C* **2007**, *111*, 7521.
- [6] I. Willner, *Science*, **2002**, *298*, 2407.
- [7] H. J. Choi, N. H. Kim, B. H. Chung, G. H. Seong, *Anal. Biochem.* **2005**, *347*, 60.
- [8] D. M. Adams, L. Brus, C. E. D. Chidsey, S. Creager, C. Creutz, C. R. Kagan, P. V. Kamat, M. Lieberman, S. Lindsay, R. A. Marcus, R. M. Metzger, M. E. Michel–Beyerle, J. R. Miller, M. D. Newton, D. R. Rolison, O. Sankey, K. S. Schanze, J. Yardley,

- X. Zhu, *J. Phys. Chem. B* **2003**, *107*, 6668.
- [9] J. J. Gooding, *Electroanalysis* **2008**, *20*, 573.
- [10] J. J. Gooding, S. Ciampi, *Chem. Soc. Rev.* **2011**, *40*, 2704.
- [11] C. J. Love, L. A. Estroff, J. K. Kriebel, R. G. Nuzzo, G. M. Whiteside, *Chem. Rev.* **2005**, *105*, 1103.
- [12] C. Vericat, M. E. Velam C. Benitez, P. Carro, R. C. Salvarezza, *Chem. Soc. Rev.* **2010**, *39*, 1805.
- [13] M. Kind, C. Wöll, *Progr. Surf. Sci.* **2009**, *84*, 230.
- [14] T. P. Sullivan, W. T. S. Huck, *Eur. J. Org. Chem.* **2003**, 17.
- [15] C. D. Bain, G. M. Whiteside, *J. Am. Chem. Soc.* **1989**, *111*, 7164.
- [16] J. P. Folkers, P. E. Laibinis, G. M. Whiteside, *Langmuir* **1992**, *8*, 1330.
- [17] S. J. Stranick, A. N. Parikh, Y. R. Tao, D. L. Allara, P. S. Weiss, *J. Phys. Chem.* **1994**, *98*, 7636.
- [18] K. Tamada, H. Akiyama, T. X. Wei, S. A. Kim, *Langmuir* **2003**, *19*, 2306.
- [19] A. J. Downard, *Electroanalysis* **2000**, *11*, 1085.
- [20] J. Pinson, F. Podvorica, *Chem. Soc. Rev.* **2005**, *34*, 429.
- [21] J. Pinson, D. Bélanger, *Chem. Soc. Rev.* **2011**, *40*, 3995.
- [22] S. Mahouche-Chergui, S. Gam-Derouich, C. Mangeney, M.

- H. Chehimi, *Chem. Soc. Rev.* **2011**, *40*, 4143.
- [23] A. L. Gui, G. Liu, M. Chockalingam, G. L. Saux, J. B. Harper, J. J. Gooding, *Electroanalysis* **2010**, *22*, 1283.
- [24] D. Astruc, E. Boisselier, C. Ornelas, *Chem. Rev.* **2010** *110*, 1857.
- [25] V. Balzani, P. Ceroni, A. Juris, M. Venturi, S. Campagna, F. Puntoriero, S. Serroni, *Coord. Chem. Rev.* **2001**, *219–221*, 545.
- [26] J. W. J. Knapen, A. W. van der Made, J. C. de Wilde, P. W. N. M. van Leeuwen, P. Wijkens, D. M. Grove, G. van Koten, *Nature* **1994**, *372*, 659.
- [27] G. R. Newkome, C. Shreiner, *Chem. Rev.* **2010** *110*, 6338.
- [28] D. Astruc, *C. R. Acad. Sci. II B* **1996**, *322*, 757.
- [29] A. Andronov, J. M. J. Fréchet, *Chem. Commun.* **2000**, 1701.
- [30] M. S. Wilson, R. D. Rauh, *Biosens. Bioelectron.* **2004**, *20*, 276.
- [31] I. Rosen, J. Rishpon, *J. Electroanal. Chem.* **1989**, *258*, 27.
- [32] A. J. Bard, L. R. Faulkner, *Electrochemical methods, Fundamentals and Applications*, 2nd ed., Wiley New York, **2001**.
- [33] O. Niwa, M. Morita, H. Tabei, *Anal. Chem.* **1990**, *62*, 447.
- [34] S.-K. Oh, L. A. Baker, R. M. Crooks, *Langmuir* **2002**, *18*, 6981.

[35] K. S. Alleman, K. Weber, S. E. Creager, *J. Phys. Chem.*
1996, *100*, 17050.

6. A Novel Three-Electrode System Microfabricated onto ITO for On-Chip Electrochemical Detection

6.1. Introduction

Recently, there has been growing interest in the development of miniaturized sensors for biomedical and environmental applications; for instance, monitoring biologically significant analytes and environmental conditions such as pH, physiological markers such as oxygen and carbon dioxide content in blood, as well as detection of pathogenic bacteria and viruses. This interest has been in response to the increasing need to prevent outbreaks and cross contamination in the global food supply and processing chains, maintain of a safe drinking water supply, as well as in medical settings where a patient's physiological condition needs to be monitored on a real-time basis.

Although a wide array of biosensors based on optical, electrical, piezoelectric, resonant and thermal transduction exists for biomedical and environmental applications, electrochemical biosensors are the simplest, low-cost, reliable, and practical sensors [1–4]. Electrochemical biosensors for

biomedical and environmental applications have been developed by employing various fabrication methods such as photolithography, screen-printing, and ink-jet printing. In all these biosensors, the electrochemical transducer, which converts the quantity and type of chemical/biological analyte into a distinct electrical signal, is the most important component. Typically, the transduction results in either a change in voltage at an electrode interface or flow of charge when the potential of the electrode is maintained constant relative to the solution. A crucial component, which measures and controls the solution side potential, is the reference electrode. The reference potential set by the reference electrode must be insensitive to any changes occurring in the electrolyte solution and maintain a constant potential throughout the analysis. The current trend towards miniaturization of biosensors for speed, performance, and portability has meant miniaturization of not just the sensing element, but also the reference electrode.

The miniaturization of the reference electrode has several implications, which require considerable attention. All components of the electrode such as metal, salt, filling solutions, and interfaces need to be miniaturized. Factors such as

potential drift, liquid junction effects, and solution concentrations are significant factors that can easily interfere with the results; therefore, they need to be controlled [5]. Thus, in constructing such electrodes, there are several factors which must be taken into account: (i) reference electrodes must have high exchange current densities, and thus be nonpolarizable (hard to change the electrode's potential); (ii) potentials of all the electrodes must be reproducible; (iii) potential drift of the electrodes, from factors attributed to filling solution effusion or degradation of electrode coating, must be minimized over the duration of device operation; and (iv) other operational requirements needed for the working electrodes might be imposed based on the nature of the experiment. For example, invasive recording and stimulating electrodes should not introduce foreign toxic ions into humans, which necessitate the use of highly polarizable electrodes.

The reference electrode has a pronounced influence on the accuracy of measurements made with such biosensors, whether they are electrochemical sensors, biological field effect transistors (bio-FET) [6,7], or bio-impedances probes [8,9] because it is present in almost all types of biosensors, and

plays an equally important role in ensuring proper device operation and reliability of the results. Evidently, in order to facilitate the development and successful operation of an array of miniaturized sensors, it is vital to fabricate functional and robust miniaturized reference electrodes.

Reportedly, the extremely large surface area of np Pt offers the benefit of very low polarizability (*i.e.* high exchange current density, i_0) in the electrochemical reaction as expressed by the following equation (1) [10].



In response to changes in pH of a sample solution, nanoporous Pt (np Pt) is a promising pH-indicating electrode, which exhibits near-Nernstian behavior with ignorable hysteresis, short response time, and high precision [10]. To suppress the interference from redox couples, dense nonconducting polymers such as polyphenol is useful for protecting np Pt by preventing most redox couples and allowing only small species such as hydrogen ion or hydrogen peroxide to permeate [10]. More interestingly, the np Pt might behave like an ideal reference electrode under a fixed pH condition [11]. It should be noted that such functional benefits of np Pt

stem solely from geometrical nanoscale tailoring, involving no chemical modification. The principle underlying such outstanding non-polarizability of nanoporous electrodes is not clear for now. Nevertheless, the enhanced interaction between the electrode surface and hydrogen ions in the highly confined porous structure was previously suggested as a plausible reason [11].

In this part, the fabrication and characterization of solid-state reference electrodes on indium tin oxide (ITO) micropatterns are described. The aim of this work was to optimize and evaluate the performance of mechanically robust, and easy to manufacture reference electrodes. For this purpose, the np Pt with a poly-1,3-phenylenediamine (poly-*m*-PD) film on the ITO surface was easy to produce and particularly compatible with microfabrication. The experimental results in this study demonstrate that the proposed system successfully works as a solid-state reference electrode, which can be integrated into microchips for microanalysis systems.

6.2. Experimental

6.2.1. Chemicals and materials

All reagents were used as received without further purification. Hydrogen hexachloroplatinate hydrate was purchased from Kojima Chemicals Co., Ltd. (Kashiwabara, Japan). 1,1'-ferrocenedimethanol, toluene, 1,3-phenylenediamine (*m*-PD), and *t*-octylphenoxy polyethoxyethanol (Triton[®] X-100) were purchased from Sigma-Aldrich (St. Louis, MO, USA). N-(6-aminohexyl)aminomethyltriethoxysilane (AHAMTES) was obtained from Gelest (Morrisville, PA, USA). Hexamethyldisilazane (HMDS), sulfuric acid, ethanol, and acetone were received from J. T. Baker (Phillipsburg, NJ, USA). Sodium chloride was received from Daejung (Siheung, Korea). Phosphate buffered saline (PBS, pH 7.4) solution consisted of 10 mM phosphate and 0.1 M NaCl. 18 M Ω ·cm deionized (DI) water was used to prepare all aqueous solutions (Barnstead NANOpure[®], Thermo Scientific Inc., USA).

6.2.2. Micropatterning of ITO-coated glass substrates

ITO-coated glass slides (75 mm \times 25 mm, 1.1 mm thick,

Sigma–Aldrich, USA) were used as substrates. An ITO–coated glass slide was sequentially cleaned with ethanol, acetone, and DI water sequentially. After removing the moisture on the surface with an air blower, the cleaned ITO substrate was dehydrated on a hot plate at 120°C for 3 min and then cooled to room temperature. The substrate was spin–coated (YS–100MD, Won Corp., Korea) with HMDS at 7000 rpm for 30 s. The HMDS–coated substrate was placed on a hot plate at 120 °C for 90 s and subsequently cooled at room temperature. Afterwards, the photoresist (PR; AZ4620, Clariant, USA) coated the surface of the substrate using a spin coater at 7000 rpm for 30 s. After soft baking the PR–coated substrate at 100 °C for 90 s, the substrate was cooled at room temperature for 90 s immediately. Then, the substrate was aligned under a pattern–designed mask, and exposed to UV light (365 nm) for 11 s with a UV aligner (MDE–4000, Midas, Korea). The UV–exposed substrate was immersed into the AZ400K developer (Clariant, USA) for developing UV–exposed PR. The substrate was then washed with DI water and dried in clean air. Next, the substrate was hard–baked on a hot plate at 120°C for 15 min. After cooling at room temperature, the PR–patterned ITO substrate

was etched with an etchant solution (TE-100, Transene Company, Inc., USA) at 60°C for 13 min, which resulted in formation of ITO microelectrodes. All photoresist residues were removed by rinsing the ITO microelectrodes with acetone using an ultrasonic cleaner (3510E-DTH, Branson, USA) for 2 min. The part of working electrode consisted of 25 pairs of microbands. The band length was 2 mm and the width was 5 μm , and the gap was 10 μm . Thus, the band length is equal to the channel width. The band width of parts of reference and counter electrode was 100 μm and 1 mm, respectively. An optical microscope image of the ITO micropatterns is shown in Fig. 6-1.

6.2.3. Fabrication of integrated three-electrode system

To form counter and reference electrodes on a glass substrate with ITO micropatterns, Pt and np Pt with a poly-*m*-PD film were selectively deposited onto the ITO micropatterns. The pretreated ITO micropatterns were immersed in 20 mL of anhydrous toluene containing 0.5 mL AHAMTES for 24 h at room temperature to allow the formation of a amine-terminated organic monolayer on the ITO surface. The substrates were

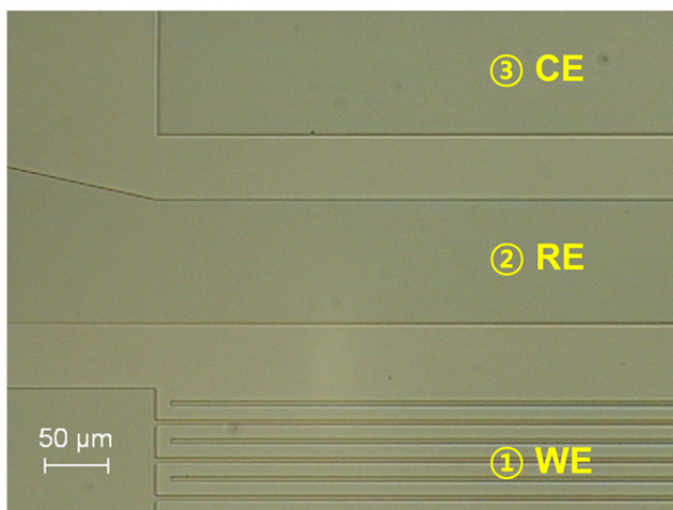


Fig. 6-1 An optical microscope image of ITO micropatterns obtained during microfabrication. The microscope image was obtained with unmodified three parts of ITO micropatterns (WE = working electrode, RE = reference electrode, CE = counter electrode).

removed from the solution, rinsed with toluene, and sonicated in toluene for 3 min. Next, the substrates were cured on a hot plate at 120°C for 30 min to promote the condensation of hydrogen-bonded silanols and form siloxane bonds, and convert ammonium ions to the neutral and more reactive amine groups [12].

To obtain a robust Pt layer, a Cr film was deposited prior to the formation of the Pt layer. A Cr layer was electrodeposited on a part of the counter electrode by applying -1.0 V for 200 s in an aqueous solution of 10 mM $\text{CrCl}_3 \cdot 6\text{H}_2\text{O}$. Then, a Pt layer was deposited by applying -0.2 V for 800 s in an aqueous solution of 10 mM $\text{H}_2\text{PtCl}_6 \cdot 6\text{H}_2\text{O}$.

The np Pt, denoted as L_2 -ePt, was prepared by electroplating Pt in a reverse micelle solution, as described in our previous study [13]. Hydrogen hexachloroplatinate hydrate (5 wt%), 0.3 M sodium chloride (45 wt%), and Triton X-100 (50 wt%) were mixed and heated to 60°C. The mixture, as made, was transparent and homogeneous. The temperature of the mixture solution was maintained around 60°C using an oven (WOF-050, Daihan Scientific Co., Ltd.). L_2 -ePt was electrochemically deposited onto the ITO surface a part of the reference at -0.16

V vs. Ag/AgCl to minimize the crack [14]. The resulting L₂-ePt electrode was kept in distilled water for one day to extract the Triton X-100, and this procedure was repeated 4 to 5 times. Afterwards, a thin poly-*m*-PD layer was electropolymerized onto the L₂-ePt surface through four cyclic scans of potential between 0.2 and 1.0 V at a scan rate 4 mV · s⁻¹ in a PBS (pH 7.4) solution containing 10 mM *m*-PD.

6.2.4. Electrochemical measurements

All electrochemical measurements were performed with a CH Instruments (Austin, TX, USA) model 750A electrochemical analyzer. A conventional three-electrode cell assembly was employed throughout the experiments, which involved a working ITO electrode, a platinum wire counter electrode, and an Ag/AgCl reference electrode (RE-6, BASi, Stareton, UK). All potentials are reported versus Ag/AgCl reference at room temperature.

6.3. Results and Discussion

6.3.1. Fabrication of a Pt counter electrode on an ITO surface for a microchip

The Pt film could be directly electrodeposited onto the ITO surface. However, such a Pt film is easily removed during the washing process or chemical treatment because Pt adhesion onto the ITO surface is not strong. Even a thick film, electrodeposited for more than 2000 s, could be readily stripped off. Instead, a Cr film was used as the adhesion layer because Cr is widely used as a stable adhesion layer between metal and metal oxide [15,16]. The two main parameters involved in the electrochemical deposition of Cr onto the ITO surface, namely, applied voltage and electrodeposition time, were optimized and characterized. In preliminary experiments, linear sweep voltammetry was employed to confirm the electroreduction of Cr^{3+} to Cr^0 . Fig. 6-2 shows the linear sweep voltammogram of an ITO electrode modified AHAMTES in 10 mM $\text{CrCl}_3 \cdot 6\text{H}_2\text{O}$ at a scan rate of $0.1 \text{ V} \cdot \text{s}^{-1}$. The characteristic single reduction peak observed at -0.85 V can be attributed to the reduction of Cr^{3+} ions. The electrochemical deposition was carried out at -1.0 V for 100, 200, and 300 s in

10 mM $\text{CrCl}_3 \cdot 6\text{H}_2\text{O}$. As seen in Fig. 6-3, a deposition time of 200 s was optimal for both Cr film quality and electric conductivity.

After a Cr film was electrodeposited at -1.0 V for 200 s on the pretreated ITO electrode, a Pt film was deposited on the Cr/AHAMTES/ITO electrode. Fig. 6-4 shows the linear sweep voltammogram of the ITO electrode measured at a scan rate of $0.1 \text{ V} \cdot \text{s}^{-1}$ in 10 mM $\text{H}_2\text{PtCl}_6 \cdot 6\text{H}_2\text{O}$. The electrochemical reduction of Pt^{4+} ions starts from $+0.2$ V *vs.* Ag/AgCl and multiple cathodic peaks over the range of *ca.* -0.1 to -0.4 V are observed. Pt electrodeposited on the counter electrode at -0.2 V for 500 s exhibits a rather flat film surface with few cracks (Fig. 6-5A). The optical microscope image in Fig. 6-5B shows the Pt electrodeposited at -0.3 V for 500 s on the counter electrode. The Pt/Cr/AHAMTES/ITO electrode surface was of poor quality and the cracks were so deep that they reached the substrate surface. In contrast, a Pt film was electrodeposited at -0.2 V for 800 s on the Cr/AHAMTES/ITO part of the counter electrode (Fig. 6-5C). The resulting Pt/Cr/AHAMTES/ITO electrode shows very good uniformity and adhesion stability. Therefore, the optimal potential is a

compromise between that required for uniformity and that required for time efficiency in the electrodeposition of metal films.

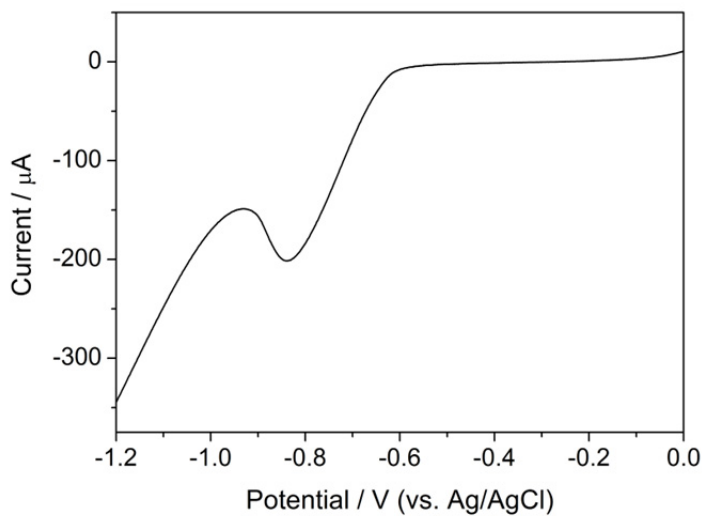


Fig. 6–2 Linear sweep voltammograms of 10 mM $\text{CrCl}_3 \cdot 6\text{H}_2\text{O}$ (scan rate $0.1 \text{ V} \cdot \text{s}^{-1}$) at the ITO electrode.

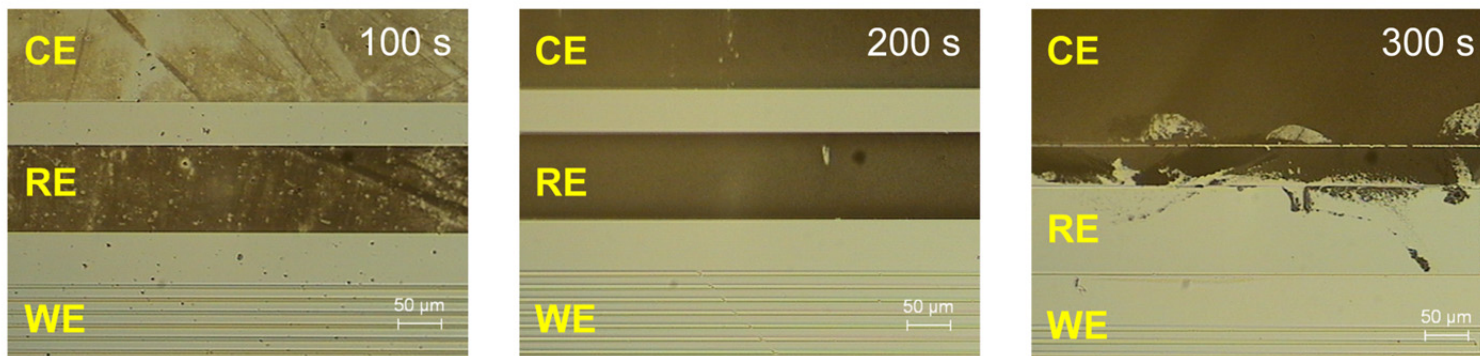


Fig. 6-3 Optical microscope images of ITO micropatterns after Cr electrodeposition with different deposition time.

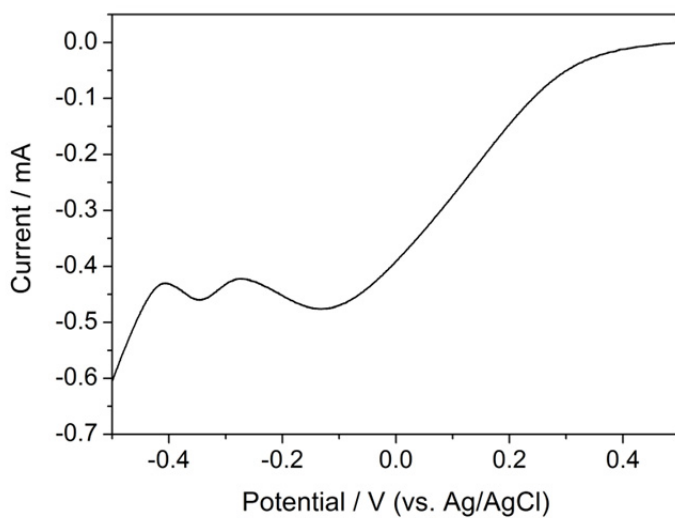


Fig. 6-4 Linear sweep voltammograms of 10 mM $\text{H}_2\text{PtCl}_6 \cdot 6\text{H}_2\text{O}$ (scan rate $0.1 \text{ V} \cdot \text{s}^{-1}$) at the ITO electrode.

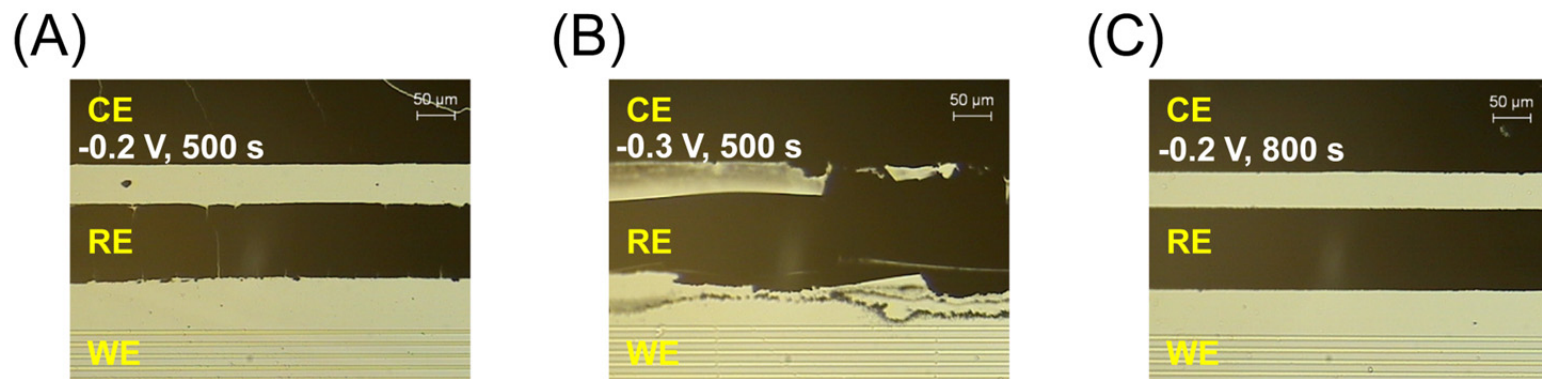


Fig. 6–5 Optical microscope images of ITO micropatterns after Pt electrodeposition with various conditions of applying voltage and deposition time.

6.3.2. Fabrication of the solid-state reference electrode for the microchip using L₂-ePt

To obtain L₂-ePt deposited electrodes, the AHAMTES modified ITO surface on part of the reference electrode was exposed to the solution of hydrogen hexachloroplatinate hydrate (5 wt%) + 0.3 M NaCl (45 wt%) + Triton X-100 (50 wt%) at around 60°C (see experimental section 6.2.3 for details), and the potential applied to the ITO electrode was -0.16 V *vs.* Ag/AgCl to minimize the cracks [14]. Fig. 6-6 shows an optical microscope image of the L₂-ePt film electrochemically deposited for ~ 2500 s onto the patterned ITO electrode on part of the reference electrode. The L₂-ePt film electrodeposited for ~ 2500 s exhibits an excess of L₂-ePt grains deposited at the edge of the reference electrode and deep cracks shaped like a flash of lightning. On the other hand, a reduced electrodeposition time, *e.g.* 500 s, leads to a smooth and uniform film morphology with diminished cracking (Fig. 6-7).

The poly-*m*-PD layer was electropolymerized on top of the L₂-ePt film by potential cycling four times between 0.2 and 1.0 V (*vs.* Ag/AgCl) at 4 mV · s⁻¹. The thickness of the layer was

self-controlled to be *ca.* 50 nm, as previously described [17,18]. Although the poly-*m*-PD layer was thin, it was so dense that only molecules as small as hydrogen peroxide could permeate. It is known that poly-*m*-PD rejects relatively large redox species with a strong ionic field while allowing protons and hydronium ions to transit. Fig. 6-8 shows the cyclic voltammograms obtained during the four consecutive cyclings; the voltammograms exhibited behavior characteristic of the electropolymerization of poly-*m*-PD. In the first scan (solid line in Fig. 6-8), an irreversible anodic wave appears at potentials larger than ~ 0.4 V but the anodic currents dramatically diminish in subsequent scans (dashed, dotted, and dashed-dotted lines in Fig. 6-8). The initial electrochemical oxidation let the poly-*m*-PD anchor onto the L₂-ePt surface and inhibited further oxidation.

In order to check the stability of a poly-*m*-PD-coated L₂-ePt electrode, the open circuit potential of the fabricated solid-state reference electrode was measured. The L₂-ePt coated with poly-*m*-PD also shows a stable potential average of 0.365 V (Fig. 6-9). This result shows that the fabricated poly-*m*-PD/L₂-ePt reference electrode is stable enough to be used as a

reference electrode in an electrochemical sensing platform.

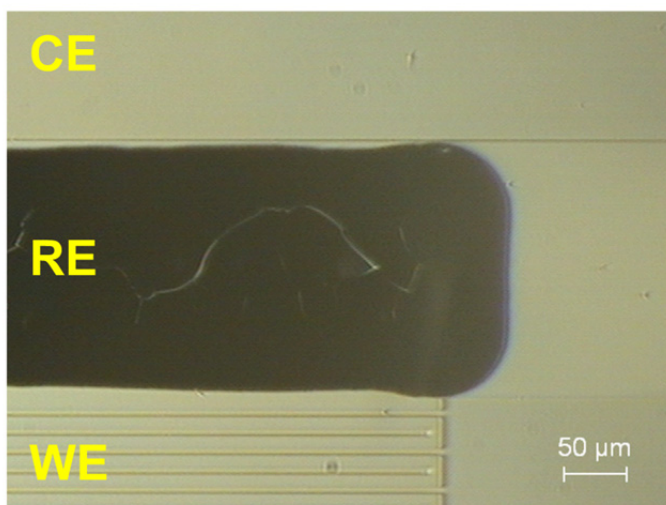


Fig. 6-6 An optical microscope image of ITO micropatterns after L_2 -ePt electrodeposited for 2500 s.

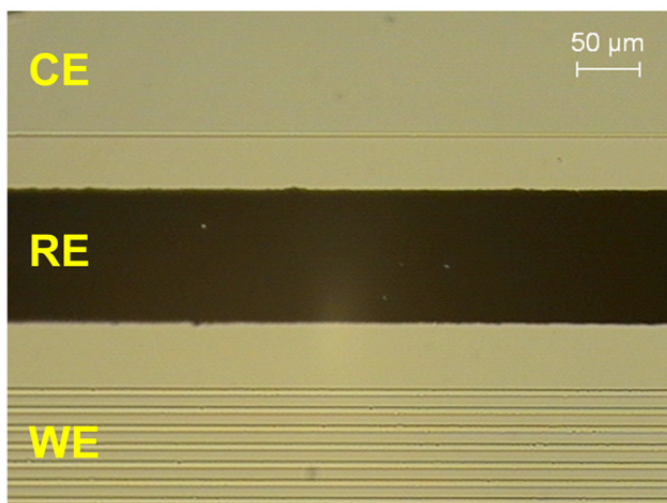


Fig. 6-7 An optical microscope image of ITO micropatterns after L_2 -ePt electrodeposited for 500 s.

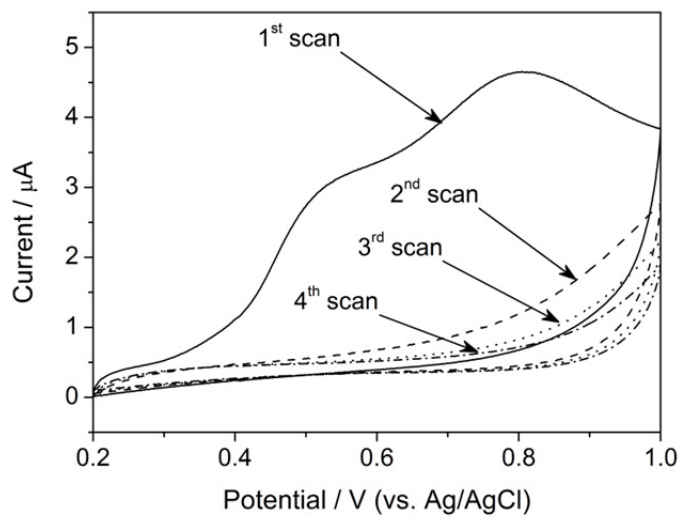


Fig. 6–8 Cyclic voltammograms obtained on $\text{L}_2\text{-ePt/ITO}$ surface in 10 mM *m*-PD solution containing 10 mM PBS (pH 7.4) solution. Scan rate was $4 \text{ mV} \cdot \text{s}^{-1}$.

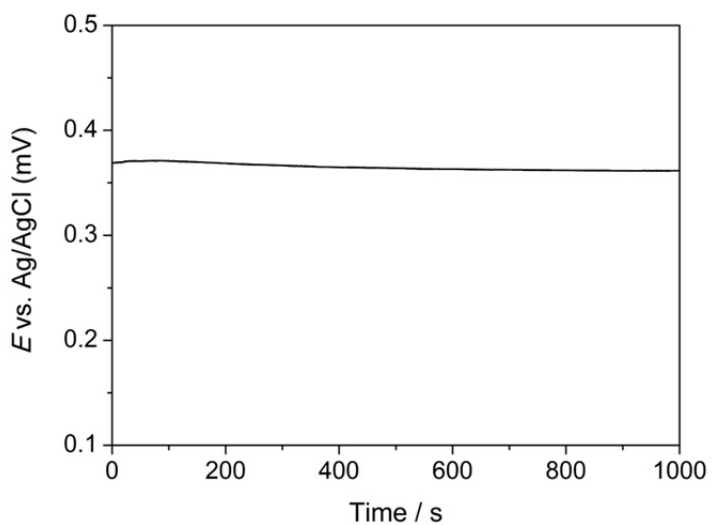


Fig. 6-9 Open circuit potential of poly-*m*-PD/L₂-ePt electrode measured in 10 mM PBS solution at pH 7.4.

6.3.3. Application for microchip with integrated three-electrode system

Embedding the poly-*m*-PD/L₂-ePt reference electrode in miniaturized systems is one of the most interesting examples of the application of solid-state reference electrodes. For demonstration purposes, an electrochemical microcell based on poly-*m*-PD/L₂-ePt was integrated into the microchip (Fig. 6-10). The electrochemical microcell contains three electrodes parts, which involve a working ITO IDA electrode, an electrodeposited Pt counter electrode, and a poly-*m*-PD/L₂-ePt as the solid-state reference electrode.

In order to probe the performance of poly-*m*-PD/L₂-ePt as the reference electrode, the results of the voltammetric measurements using poly-*m*-PD/L₂-ePt were compared with those obtained using an Ag/AgCl reference electrode. The cyclic voltammograms recorded with Ag/AgCl and poly-*m*-PD/L₂-ePt had identical shapes as demonstrated in Fig. 6-11 ~ 6-12.

Fig. 6-11 shows the cyclic voltammograms of 1 mM ferrocenedimethanol (Fc(MeOH)₂) in 2 M KCl as supporting electrolyte on ITO IDA as the working electrode. The generator

and collector electrodes of the IDA electrode were electrically tied to apply the same potential to both of them; actually, a single electrode (non-feedback mode). The cyclic voltammograms show behavior typical of a faradaic reaction that was limited by unidirectional diffusion. On the other hand, the cyclic voltammogram in Fig. 6-12 was acquired by scanning the potential of the generator electrode on the IDA electrode while the potential of the collector electrodes was constant (feedback mode). These data unambiguously reveal the usefulness of poly-*m*-PD/L₂-ePt as a solid-state reference electrode for electrochemical applications in microanalysis systems.

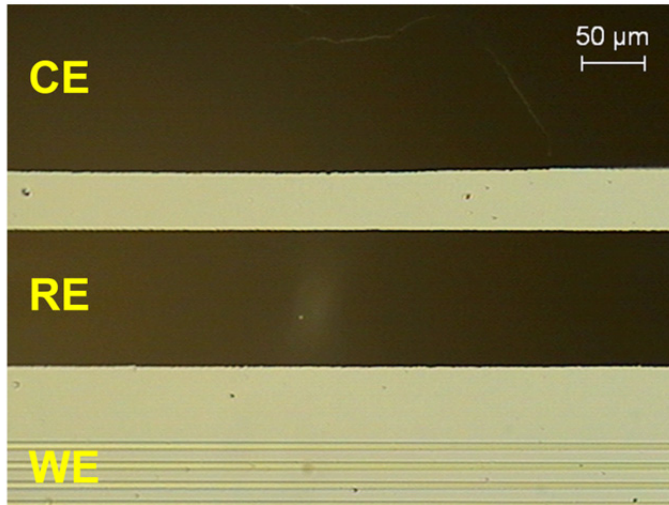


Fig. 6–10 An optical microscope image of ITO micropatterns obtained during microfabrication of the integrated three-electrode system.

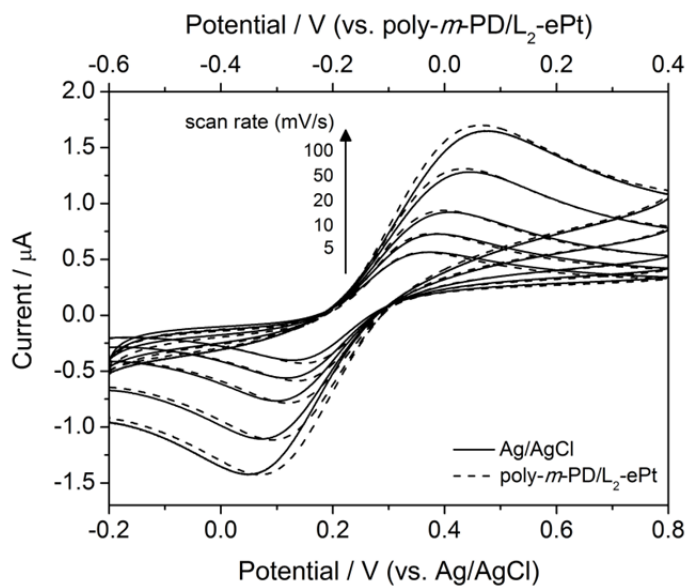


Fig. 6–11 Cyclic voltammograms obtained in 1 mM $\text{Fc}(\text{MeOH})_2$ containing 2 M KCl, using a ITO as a working electrode and Pt electrodeposited on ITO surface as a counter electrode and Ag/AgCl (solid line) or $\text{poly-}m\text{-PD/L}_2\text{-ePt}$ (dotted line) as a reference electrode.

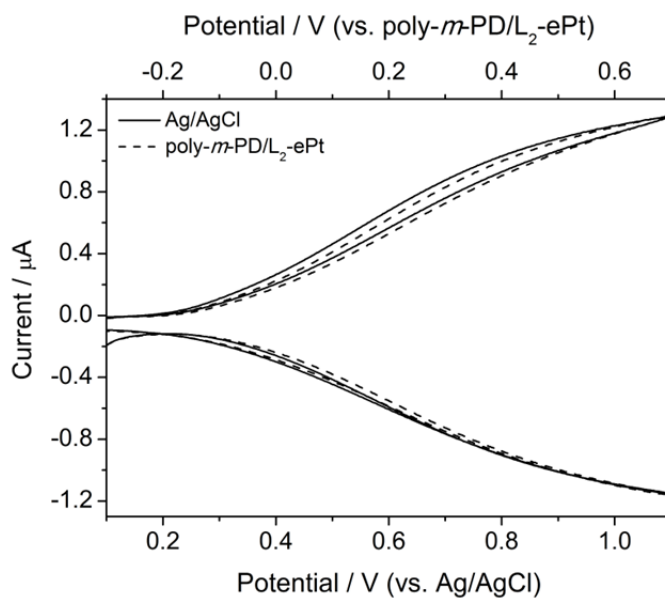


Fig. 6–12 Cyclic voltammograms obtained in 1 mM $\text{Fc}(\text{MeOH})_2$ containing 2 M KCl, using a ITO IDA electrode as a working electrode and Pt electrodeposited on ITO surface as a counter electrode and Ag/AgCl (solid line) or poly-*m*-PD/L₂-ePt (dotted line) as a reference electrode. Scan rate was 5 $\text{mV} \cdot \text{s}^{-1}$.

6.4. Conclusion

In this chapter, we demonstrated a reliable three-electrode system fabricated on ITO micropatterns. The parameters concerning the fabrication of counter and reference electrodes were optimized. The analytical performance of the three-electrode system involving the microchip was successfully demonstrated through the analysis of the electroactive species in the microchannel. The advantages of the three-electrode system include ease of chip fabrication, compatibility with a variety of substrate materials, ability of either static or dynamic electrochemical measurements as well as good electroanalytical performance. Furthermore, the design is well suited for application as an electrochemical detector for either flow injection analysis (FIA) or high performance liquid chromatography (HPLC).

The poly-*m*-PD/L₂-ePt system provides several valuable opportunities for various electrochemical applications; for example, chemical/biosensors and micro total analysis systems. It is easy to make, and fabricates reproducible products in a short duration, thus favoring mass production. Moreover, poly-*m*-PD/L₂-ePt can be patterned on a small scale, even

micrometers, because its fabrication procedure is based on electrodeposition, which takes place only on the electrode pattern. Apparently, miniaturized electrochemical systems such as the electrochemical detection units when integrated into the microfluidic chips will add several targets by introducing the poly-*m*-PD/L₂-ePt system.

6.5. References

- [1] H. Suzuki, *Electroanalysis* **2000**, *12*, 703.
- [2] N. Ravindra, M. C. Prodan, S. Fnu, I. Padron, S. K. Sikha, *JOM* **2007**, *59*, 37.
- [3] H. Suzuki, *Mater. Sci. Eng. C* **2000**, *12*, 55.
- [4] M. Koudelka–Hep, P. van der Wal, *Electrochim. Acta* **2000**, *45*, 2437.
- [5] D. P. Brezinski, *The Analyst* **1983**, *108*, 425.
- [6] F. Sevilla III, T. Kullick, T. Scheper, *Biosens. Bioelectron.* **1994**, *9*, 275.
- [7] M. W. Shinwari, M. J. Deen, D. Landheer, *Microelectron. Reliab.* **2007**, *47*, 2025.
- [8] H. Benjamin, S. Bhansali, S. B. Hoath, W. L. Pickens, R. Smallwood, *Sens. Actuat. B* **2005**, *111*, 430.
- [9] Y. Y. Duan, R. E. Millard, M. Tykocinski, X. Lui, G. M. Clark, R. Cowan, *Proc. SPIE* **2001**, *4235*, 145.
- [10] S. Park, H. Boo, Y. Kim, J.–H. Han, H. C. Kim, T. D. Chung, *Anal. Chem.* **2005**, *77*, 7695.
- [11] J.–H. Han, S. Park, H. Boo, H. C. Kim, J. Nho, T. D. Chung, *Electroanalysis* **2007**, *19*, 786.
- [12] J. Kim, G. J. Holinga, G. A. Somorjai, *Langmuir* **2011**, *27*,

5171.

[13] S. Park, S. Y. Lee, H. Boo, H.-M. Kim, K.-B. Kim, H. C. Kim, Y. J. Song, T. D. Chung, *Chem. Mater.* **2007**, *19*, 3373.

[14] S. Park, Y. J. Song, J.-H. Han, H. Boo, T. D. Chung, *Electrochim. Acta* **2010**, *55*, 2029.

[15] B. J. Polk, A. S. Stelzenmuller, G. Mijares, W. MacCrehan, M. Gaitan, *Sens. Actuators B* **2006**, *114*, 239.

[16] E. W. H. Jager, E. Smela, O. Inganäs, *Science* **2000**, *290*, 1540.

[17] R.-A. Jeong, J. Y. Hwang, S. Joo, T. D. Chung, S. Park, S. K. Kang, W.-Y. Lee, H. C. Kim, *Biosens. Bioelectron.* **2003**, *19*, 313.

[18] T. D. Chung, R.-A. Jeong, S. K. Kang, H. C. Kim, *Biosens. Bioelectron.* **2001**, *16*, 1079.

7. Summary

This dissertation presents a study of the development of practical sensors for the detection and quantification of analytes in environmental and biological samples. Although the sensors use a broad range of different chemistries, they all depend on the solid electrode surface and interactions with the target and molecular recognition layer. We focused on the improvement of analytical performance in chemical/bio sensors based on signal amplification strategies for highly sensitive detection. New methods such as the electrokinetic preconcentration on a microfluidic chip for small-molecule immunoassays and redox cycling in the 3D IDA device, present possibilities for signal amplification. We introduced additional methods to enhance the sensitivity, such as SERS-based techniques for sensitive detection over a range of heterogeneous assay methodologies. In addition, this dissertation also describes the importance of the precise control over the delicate interplay among surface nano-architectures, surface functionalization and chosen sensor transducer principle, as well as the usefulness of miniaturized lab-on-chip devices by the microfabrication of the integrated three-electrode system on microchips for

electrochemical detection.

In the first chapter, we highlighted the interesting behavior of SERS using oligonucleotides on thin gold microshells. The SERS signals from this 2 μm diameter gold microshell sensitively depended on the conformation of the oligonucleotides with Raman reporters at their terminals. The folded hairpin structure of the strands led to strong SERS signals. It is well known that the SERS phenomenon originates because of the distance from the gold surface. We experimentally verified the use of this behavior for sensitive and selective detection of mercury(II) using DNA-modified gold microshells. In addition to the conformation-sensitive SERS signals, the DNA-modified gold microshells employed in this study had extraordinary advantages. These microshells can be individually manipulated using a micropipette and act as a SERS probe for the analysis of small volumes. It is worth mentioning that the behavior and technology described in this study are not limited to Hg^{2+} ion detection but can be extended to general spectroscopic analysis in environmental and biological samples. The principle involved is simple but promising.

In the second chapter, we discussed a novel microfluidic system involving a highly charge-selective polymer for sample preconcentration by electrokinetic trapping. Inspired by the exceptional preconcentration capability of the microfluidic system, we combined it with a bead-based competitive immunoassay to improve the sensitivity of conventional competitive immunoassays for the detection of small molecules. We employed fluorescent indicators, which were readily displaced by the unlabeled targets, and subsequently conducted the electrokinetic preconcentration of the released indicators in the microfluidic chip. We experimentally confirmed the working of the proposed scheme and understood its functioning. The underlying principle of the new method described in this report was concentration polarization, which was induced by electrochemical means. This is one of the promising and rapidly advancing fields of modern electrochemistry. It suggests a means to address the intrinsic problem of competitive immunoassays and holds tremendous potential to be widely applied to high-throughput immunosensing in clinical and biological samples.

In the third chapter, we report a new strategy for signal

amplification by redox cycling using a 3-dimensional interdigitated array (3D IDA) device consisting of two closely spaced parallel IDA electrodes facing each other. By employing a simple and practical process, we fabricated 3D IDA chips and obtained more sensitive electrochemical immunosensing of target antigens in human serum compared to any of the previous studies. Experiments as well as simulation consistently confirmed that the proposed scheme successfully functioned as predicted. We find that the method used in this work significantly improves conventionally used IDA; our studies is also a step forward in the field of electrochemical signal amplification, which can be used in realizing ideal electrochemical sensing devices. This is simple and clear, and can be widely applied to general electrochemical analysis in clinical and biological samples.

In the fourth chapter, we demonstrate the electrochemical grafting of amine-terminated dendrimers onto the ITO surface. The immobilization approach was applied to assemble Fc-Ds and Pt DENs. The electrochemical experiments clearly confirm that the two different types of dendrimer films were electrochemically grafted onto the ITO surface. Furthermore,

the resulting Fc-D and Pt DEN films were electrocatalytically active for the *p*-aminophenol redox reaction. Currently, we are exploring the possibility of applying this general strategy for the functionalization of ITO using a variety of catalytic materials, which might be useful for a broad range of electrocatalytic reactions.

Finally, we report a solid-state reference electrode operating in a buffered aqueous solution for the electrochemical system on a microfluidic chip. The solid-state reference electrode was constructed by combining the unique characteristics of np Pt and a poly-*m*-PD layer onto the ITO surface. The np Pt with the poly-*m*-PD film is easily produced and particularly compatible with microfabrication. The experimental results in this study demonstrate that the proposed system successfully works as a solid-state reference electrode, which can be integrated into microchips for microanalysis systems.

Appendix

A. Mask Layout

A.1. Overall mask layout

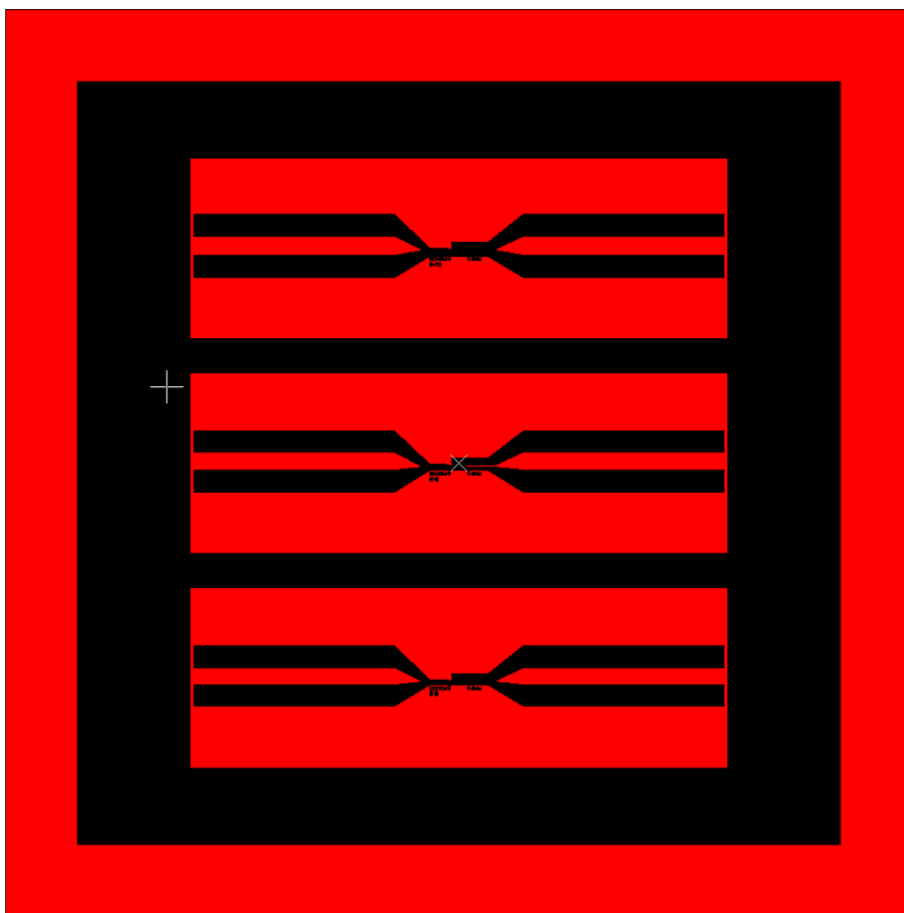


Fig. A-1 Overall mask layout.

A.2. Single sensor mask layout

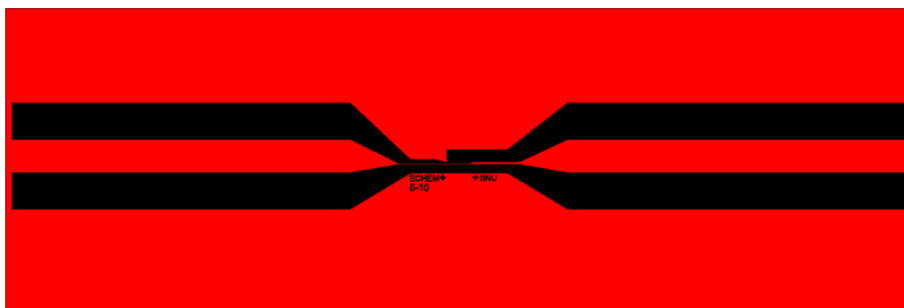


Fig. A-2 Single sensor mask layout.

A.3. Integrated three-electrode system structure

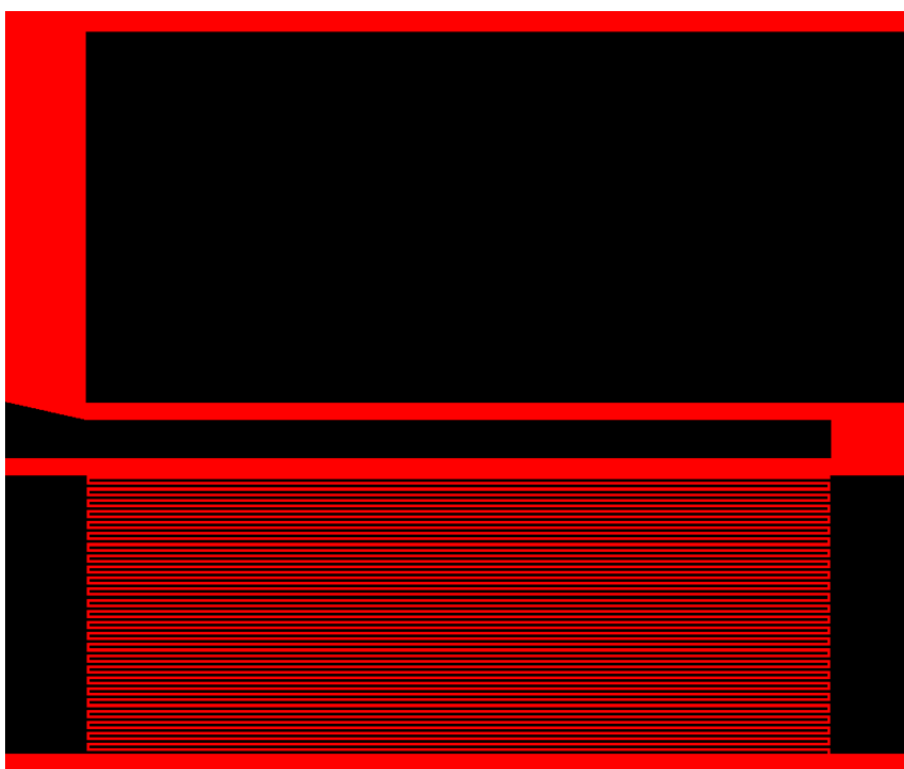


Fig. A-3 Mask layout of part of the integrated three-electrode system structure.

B. Cyclic Voltammetry Simulation at 3D IDA with COMSOL Mutiphysics

B.1. Introduction

Cyclic voltammetry is a common analytical technique for investigating electrochemical systems. In this method, the potential difference between a working electrode and a reference electrode is swept linearly in time from a start potential to a vertex potential, and back again (Fig. B-1). The resulting current at the working electrode is recorded and is plotted against the applied electrode potential in a voltammogram. Voltammetry is a valuable technique because information about both the electrochemical reactivity and the transport properties of a system can be extracted simultaneously. For quantitative interpretation of voltammetry, however, we must use numerical methods to solve the physical equations that describe voltammetry. Then, unknown physical quantities in the system can be inferred by ‘fitting’ to experimental data. This example demonstrates the use of a common approximation in which a three-dimensional interdigitated array (3D IDA) electrode is assumed to have uniform transport behavior across its surface, so only physics

occurring normal to the surface need to be considered. To decrease computing time, it is often recommended to simplify a three-dimensional problem into a two-dimensional problem when possible. Furthermore it is important to look at axes of symmetry. For the case of the 3D IDA electrode for example, it is possible to simplify the model into a single set of four collector and four generator electrodes.

B.2. Model definition

This model contains a single 2D domain of height $h = 30 \mu\text{m}$, which is the distance between top and bottom IDA electrodes. The band width of the IDA was $5 \mu\text{m}$ and the gap was $10 \mu\text{m}$. The approximation that the bulk solution is infinitely distant is suitable if the electrochemical cell is several orders of magnitude larger than the electrode.

B.2.1. Domain equations

We assume the presence of a large quantity of supporting electrolyte. This is inert salt that is added in electroanalytical experiments to increase the conductivity of the electrolyte without otherwise interfering with the reaction chemistry.

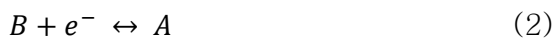
Under these conditions, the resistance of the solution is sufficiently low that the electric field is negligible, and we can assume that the electrolyte potential $\phi_e = 0$.

The Electroanalysis interface implements chemical species transport equations for the reactant and product species of the redox couple subject to this assumption. The domain equation is the diffusion equation (also known as Fick's 2nd law), which describes the chemical transport of the electroactive species A and B. At steady-state, this reduces to:

$$\nabla \cdot (D_i \nabla c_i) = 0 \quad (1)$$

B.2.2. Boundary equations

At the bulk boundary, we assume a uniform concentration equal to the bulk concentration for the reactant. The product has zero concentration here, as in bulk. At the boundary of the generator electrode of the 3D IDA ($x = 0$), the reactant species A oxidizes (loses one electron) to form the product B. By convention, electrochemical reactions are written in the reductive direction:



The stoichiometric coefficient is -1 for B, the "reactant" in

the reductive direction, and +1 for A, the “product” in the reductive direction. This formulation is consistent even in examples such as this model where at certain applied potentials, the reaction proceeds favorably to convert A to B. The number of electrons transferred, n , equals one.

The current density for this reaction is given by the electroanalytical Butler–Volmer equation for an oxidation:

$$i_{\text{loc}} = nFk_0 \left\{ c_A \exp\left(\frac{(n-\alpha_c)F\eta}{RT}\right) - c_B \exp\left(\frac{-\alpha_c F\eta}{RT}\right) \right\} \quad (3)$$

in which k_0 is the heterogeneous rate constant of the reaction, α_c is the cathodic transfer coefficient, and η is the overpotential at the working electrode. This overpotential is the difference between the applied potential and the equilibrium potential (formal reduction potential) of the redox couple of species A and B.

According to Faraday’s laws of electrolysis, the flux of the reactant and product species are proportional to the current density drawn:

$$-n \cdot N_i = \frac{v_i i_{\text{loc}}}{nF} \quad (4)$$

This is expressed in the Electrode Surface boundary condition.

The applied triangular waveform for the cyclic voltammetry study is specified in the Electrode Surface boundary condition

according to two vertex potentials—forming a potential window between -0.4 V and $+0.4$ V, either side of the equilibrium reduction potential—and a voltammetric scan rate, ν (SI unit: $\text{V} \cdot \text{s}^{-1}$), which is the rate at which the applied potential is changed.

B.3. Results and discussion

The shape of the cyclic voltammogram illustrates the relation between electrode kinetics and chemical species transport (diffusion). Fig. B-2 shows a typical cyclic voltammogram of an IDA electrode operated in feedback mode. As the potential of generator electrodes of the 3D IDA approached the redox potential, both collector and generator current of the 3D IDA increased by the same magnitude but with opposite sign. When the generator potential of the 3D IDA surpassed the redox potential, both electrode currents became stable.

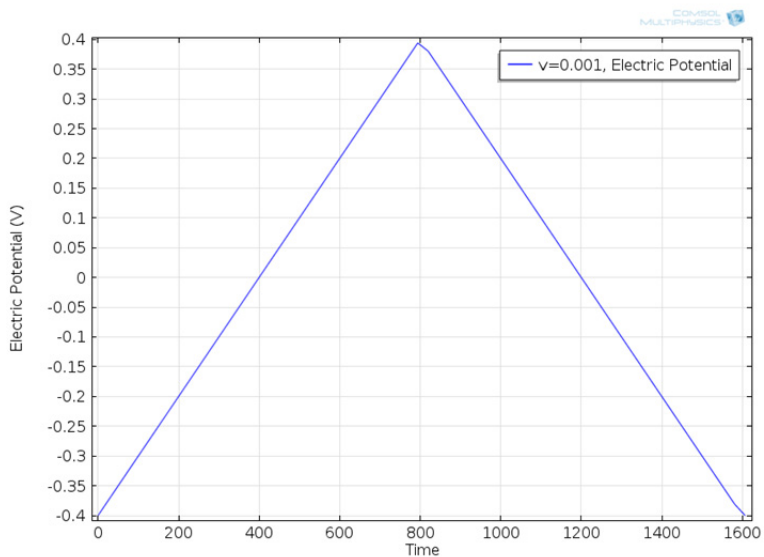


Fig. B-1 Potential of the working electrode during one voltammetric cycle. The potential is cycled between the vertex potentials -0.4 V and $+0.4\text{ V}$. Scan rate is $1\text{ mV} \cdot \text{s}^{-1}$.

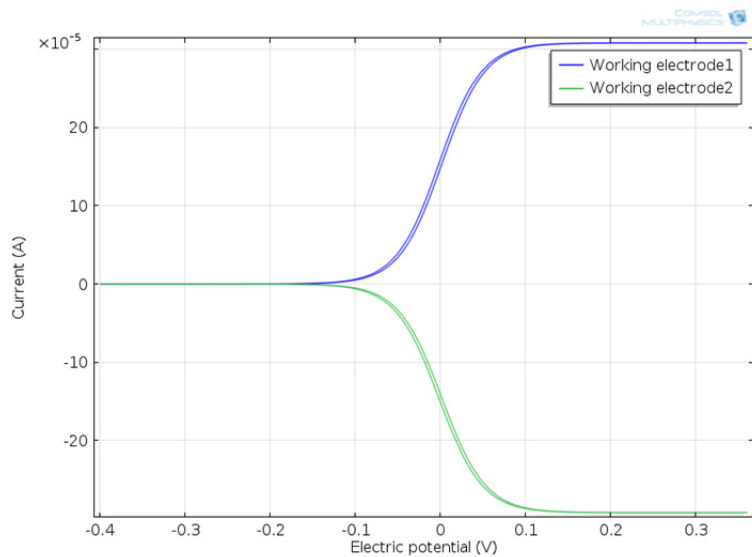


Fig. B-2 Cyclic voltammetry recorded at a 3D IDA electrode.

B.4. Modeling instructions

MODEL WIZARD

1. Open COMSOL Multiphysics.

2. In the **Model Wizard** window, click the **2D** button. Click **Next**.

3. In the **Add physics** tree, select **Electrochemistry**>

Electroanalysis (elan).



4. Click **Add Selected**.

5. This model will solve for the two concentrations of a redox couple. Change the default concentration variable names to cRed and cOx. Find the **Dependent variables** subsection. In the

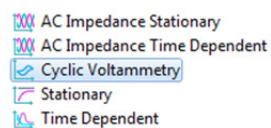
Concentrations table,

enter the following settings



6. Click **Next**.

7. Find the **Studies** subsection. In the tree, select **Preset Studies**>**Cyclic Voltammetry**.



GLOBAL DEFINITIONS

3. In the **Width** edit field, type 400.
4. In the **Height** edit field, type 30.
5. Locate the **Position** section. In the **x** edit field, type -175 .
6. Click the **Build Selected** button.

Rectangle 2

1. In the **Model Builder** window, right-click **Geometry 1** and choose Rectangle.
2. In the **Rectangle** settings window, locate the **Size** section.
3. In the **Width** edit field, type 5.
4. In the **Height** edit field, type 0.12.
5. Locate the **Position** section. In the **x** edit field, type 5.
6. Click the **Build Selected** button.

Rectangle 3

1. Right-click **Geometry 1** and choose Rectangle.
2. In the **Rectangle** settings window, locate the **Size** section.
3. In the **Width** edit field, type 5.
4. In the **Height** edit field, type 0.12.
5. Locate the **Position** section. In the **x** edit field, type 20.
6. Click the **Build Selected** button.

Rectangle 4

1. Right-click **Geometry 1** and choose Rectangle.
2. In the **Rectangle** settings window, locate the **Size** section.
3. In the **Width** edit field, type 5.
4. In the **Height** edit field, type 0.12.
5. Locate the **Position** section. In the **x** edit field, type 35.
6. Click the **Build Selected** button.

Rectangle 5

1. Right-click **Geometry 1** and choose Rectangle.
2. In the **Rectangle** settings window, locate the **Size** section.
3. In the **Width** edit field, type 5.
4. In the **Height** edit field, type 0.12.
5. Locate the **Position** section. In the **x** edit field, type 50.
6. Click the **Build Selected** button.

Rectangle 6

1. Right-click **Geometry 1** and choose Rectangle.
2. In the **Rectangle** settings window, locate the **Size** section.
3. In the **Width** edit field, type 5.

4. In the **Height** edit field, type 0.12.
5. Locate the **Position** section. In the **x** edit field, type 5.
6. Locate the **Position** section. In the **y** edit field, type 29.88.
7. Click the **Build Selected** button.

Rectangle 7

1. Right-click **Geometry 1** and choose Rectangle.
2. In the **Rectangle** settings window, locate the **Size** section.
3. In the **Width** edit field, type 5.
4. In the **Height** edit field, type 0.12.
5. Locate the **Position** section. In the **x** edit field, type 20.
6. Locate the **Position** section. In the **y** edit field, type 29.88.
7. Click the **Build Selected** button.

Rectangle 8

1. Right-click **Geometry 1** and choose Rectangle.
2. In the **Rectangle** settings window, locate the **Size** section.
3. In the **Width** edit field, type 5.
4. In the **Height** edit field, type 0.12.
5. Locate the **Position** section. In the **x** edit field, type 35.
6. Locate the **Position** section. In the **y** edit field, type 29.88.

7. Click the **Build Selected** button.

Rectangle 9

1. Right-click **Geometry 1** and choose Rectangle.
2. In the **Rectangle** settings window, locate the **Size** section.
3. In the **Width** edit field, type 5.
4. In the **Height** edit field, type 0.12.
5. Locate the **Position** section. In the **x** edit field, type 50.
6. Locate the **Position** section. In the **y** edit field, type 29.88.
7. Click the **Build Selected** button.
8. Click the **Zoom Extents** button on the Graphics toolbar. The finished geometry should look like Fig. B-3 in the Model Definition section.

DEFINITIONS

Make some selections on the geometry to use later when you set up the physics.

Variables 1

1. Right-click **Definitions** and choose **Variables**.
2. In the **Variables** settings window, locate the **Variables** section.

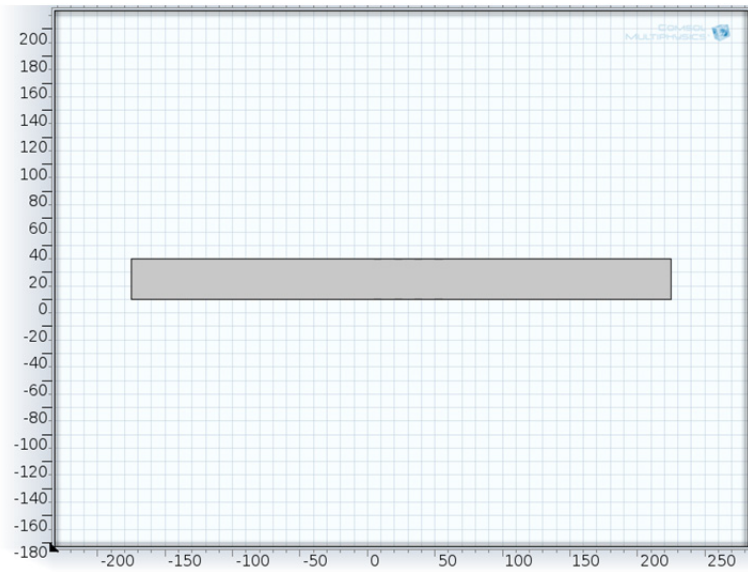


Fig. B-3 Model geometry.

3. In the table, enter the following settings.

Name	Expression	Unit	Description
i_WE1	intop1(elan.itot)	A/m	Working electrode1 current
i_WE2	intop2(elan.itot)	A/m	Working electrode2 current
i_WE3	elan.itotavg_els2	A/m ²	Current Density

Explicit 1

1. In the **Model Builder** window, under Model 1 right-click **Definitions** and choose **Selections>Explicit**.
2. Select Domains 2, 5, 6, and 9 only.
3. Right-click **Model 1>Definitions>Explicit 1** and choose **Rename**.
4. Go to the **Rename Explicit** dialog box and type *Working Electrode 1* in the **New name** edit field.
5. Click **OK**.

Explicit 2

1. Right-click **Definitions** and choose **Selections>Explicit**.
2. Select Domains 3, 4, 7, and 8 only.
3. Right-click **Model 1>Definitions>Explicit 2** and choose **Rename**.
4. Go to the **Rename Explicit** dialog box and type *Working Electrode 2* in the **New name** edit field.

5. Click **OK**.

Explicit 3

1. Right-click **Definitions** and choose **Selections>Explicit**.
2. In the **Explicit** settings window, locate the **Input Entities** section.
3. From the **Geometric entity level** list, choose **Boundary**.
4. Select Boundaries 4, 6, 10, 17, 18, 22, 24, 26, 30, 37, 38, and 42 only.
5. Right-click **Model 1>Definitions>Explicit 3** and choose **Rename**.
6. Go to the **Rename Explicit** dialog box and type *Working Electrode 1_Active Surface* in the **New name** edit field.
7. Click **OK**.

Explicit 4

1. Right-click **Definitions** and choose **Selections>Explicit**.
2. In the **Explicit** settings window, locate the **Input Entities** section.
3. From the **Geometric entity level** list, choose **Boundary**.
4. Select Boundaries 7, 8, 12, 14, 16, 20, 27, 28, 32, 34, 36,

and 40 only.

5. Right-click **Model 1>Definitions>Explicit 4** and choose **Rename**.

6. Go to the **Rename Explicit** dialog box and type *Working Electrode 2_Active Surface* in the **New name** edit field.

7. Click **OK**.

Integration 1

1. In the **Model Builder** window, right-click **Definitions** and choose **Model Couplings>Integration**.

2. In the **Integration** settings window, locate the **Source Selection** section.

3. From the **Geometric entity level** list, choose **Boundary**.

4. From the **Selection** list, choose **Working Electrode 1_Active Surface**.

Integration 2

1. In the **Model Builder** window, right-click **Definitions** and choose **Model Couplings>Integration**.

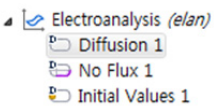
2. In the **Integration** settings window, locate the **Source Selection** section.

3. From the **Geometric entity level** list, choose **Boundary**.
4. From the **Selection** list, choose **Working Electrode 2_Active Surface**.

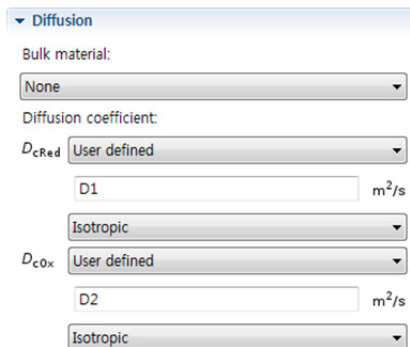
ELECTROANALYSIS

Diffusion 1

Start defining the physics by setting the diffusion coefficients for the two species of the redox couple.

1. In the **Model Builder** window, under **Electroanalysis (elan)** **Model 1** > **Electroanalysis** click **Diffusion 1**.
 

2. In the **Diffusion** settings window, locate the **Diffusion** section



3. In the D_{cRed} edit field, type $D1$.
4. In the D_{cOx} edit field, type $D2$.

Concentration 1

Now, set the boundary to the right to bulk concentration values.

1. In the **Model Builder** window, right-click **Electroanalysis**

and choose **Concentration**.

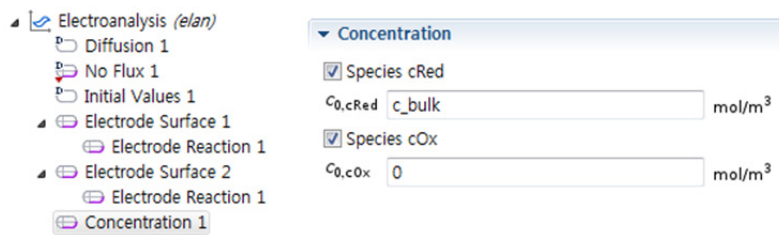
2. Select Boundary 1 and 44 only.

3. In the **Concentration** settings window, locate the **Concentration** section.

4. Select the **Species cRed** check box.

5. In the $c_{0,cRed}$ edit field, type c_{bulk} .

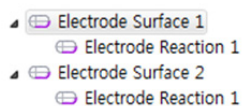
6. Select the **Species cOx** check box.



Electrode Surface 1

Set up the electrode surface and the cyclic voltammetry settings on the left boundary.

1. Right-click **Electroanalysis** and choose **Electrode Surface**.



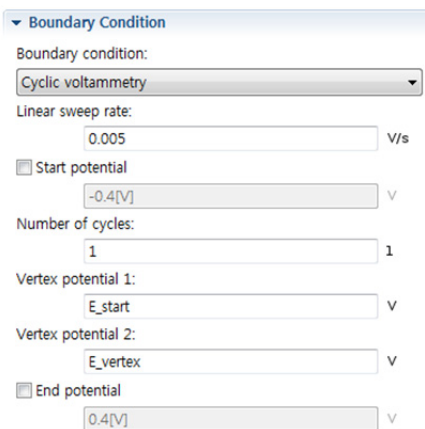
2. From the **Boundary selection** list, choose **Working Electrode 1_Active Surface**.

3. In the **Electrode Surface** settings window, locate the **Boundary Condition** section.

4. From the **Boundary condition** list, choose **Cyclic**

voltammetry.

5. In the **Linear sweep rate** edit field, type *0.005*. The voltage will be cycled between the vertex potentials. When a distinct **Start potential** is not



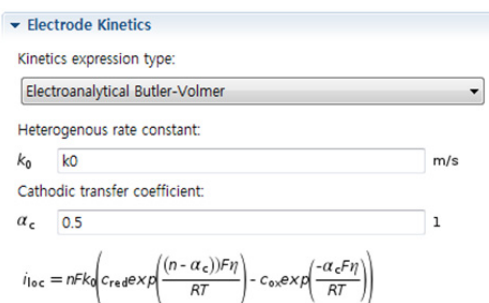
specified, the sweep will start at **Vertex potential 1**.

6. In the **Vertex potential 1** edit field, type *E_start*, and in the **Vertex potential 2** edit field, type *E_vertex*.

Electrode Reaction 1

Specify the electrode reaction using **Electroanalytical Butler–Volmer** kinetics. The current is concentration dependent, as defined by the stoichiometric coefficients.

1. In the **Model Builder** window, expand the **Electrode Surface 1** node, then click **Electrode Reaction 1**.



2. In the **Electrode Reaction** settings window, locate the

Electrode Kinetics section.

3. In the k_0 edit field, type k_0 .
4. Locate the **Stoichiometric Coefficients** section. In the ν_{cRed} edit field, type 1 .
5. In the ν_{cOx} edit field, type -1 .

▼ Stoichiometric Coefficients

Number of participating electrons:

n_m 1

Stoichiometric coefficient:

ν_{cRed} 1

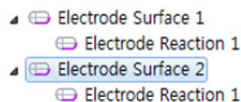
ν_{cOx} 1

$$R_{i,m} = \frac{\nu_{i,m} i_{loc,m}}{n_m F}$$

Electrode Surface 2

Add an **Electrode Surface** condition. Set up the electrode kinetics in the **Electrode Reaction** subnode.

1. In the **Model Builder** window, right-click **Electroanalysis** and choose



Electrode Surface.

2. From the **Boundary selection list**, choose **Working Electrode 2_Active Surface**.

▼ Boundary Condition

Boundary condition:

Electrode potential vs reference:
 $E_{vs,ref}$ v

Electric reference potential:
 $\phi_{s,ref}$

v

3. In the **Electrode Surface** settings window, locate the **Boundary Condition** section.

4. From the **Boundary condition** list, choose **Electrode potential**.

5. In the $E_{vs\ ref}$ edit field, type E_{start} .

Electrode Reaction 2

1. In the **Model Builder** window, expand the **Electrode Surface 2** node, then click **Electrode Reaction 1**.

Electrode Kinetics

Kinetics expression type:

Heterogenous rate constant:
 k_0 m/s

Cathodic transfer coefficient:
 α_c 1

$$i_{loc} = nFk_0 \left(C_{red} \exp\left(\frac{(n - \alpha_c)F\eta}{RT}\right) - C_{ox} \exp\left(\frac{-\alpha_c F\eta}{RT}\right) \right)$$

2. In the **Electrode Reaction** settings window, locate the **Equilibrium Potential** section.

Stoichiometric Coefficients

Number of participating electrons:
 n_m 1

Stoichiometric coefficient:
 ν_{cRed} 1
 ν_{cOx} 1

$$R_{i,m} = \frac{\nu_{i,m} i_{loc,m}}{n_m F}$$

3. In the $E_{eq, ref}$ edit field, type Ef .

4. Locate the **Electrode Kinetics** section. In the k_0 edit field, type $k0$.

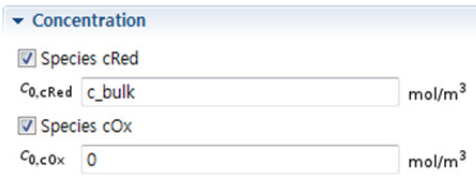
5. Locate the **Stoichiometric Coefficients** section. In the ν_{cRed} edit field, type 1 .

6. In the ν_{cOx} edit field, type -1 .

Initial Values 1

Now specify the initial concentration values. This will set concentration values when the simulation starts at $t = 0$.

1. In the **Model Builder** window, under **Model 1** > **Electroanalysis** click



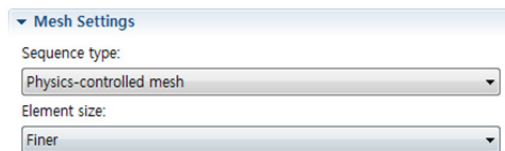
Initial Values 1.

2. In the **Initial Values** settings window, locate the **Initial Values** section.
3. In the cRed edit field, type *c_bulk*.

MESH 1

1. In the **Model Builder** window, under **Model 1** click **Mesh 1**.
2. In the **Mesh** settings window, locate the **Mesh Settings** section.

3. From the **Element size** list, choose **Finer**.



STUDY 1

The problem is now ready for solving.

1. Right-click **Study 1** and choose **Compute**.

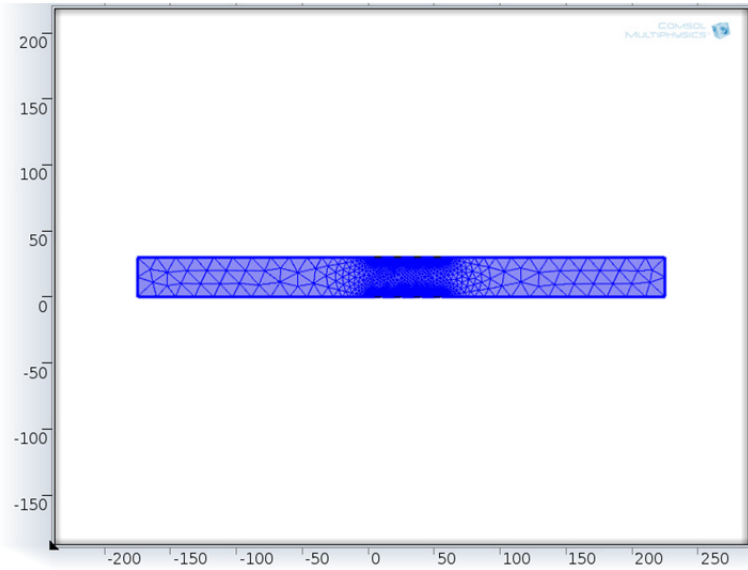


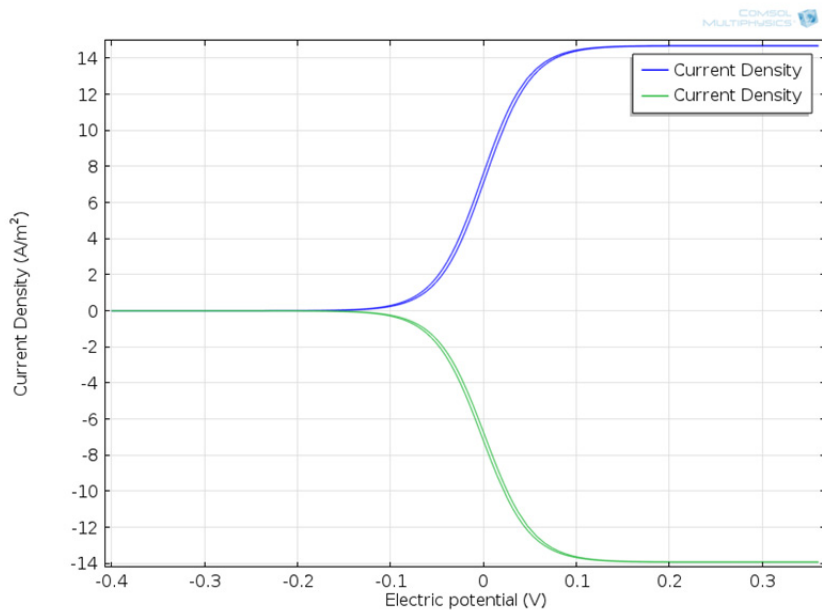
Fig. B-4 Customized mesh used for the 3D IDA analysis.

RESULTS

Cyclic Voltammograms (elan)

A number of plots are created by default. The first default plot shows the voltammograms created by the Cyclic voltammetry feature in the Electrode Surface node.

1. In the **Model Builder** window, under **Results** click **Cyclic Voltammograms (elan)**.
2. Modify the default legend position. In the **1D Plot Group** settings window, click to expand the **Legend** section and from the **Position** list, choose **Upper left**.
3. Click the **Plot** button. The plot should like this:



국문초록

현대의 분석 연구는 생분자 검출을 위해 민감하고 신뢰할 수 있으며 비싸지 않은 고 처리량 분석 방법 개발이 임상 진단, 식품 안전 및 환경 감시에 있어서 큰 잠재력을 보여주고 있다. 생분석에 있어서 가장 중요한 문제 중 하나는 매우 민감한 신호를 만들어 내는 것인데, 이는 분석하고자 하는 물질이 샘플과 시약의 아주 적은 처리 및 소모와 밀접한 관계가 있음을 알 수 있다. 본 학위 논문은 화학 및 생 분석 검출의 성능을 향상시키기 위한 분석 방법론의 개발 및 응용에 관한 연구이다.

첫째, 수은 이온 검출을 위해 금 마이크로셀을 기반한 표면 증강 라만 산란 센서를 개발하였다. 이 센서는 라만 활성 물질인 테트라 메틸로다민이 표지된 DNA 머리핀 구조를 기반하며 수은 이온에 대해 티민-티민 불일치에서의 선택적 결합을 전략적으로 제공한다. 이 센서는 좋은 민감도와 금 마이크로셀 표면 위에 제한된 라만 분자의 SERS 신호 변화 관찰을 통해 50 nM 의 검출한계를 보였다. 다양한 다른 경쟁 금속 이온들로부터 수은 이온의 명확한 구별을 통해 센서의 선택성을 입증하였다. 또한 DNA가 고정된 단일 금 마이크로셀은 마이크로피펫을 이용하여 개별적으로 조작을 할 수 있었다. 이러한 DNA가 고정된 단일 금 마이크로셀을 통해 소체적 샘플에서 수은 이온의 검출을 성공적으로 수행할 수 있음을 입증하였다.

둘째, 마이크로 유동칩에서의 매우 높은 전하 선택성을 지닌 고분자 [poly-2-acrylamido-2-methyl-1-propanesulfonic acid (pAMP SA)] 플러그 가까이에서 일어나는 동전기적인 농축을 통해 경쟁적 면역 분석법의 민감도를 증가시키기 위한 새로운 방법을 고안하였다. 이온 분포를 정교하게 조절하는 효과적인 전하 선택성을 지닌 추출기로 기여하는 고분자 전해질 젤은 마이크로 유동 채널 안에서 광중합을 통해 제작되었다. 본 시스템은 샘플 안에 분산된 자성 마이크로비드 위의 형광 지시체가 꼬리표가 붙지 않은 타겟 분자에 의해 자발적으로 대체된 후 마이크로 유동 칩 상의 단일 특정한 곳에 동전기적으로 농축한다. 국부적으로 농축된 형광 지시체는 레이저 유도 형광을 이용해 검출하였다. 개념 입증 연구로서 꼬리표가 붙지 않은 1 nM 바이오틴의 경쟁적 치환 분석 시험을 통해 3분 안에 2000배에 달하는 농축을 관찰했다. 꼬리표가 붙지 않은 작은 타겟 분자의 민감한 검출뿐만 아니라 제안한 면역 분석 시스템은 바이오틴 유사 물질인 바이오사이틴, 2-이미노바이오틴, 데스티오바이오틴에 대해서도 좋은 선택성을 보였다.

셋째, 칩 기반인 면역센서의 민감도 증가를 위한 신호 증폭을 위해 3차원 집적화 전극에 기반한 전기화학적 산화환원 순환을 제안하였다. 3차원 집적화 전극은 가까이 간격을 둔 2개의 ITO 전극으로 이루어져 있으며, 천장뿐만 아니라 바닥에 위치해있고

마이크로 유동 채널을 따라 서로 마주보고 있는 형태이다. 전기화학적 실험과 유한 요소 시뮬레이션을 통해 평행한 전극, 열린 2차원 집적화 전극, 닫힌 2차원 집적화 전극 및 3차원 집적화 전극의 기하학적 배치에 대한 신호 세기의 영향을 주는지 연구하였다. 4개의 다른 시스템 중에 3차원 집적화 전극은 제한된 마이크로 채널 안에서 전기화학적 활성을 띤 물질의 효과적인 산화환원 순환을 통해 페러데이 전류가 100배가 증가되었다. 샌드위치 효소면역측정법을 기반한 시간대전하적인 면역 검출 플랫폼 구축을 3차원 집적화 전극의 증가된 민감도에 이용하였다. 3차원 집적화 전극에서 mouse IgG 의 검출한계는 닫힌 2차원 집적화 전극보다 더 낮은 검출한계를 보였다. 또한 3차원 집적화 전극을 기반한 면역센서 시스템은 인혈청 안에서 100 fg/mL cardiac troponin I 의 민감한 검출을 통해 임상적 분석에 성공적으로 이용할 수 있었다.

넷째, 아민 말단화된 PAMAM 덴드리머를 ITO 표면 위에 덴드리머의 아민 말단 그룹의 전기산화적 결합을 통해 고정할 수 있었다. 전기화학적 측정법으로 ITO 표면 위에 아민 말단화된 덴드리머의 전기화학적 결합을 확인하였다. 이러한 고정화 방법으로 ITO 표면 위에 Fc-D 와 Pt DENs 을 만들기 위해 적용하였고, 덴드리머가 접합된 막은 아미노페놀의 산화환원 반응에 대한 전기 촉매 작용 활성을 보였다.

마지막으로 마이크로 칩 안에서 삼 전극 시스템 제작이 가능한 새로운 방법을 개발하였다. 고체 상태인 기준전극, ITO 작업전극 및 전기 도금된 Pt 보조전극이 집적화된 칩의 제작은 일반적인 사진석판술 방법을 사용하였다. 전압과 시간에 관한 전기도금 조건들을 기준전극과 보조전극으로 사용되는 전기도금된 막의 안정성과 균일성에 대해 연구하였다. 고체 상태인 기준전극은 나노다공성 백금 표면 위에 전기고분자화된 poly-*m*-PD 막을 이용하여 제작하였다. 삼 전극 시스템의 전기화학적 성능은 순환전압전류법을 통해 평가하였다. 제안한 시스템은 고체 상태인 기준전극으로서 성공적으로 작동을 하며, 미량분석 시스템을 위해 마이크로 칩 안으로 집적화 시킬 수 있음을 실험을 통해 증명하였다.

주요어: 표면 증강 라만 산란, 동전기적 농축, 3차원 집적화 전극, 산화환원 순환, 전기그래프트가공, 집적화된 전기화학적 검출 플랫폼

학 번: 2009-30852